

The Pennsylvania State University

The Graduate School

College of Engineering

## **COMPLETE VECTOR NETWORK ANALYZER**

## **APPROACH TO ICE PENETRATING RADAR SYSTEM**

A Thesis in

Electrical Engineering

By

Brian Alexander Herrold

© 2013 Brian Alexander Herrold

Submitted in Partial Fulfillment  
of the Requirements  
for the Degree of

Master of Science

August 2013

The thesis of Brian Alexander Herrold has been reviewed and approved\* by the following

Sven G. Bilén

Associate Professor of Engineering Design, Electrical Engineering, and Aerospace Engineering  
Thesis Advisor

Julio V. Urbina

Associate Professor of Electrical Engineering

Sridhar Anandakrishnan

Professor of Geosciences

Kultegin Aydin

Professor of Electrical Engineering

Department Head of Electrical Engineering

\* Signatures are on file in the Graduate School

## **Abstract**

This thesis explores the design of a complete system for Ice-Penetrating Radar (IPR) measurements of polar-region ice thickness. The goal of the radar system is provide high resolution measurements of the change in ice thickness between successive measurements at a fixed location on the ice over time. The design requirement for resolution in thickness change is better than  $\pm 1\text{mm}$ . The system designed can make absolute ice thickness to a much less accurate degree than the relative measurements of thickness change.

This approach is based on adapting a previously published design for a low-cost Vector Network Analyzer (VNA) to a rugged form factor and optimizing the performance parameters of the instrument to maximize its usefulness for ice-penetrating radar measurements. The radar relies on precise measurement of the magnitude and phase response of the propagation path from transmitting antenna to receiving antenna, through the ice and off the ice bottom, to make the thickness measurements. The phase change of the response of the ice between successive measurements allows the user to determine small thicknesses changes with very high accuracy. The inverse Fourier transform of the magnitude and phase frequency-response of the path provides the time domain approximation of the path response to a very short radar pulse.

# TABLE OF CONTENTS

List of Tables.....	ix
List of Figures.....	x
Chapter 1: Introduction.....	1
1.1 Motivations for Ice-Penetrating Radar System Development.....	1
1.2 Glaciological Terminology.....	2
1.3 Mass Balance and Cyclical Changes.....	3
1.4 Ice-Penetrating Radar Concept of Operations.....	5
1.5 Contribution of this Thesis.....	7
1.6 Overview of Thesis.....	7
Chapter 2: Background.....	10
2.1 Historical Context.....	11
2.2 General Radar Remote Sensing Principles.....	13
2.2.1 Radars for Snow Thickness.....	14
2.3 Electromagnetic Properties of Ice and Snow.....	15
2.3.1 Electric Permittivity.....	17
2.3.2 Magnetic Permeability.....	19
2.3.3 Conductivity.....	19
2.3.4 Propagation Velocity.....	21
2.3.5 Refractive Index and Reflection Coefficient.....	22

2.3.6 Path Loss through Ice and Snow Media.....	25
2.4 Types of Radars for Ice-Thickness Sounding.....	29
2.4.1 Monostatic, Psuedo-Monostatic, and Bistatic Radars.....	30
2.4.2 Pulsed and Chirp Radars.....	31
2.4.3 Frequency-Modulated Continuous-Wave Radar (FMCW).....	32
2.4.4 High Phase-Accuracy Network Analyzer Approach.....	33
2.5 Considerations for an IPR System.....	39
2.5.1 Receiver Power Sensitivity and loss Mechanisms.....	39
2.5.2 Sampling Rate.....	39
2.5.3 Implications of Phase Stability and Jitter.....	40
2.5.4 Phase Measurement Reference Selection.....	41
2.6 System Level Block Diagram of Proposed Approach.....	44
2.7 System Functional Requirements.....	45
Chapter 3: Vector Network Analyzer Background.....	48
3.1 Scattering Parameters and the Device Under Test (DUT).....	49
3.2 VNA Measurements, Modes, and Figures of Merit.....	53
3.3 VNA System Block Diagram.....	56
3.4 Input Protection Circuitry.....	57
3.5 Test Set and Directional Circuitry.....	59
3.5.1 VSWR Bridge.....	64
3.5.2 RF Directional Coupler.....	66

3.6 Step Attenuators and Signal Level Control .....	66
3.7 Core Reference Oscillator.....	68
3.8 Frequency Sweep Generation.....	70
3.9 Phase-Locked-Loops (PLLs).....	72
3.10 Receiver Sets.....	74
3.10.1 Quadrature Phase Detection.....	74
3.11 A/D Sampling.....	76
3.12 Signal Chain Accuracy and Calibration.....	78
3.12.1 Types of Calibrations and Error Correction.....	79
3.12.2 Systematic Error Modeling.....	80
3.12.3 Base Reference Oscillator.....	87
Chapter 4: Antenna Design.....	96
4.1 Antenna RF Performance Requirements.....	96
4.2 Design Equation Background.....	98
4.3 Full Wave Simulation of Antenna.....	101
4.4 Idealized Analysis of Transmit/Receive Coupling.....	123
4.5 Loading of Ice in the Near Field.....	149
4.6 Antenna Phase Center.....	151
Chapter 5: VNA Design implementation.....	154
5.1 VNA Architecture Overview.....	154
5.1.1 Published Low-Cost VNA Architectures.....	154

5.2 Base Reference Oscillator.....	158
5.3 Direct Digital Synthesis.....	160
5.3.1 Spur and Harmonic Products.....	161
5.3.2 DDS Phase-Coherence and Synchronization.....	164
5.4 VSWR Bridge.....	165
5.5 Tuned Receiver.....	167
5.6 Digitization.....	169
5.7 Miscellaneous Component Selection .....	169
5.7.1 RF Signal Capacitors.....	170
5.7.2 Inductors.....	170
5.7.3 Resistor Selection.....	171
5.7.4 PCB Substrates and Plating.....	171
5.8 Digital Processing and Control.....	171
5.8.1 DSP Capable Microcontroller.....	172
5.8.2 Embedded Linux Platforms for Interfaces.....	174
5.9 Power.....	174
5.9.1 Power Requirements of VNA.....	175
5.9.2 Power Supply Architecture.....	175
5.9.3 Battery Pack for Long Term Monitoring.....	175
5.9.4 Switching Supply Pre-Regulator.....	176
5.9.5 Point-of-Load Linear Regulators.....	177

5.9.6 Power Supply Layout Guidelines.....	177
5.10 Mechanical and Environmental.....	178
5.10.1 Thermal Environment.....	178
5.10.2 Moisture, Humidity & Condensation.....	180
5.10.3 Requirements and Testing for Corrosion Resistance .....	180
5.10.4 Requirements and Testing for Mechanical Shock and Vibration.....	180
5.11 Electronics Enclosures.....	181
5.12 Mounting and Mechanical Structures.....	182
5.13 RF Interconnects.....	183
5.14 Data Interconnects.....	185
Chapter 6: Conclusions.....	187
References.....	189
Appendix: Development Software Information.....	194

## LIST OF TABLES

Table 1: Size and Volume of Major World Ice Sheets.....	2
Table 2: Electrical Properties of Earth and Ice Sheet Materials (Data from [Beres, 1991]).....	23
Table 3: Phase Resolution by ADC Bit Depth and Reference Phase.....	43
Table 4: Ice Sheet Thickness Resolution by ADC Bit Depth and Reference Phase.....	43
Table 5: Abbreviated System Requirements.....	45
Table 6: CLP5130-2 Log-Periodic antenna data.....	97
Table 7: Connor–Winfield D53G reference oscillator technical data.....	159
Table 8: AVX/Kyocera KT7050A20000KAW33TAD oscillator technical data.....	160

## LIST OF FIGURES

Figure 1: Attenuation of ice for various conductivities from $10^{-6}$ to $10^{-3}$ .....	27
Figure 2: Attenuation of ice for various conductivities from $10^{-5}$ to $10^{-4}$ .....	29
Figure 3: Resolvable depth calculating sheet thickness based directly on frequency spread.....	38
Figure 4: Ice-Penetrating radar block diagram.....	44
Figure 5: One-Port Network as viewed from VNA.....	50
Figure 6: Two Port Network as seen from the VNA.....	51
Figure 7: Simplified VNA single channel block diagram.....	57
Figure 8: Test Set represented as a three-port network to the VNA system.....	60
Figure 9: Standard VSWR bridge block diagram.....	64
Figure 10: Clock distribution architecture in typical VNA.....	71
Figure 11: Simplified PLL Topology.....	72
Figure 12: Model of two-port VNA with four port bridge error term calculation.....	81
Figure 13: VNA model with error network and ideal bridge.....	85
Figure 14: Single antenna geometry with radiation pattern cuts, snow media suppressed.....	101
Figure 15: Antenna model setup with log-periodic position 10 cm above modeled snow.....	102
Figure 16: Antenna gain with loading of snow media, 50 MHz, E-Plane.....	103
Figure 17: Antenna gain with loading of snow media, 50 MHz, H-Plane.....	104
Figure 18: Antenna gain with loading of snow media, 100 MHz, E-Plane.....	105
Figure 19: Antenna gain with loading of snow media, 100 MHz, H-Plane.....	106

Figure 20: Antenna gain with loading of snow media, 150 MHz, E-Plane.....	107
Figure 21: Antenna gain with loading of snow media, 150 MHz, H-Plane.....	108
Figure 22: Antenna gain with loading of snow media, 200 MHz, E-Plane.....	109
Figure 23: Antenna gain with loading of snow media, 200 MHz, H-Plane.....	110
Figure 24: Antenna gain with loading of snow media, 250 MHz, E-Plane.....	111
Figure 25: Antenna gain with loading of snow media, 250 MHz, H-Plane.....	112
Figure 26: Antenna gain with loading of snow media, 300 MHz, E-Plane.....	113
Figure 27: Antenna gain with loading of snow media, 300 MHz, H-Plane.....	114
Figure 28: Antenna gain with loading of snow media, 350 MHz, E-Plane.....	115
Figure 29: Antenna gain with loading of snow media, 350 MHz, H-Plane.....	116
Figure 30: Antenna gain with loading of snow media, 400 MHz, E-Plane.....	117
Figure 31: Antenna gain with loading of snow media, 400 MHz, H-Plane.....	118
Figure 32: Antenna gain with loading of snow media, 450 MHz, E-Plane.....	119
Figure 33: Antenna gain with loading of snow media, 450 MHz, H-Plane.....	120
Figure 34: Antenna gain with loading of snow media, 500 MHz, E-Plane.....	121
Figure 35: Antenna gain with loading of snow media, 500 MHz, H-Plane.....	122
Figure 36: Previous Ice Radar system, reproduced from [Mendoza, 2012].....	124
Figure 37: Previous antenna coupling model, antennas parallel and broadside.....	124
Figure 38: Antenna coupling model recommended collinear configuration.....	125
Figure 39: Model setup for configuration with antennas oriented orthogonally polarized.....	126

Figure 40: Received power levels on coupled antennas of various configurations.....	127
Figure 41: Coupling between Tx and Rx antennas for various orientations of the antenna.....	128
Figure 42: Antenna pattern perturbation (E-Plane) from Tx/Rx coupling at 50 MHz.....	129
Figure 43: Antenna pattern perturbation (H-Plane) from Tx/Rx coupling at 50 MHz.....	130
Figure 44: Antenna pattern perturbation (E-Plane) from Tx/Rx coupling at 100 MHz.....	131
Figure 45: Antenna pattern perturbation (H-Plane) from Tx/Rx coupling at 100 MHz.....	132
Figure 46: Antenna pattern perturbation (E-Plane) from Tx/Rx coupling at 150 MHz.....	133
Figure 47: Antenna pattern perturbation (H-Plane) from Tx/Rx coupling at 150 MHz.....	134
Figure 48: Antenna pattern perturbation (E-Plane) from Tx/Rx coupling at 200 MHz.....	135
Figure 49: Antenna pattern perturbation (H-Plane) from Tx/Rx coupling at 200 MHz.....	136
Figure 50: Antenna pattern perturbation (E-Plane) from Tx/Rx coupling at 250 MHz.....	137
Figure 51: Antenna pattern perturbation (H-Plane) from Tx/Rx coupling at 250 MHz.....	138
Figure 52: Antenna pattern perturbation (E-Plane) from Tx/Rx coupling at 300 MHz.....	139
Figure 53: Antenna pattern perturbation (H-Plane) from Tx/Rx coupling at 300 MHz.....	140
Figure 54: Antenna pattern perturbation (E-Plane) from Tx/Rx coupling at 350 MHz.....	141
Figure 55: Antenna pattern perturbation (H-Plane) from Tx/Rx coupling at 350 MHz.....	142
Figure 56: Antenna pattern perturbation (E-Plane) from Tx/Rx coupling at 400 MHz.....	143
Figure 57: Antenna pattern perturbation (H-Plane) from Tx/Rx coupling at 400 MHz.....	144
Figure 58: Antenna pattern perturbation (E-Plane) from Tx/Rx coupling at 450 MHz.....	145
Figure 59: Antenna pattern perturbation (H-Plane) from Tx/Rx coupling at 450 MHz.....	146

Figure 60: Antenna pattern perturbation (E-Plane) from Tx/Rx coupling at 500 MHz.....	147
Figure 61: Antenna pattern perturbation (H-Plane) from Tx/Rx coupling at 500 MHz.....	148
Figure 62: Antenna orientation for modeling of media effect frequency series.....	150
Figure 63: Log-Periodic antenna phase center distribution.....	152
Figure 64: VNA block diagram proposed by Baier .....	155
Figure 65: Block diagram for VNA design with independent A/D and local DSP.....	156
Figure 66: Clock source signal chain.....	158
Figure 67: DDS alias, harmonic, and spur products and their ouput power.....	162
Figure 68: DDS LO and RF DAC image spacings.....	163
Figure 69: DDS RF and LO spectral product placement to attenuate mix products.....	164
Figure 70: Standard VSWR bridge with for differential input.....	165
Figure 71: Improved VSWR bridge with DC blocking and bleed resistor.....	166
Figure 72: VSWR bridge with broadband transformer for ground isolation.....	167

## Acknowledgements

The thesis preparation guide suggests that I make use of the acknowledgements section to express my professional indebtedness to those who have helped me in my academic career. As I contemplate how best to do that, it seems almost laughable that a few sentences of Front Matter could ever begin to adequately express my gratitude to those at this University who I have come to know and call my friends and colleagues over the years.

I've been here for quite some time now — first as a traditional undergraduate student and subsequently for many years after as a working professional engineer — struggling to find spare moments to complete this Masters in long, late hours after work. It's been a trying ordeal for me and even more so for those of you who I have dragged through it with me. And I wouldn't change any of it had I the chance to do it all again. I've had the time of my life.

In particular, I would like to thank those from whom I have learned so much, both in the classroom and the lab. I owe so much of what I know of circuit theory and analog design to the amazing Mark Wharton and Dr. Jack Mitchell; they are the best anywhere. Nor can I ever adequately thank Dr. Jim Breakall for all I have learned about antenna design and electromagnetics.

I am forever indebted to my incredibly patient committee members Dr. Julio Urbina and Dr. Sridhar Anandakrishnan. Since I began this work in earnest six months ago, both have been understanding of my ridiculous work and travel schedules, always willing to find times to meet, and to teach me more than I ever thought I would know about ice. I certainly do not deserve the forbearance that they have shown to my late submissions of thesis drafts, my cluttered defense slides, or the amount of effort they have put into helping me understand the science behind the technical challenges of this thesis. Your guidance has shaped this work and has made me a better engineer. Thank you both.

It should go without saying that my biggest debt of gratitude is owed to my advisor Sven Bilén. I have known Sven for nearly ten year now, from those first undergraduate days to the space systems class and on to the completion of this thesis, he has been there at every step to answer my questions. Sometimes with answers, and sometimes — as the best teachers and mentors always do — with other questions that lead me off to discover something new for myself. This is the mark of academic excellence. Not to dispense formulas, but to guide discovery.

There is no way I can truly put into a few sentences all that I have learned from Sven. So I will not try to do it justice. Even just in the process of editing this thesis, I have learned so much from him — including that I had an incredibly unsophisticated understanding of the lengths of various dashes. (That one was an em!)

So to Sven, I offer my thanks. They are, as mere words all too often are, insufficient for what is owed. I thank you for all I have learned about space systems and systems engineering. I thank for all I have learned about SDR. I thank you for your patience and indulgence these many years, encouraging me to finish this thesis. Were it anyone else, I never could have made it. And most importantly, I thank for the example you have set. It is one of leadership, sharing your knowledge with those willing to learn, academic excellence, and integrity.

“My favorite programming language is solder.”

— Robert A. Pease —

# **CHAPTER 1: INTRODUCTION**

In this introductory chapter, the motivation for this thesis and the theory of operation of Ice-Penetrating Radar (IPR) systems is described. This chapter serves as background information for the radar system design developed and characterized as the topic of this thesis.

It should be explicitly noted at the outset that the topic of this thesis is not to study climate change, global warming, or to make any claims about the mechanisms responsible for ice melting in polar regions. This thesis research is focused on developing methods and technology that will enable the scientific study of the rates and patterns of ice melt, not to reach conclusions about the causes of the trends or causes of those phenomena.

## **1.1 Motivations for Ice-Penetrating Radar System Development**

There is growing concern about the melting of arctic and antarctic ice bodies due to an observed trend of increasing global air and sea temperatures [Legarsky, 1997]. The impact of ice melt on the large ice sheets and ice shelves of Antarctica and, to a lesser extent, Greenland is significant [Gogineni, 1998] [Kuchikulla, 2004]. The continental ice sheets of Antarctica and Greenland represent 27.6 million cubic kilometers of fresh water comprising 98–99% of the fresh water on the surface of the Earth [Bentley, 2007] [IPCC, 2007]. The Antarctic ice sheet is of particular interest as it contains approximately nine times more ice than the Greenland ice sheet, the next largest [Bentley, 2007]. To understand the sheer scale of the impact of excessive ice-melt, consider the estimates of sea level rise were these large continental ice sheets to melt. Ice sheet area is presented in Table 1. Data for Table 1 is taken from the 2007 Intergovernmental Panel on Climate Change (IPCC) report [IPCC, 2007]. Should the total ice sheet area melt — something that would admittedly take in excess of 1000 years — sea levels would rise

almost 64 meters [IPCC, 2007], rendering vast stretches of the Earth no longer inhabitable. Even small rises, however, have significant impacts on life in large densely-populated coastal areas [Jenkins, 2003].

In addition to the major ice sheets, the ice shelves that float over the sea contribute significantly to the overall melting rate of polar ice. The fresh melt-water from these ice shelves plays a critical role in ocean current circulation — deep ocean convection — which impacts the overall melt rate [Jenkins, 2003] and oceanic currents. For this reason, it is particularly important to understand the specific rates at which these ice shelves are melting rather than simply extracting the ice shelf melt rate as a calculated value from a mass balance equation for the ice sheet as a whole.

*Table 1: Size and Volume of Major World Ice Sheets*

	<b>Area Covered</b> [Millions of Square Kilometers]	<b>Ice Volume</b> [Millions of Square Kilometers]	<b>Potential Sea Level Rise</b> [Meters]
<b>Ice Sheet (Total)</b>	<b>14.0</b>	<b>27.6</b>	<b>63.9</b>
Antarctica	12.3	24.7	56.6
Greenland	1.7	2.9	7.3
<b>Ice Shelves (Total)</b>	<b>1.5</b>	<b>0.7</b>	<b>&lt; 1</b>

## 1.2 Glaciological Terminology

It is important to understand the terminology used in this area of glaciological research called *radioglaciology*. The term *ice sheet*, in particular, refers to a large, continental area of compacted ice over land, typically directly over bedrock. Ice sheets can cover loose material, subglacial lakes, and bedrock. The term *ice shelf* is used to refer to ice flows over water, typically having flowed from the larger ice sheet to an offshore region across the *grounding line* that divides the sea from the continental area. *Icebergs* and some forms of *sea ice* are portions of ice shelves that have broken off of the shelf and

moved into the sea. The process of ice sections separating from the ice shelves due to the internal stresses and moving into the sea is known as *calving*.

The ice sheets contain both solidified ice, which is the compacted snow accumulation, and an upper layer of fresher snow. *Firn* is snow that has been recrystallized to some extent and is in an intermediate stage between fresh, new snow and compacted glacial ice [USGS, 2012]. Firn is generally the top 50 to 100 meters in which the snow begins to compress and recrystallize. The transition to ice is generally considered to occur, by convention, when firn reaches a density of  $830 \text{ kg/m}^3$  [USGS, 2012]. The depth at which the transition occurs is generally related to the local temperature cycling. In more temperate regions where there are freeze and thaw cycles, seasonally, the transition typically occurs within a depth of approximately 20 meters [Daniels, 2004]. In areas that rarely see temperatures above freezing, such as West Antarctica, the depth of the firn layer has been reported to reach 60–70 meters. In the East Antarctic, soundings have shown firn depths to 100 meters [Daniels, 2004] before the firn fully compacts to form solid glacial ice. While it may seem a particularly esoteric point, the distinction between solid ice and firn is critical to understand because of their vastly different electromagnetic properties due to the crystalline structure of the ice.

### 1.3 Mass Balance and Cyclical Changes

Ice sheets and ice shelves are not static entities. They exist in a continual cycle of change that can be characterized by a mass balance equation [USGS, 2012]. New ice is formed when precipitation — snow — is deposited and compacts over time to form firn and subsequently recrystallizes to solid ice. The compaction process is driven by recrystallization of the moisture within the snow from thermal and, predominantly, pressure-driven processes. Ice is removed from the mass balance of the sheet as it flows to the sea and calves to form sea ice; experiences seasonal surface melting and subsequent runoff; basal

melting under the ice sheet due to pressure and friction, or is ablated from the surface due to insolation; i.e. solar flux. These changes in the ice sheet are typically both seasonal and long term. Seasonal changes are observed more in temperate glaciers and in Greenland, whereas the Antarctic ice sheet experiences much less seasonal cycling. The extents of the Greenland ice sheet recede significantly in the warm season and grows in the cold season.

Changes in glacial mass from a net balance over a cycle of time are being observed. But, to simply say that the Earth is warming and that ice sheets therefore are melting is not sufficient for the scientific community. Data must be obtained for the specific patterns and rates of ice melt, particularly on the periphery of the sheet and at the ice shelves where the changes are most severe. These patterns and rates can vary significantly over short time scales due to weather, geography, ocean currents, etc. Patterns of ice melt of major ice sheets and ice shelves translate directly to sea level rise [Bentley, 2007] as they are leading indicators of the trend and must be studied with sufficient precision as to determine the patterns and trends. In particular, it is important to separate factors and effects that are long term trends and are not cyclical from long-term trends that are cyclical and “normal” for the climate.

There are two typical means of determining the melt rates of ice sheets and ice shelves. The primary means of high accuracy measurements is to drill ice cores into the ice sheet to measure the thickness of the ice directly through the bore-holes and to determine the specific content of the water contained within the stratified layers of ice accumulation within the core samples. Study of the mineral content of the ice core samples yields valuable information about the geologic record. Analysis of the mineral content and dissolved CO<sub>2</sub> and O<sub>2</sub> content can reveal information about global and sea temperatures over a record stretching back thousands of years.

While ice core samples are a valuable tool, the drilling and study of cores on the large scale required to precisely map global ice sheet thicknesses and thus ice sheet and ice shelf melt rates is cost-prohibitive

and cannot be completed on a sufficiently large spacial area within the seasonal window to provide the information desired by glaciologists. Other methods must be employed to gather high-precision melting data over large spacial areas to asses the big picture.

On the other end of the quantity-vs.-quality spectrum of measurement options is aerial radar measurements. Rough data about the basal terrain and ice sheet thickness can be obtained using high altitude radar surveys and gravitational measurements. This data, however, does not have the resolution to detect localized ice melt rates over short time scales.

To fill the void between precise-yet-costly ice core sampling and coarse estimates of melt rate from satellite imagery and high altitude radar surveys, ground-based, high-accuracy ice-penetrating radar systems can be employed to determine ice sheet thickness and, over time, to determine the melt rate thereof. Determining the rate of melt over short time periods requires high accuracy measurements in order to extrapolate long term melt rates. Satellite measurements of the Antarctic ice shelf show thinning on the order of up to 5.5 meters per year over the last decade [Bentley, 2007] [Shephard, 2004]. This translates to thickness changes — in ice sheets with thickness on the order of kilometers — of only 1 to 2 mm per day. It should also be noted that in temperate regions where there is significant seasonal cycling, this could mean higher melt rates in warm periods and lower melt rates in cold periods.

## 1.4 Ice-Penetrating Radar Concept of Operations

It is important to define the Concept-of-Operations (CONOPS) for the measurement system that is the topic of this thesis. Such an understanding ensures that the instrument developed will be both technically capable of fulfilling the scientific objectives for the system and can be used in a reasonable manner in the field. A precision laboratory Vector Network Analyzer (VNA), for example, meets the technical needs of the scientific measurement but is ill-suited for the measurement campaign because of the cost of

deploying many measurement sets and because the harsh conditions in which it must operate are far outside of those specified for laboratory-grade equipment. The CONOPS drives the system requirements.

The primary CONOPS for the radar developed in this thesis is one where the system is used seasonally for ice shelf thickness measurements during observational campaigns at the glacial sites. The radar is not intended for permanent installation.

In this option, the research team will go to the ice sheet on plane specially equipped to land on the ice. The team will have access to the aircraft to go to the measurement site for several week-long campaigns separated by approximately one week each. The radar will be placed at preselected locations on the ice shelf and soundings using the radar developed in this thesis will be recorded. The team will then place bamboo marker flags indicating the position of the radar measurement to compare to future thickness soundings. GPS position may or may not be recorded depending on the difficulty of securing high-precision GPS position fix data in polar regions.

Another option for the glaciology team would be the long-term installation of a low-cost, low-power radar that could be placed at the sounding sites at the start of a measurement campaign to collect data over the several-week observation period. The radar system would be left to automatically collect data at preselected intervals (e.g., every 10 minutes, once an hour, etc.). Particularly for ice shelves over the sea, this would allow the correlation of melt rate to very short term phenomena like tidal activity or ocean currents if one assumes that the radar can be made with sufficient resolution to observe such changes. This is in contrast to the two-week measurement interval if the radar must be taken with the team — moving large, costly, single-shot radars into position for each measurement window. Design of a radar with sufficient resolution to measure changes on a daily basis is difficult, although the work of this thesis indicates through simulation and analysis that it is possible. It is yet experimentally unproven if this method provides any practical advantage over the two-week-spaced campaigns.

Past work has found that the use of precise phase-measurement-based radars can discriminate 1% of a wavelength under certain assumptions and used a center frequency of 300 MHz and had bandwidths of 60 MHz to 160 MHz [Jenkins, 2003].

## 1.5 Contribution of this Thesis

The work presented in this thesis advances the development of a very-low-cost Vector Network Analyzer (VNA) based radar system that is capable of measuring ice thickness in sufficient resolution and stability over time to determine the melt rates of glacial ice in short measurement campaigns. The work presents a system-level description of the radar and the requirements. Analysis of the design tradeoffs is provided and design tables showing tradeoffs in component or subsystem selection are provided so that future users of this instrument can modify the system design presented in this thesis to meet their particular design requirements. Design files for fabrication of completed systems are also provided.

The design developed within this work will enable glaciologists to make many ice-sheet and ice-shelf thickness measurements at very low cost, possibly with ongoing and continuous data, in the polar regions. This ice thickness data will allow glaciologists and climate scientists to study the cyclical melt rates of ice sheets and ice shelves and separate short-term cyclical changes from the long-term trends using very high accuracy thickness measurements from a wide variety of locations.

## 1.6 Overview of Thesis

This thesis is structured to present the work in a manner that is logical and understandable to a technical audience familiar with radar systems and RF design but that is not necessarily expert in the details of VNA design and calibration or in the use of a VNA for a radar system.

In this introductory chapter, basic glaciological terminology and the motivation for conducting radar sounding of glacial ice thickness has been presented without discussion of the specific technical methods of the radar system or the design. This chapter also discussed the CONOPS for a glacial ice thickness measurement campaign as it will impact the system requirements.

In *Chapter 2: Background*, the background of how ice-penetrating radar systems operate and different radioglaciology techniques are discussed. The chapter begins with a discussion of the evolution of radioglaciology techniques from a historical perspective. Next, a background in the electromagnetic properties of ice and snow, which affect the radar system design, are presented. The work then explores the types of radar systems that are capable of making ice thickness measurements. The thesis then looks at how parameters of an ice-penetrating radar system and the radar's particular figures of merit affect its accuracy. Finally, requirements for the system are discussed and a block diagram of the radar system is presented.

In *Chapter 3: Vector Network Analyzer Background*, the background theory of VNA operation is discussed in detail. A systems-level overview of the VNA is presented with block diagrams. Each subsystem block is then explained in some detail with particular emphasis on the VNA subsystems that directly impact that performance of the VNA for this application — affecting the phase accuracy. In this section, a detailed analysis of the calibration theory is also discussed as this will be critical to the successful use of the VNA for high-precision ice thickness measurements. The development of VNA background constitutes the bulk of this work.

In *Chapter 4: Antenna Design*, the analysis, design, and selection of the antennas for the radar system is presented. The radars receiving and transmitting antennas play a vital role in the successful system implementation. An analysis is presented of commercial off the shelf (COTS) antennas that are available to the university glaciological research team.

In *Chapter 5: VNA Design implementation*, the specific VNA design is discussed. First, a discussion of the COTS, low-cost VNA — the original basis of this design — is presented complete with an analysis of its overall shortcomings. Following that, specific redesigns of several of the system blocks is presented complete with analysis and bench testing of the subsystems.

In *Chapter 6: Conclusions*, results of some bench-testing and brass-board prototyping are discussed. Recommendations for future work and implementation of this research conclude the thesis.

## **CHAPTER 2: BACKGROUND**

Recognizing that there is a scientific motivation to conduct high-accuracy measurements of ice thickness, the focus of research shifts to the best way in which to make such measurements in a practical sense. The critical factors in the development of a remote sensing radar for ice thickness measurement purposes are the accuracy of the radar, the reliability of the radar in harsh arctic conditions, and the cost of the system.

There are several types of radar remote sensing measurements that can be used to determine the thickness of glacial ice. When these measurements are made over time, they can be used to determine the change in thickness and thus the melt rate of the ice shelves and continental ice sheets. Additionally, the changes in thickness, when referenced to the internal layering, can be used to determine the flow of the ice.

This chapter explores the types of radar systems that are capable of making ice thickness measurements. The discussion begins with a review of the history of the development of ice penetrating radar systems in *2.1: Historical Context*. Understanding how the accuracy of such radars advanced over time provides insight into the motivation for this thesis. Next, general background on radar remote sensing and the parameters discussed in later chapters is provided briefly in *2.2: General Radar Remote Sensing Principles*. The electrical and electromagnetic properties of ice and snow are discussed in *2.3: Electromagnetic Properties of Ice and Snow* to provide background on how radar systems interact with these media. Finally, the way in which key parameters or performance metrics for radar systems impact the accuracy and usability of a radar for ice thickness measurements is discussed in *2.5: Considerations for an IPR System*.

In general this chapter discusses the radar system required for ice thickness measurements functionally, abstracted from the specific implementation of the hardware and software. The information is presented

in such a way as to provide background context for the research and a review of pertinent literature on ice penetrating radar systems. Later chapters of this thesis address the specific, practical implementation of the antennas, radar electronics — the VNA itself — and processing software.

## 2.1 Historical Context

The origin of depth sounding of glacial ice and snow can be traced to early flights over polar regions by military pilots in the 1930s–1940s. In a specific reported incident in 1946, a US Air Force pilot documented that radar altimeter measurements taken over glacial ice sheets in the Antarctic did not provide true altitude indication and that the readings should not be trusted by future pilots [Waite, 1962]. Based on the reports of that pilot, and subsequent reports from other flights, US Army researchers operating from the US Army Signals Research Lab at Fort Monmouth, NJ (Amory H. Waite and his group) theorized that ice may be effectively transparent to radar signals.

Additional propagation studies not specifically related to depth sounding of ice were conducted in 1946 through 1955 for US Army radar research purposes. A review of the cumulative results from those studies led Waite's team to conduct the first reported experiments directly on the use of radar remote sensing of ice sheet thickness in 1957 using a standard aircraft SCR-718 radar altimeter operating 440 MHz [Waite, 1962]. Results were first publicly presented in 1961 and published by the Institute of Radio Engineers (IRE) in 1962 [Waite, 1962]. The SCR-718 used by Waite is a pulsed radar operating at 7 watts transmit power [Weber, 1970]. Waite's experiments were conducted as an airborne radar from an Air Force plane. For the radar measurements interpretation, an oscilloscope was used as the display instrument and the horizontal timebase display is adjusted to calibrate to depth using assumptions — initially very coarse — about the velocity of propagation of electromagnetic waves in ice.

Based on the work by Waite and Schmidt at Fort Monmouth, the Scott Polar Research Institute (SPRI) at

Cambridge University developed several VHF remote sensing systems specifically for radar sensing — often referred to in older literature as radio-echo sounding — of the depth of glacial ice. The work at SPRI, complete by Evans et al.; began in 1963. Important results on the accuracy of depth sounding of Antarctic glaciers were published by that group, including descriptions of the pulsed VHF radar system [Evans, 1969]. Other VHF pulsed radar systems followed, each demonstrating the feasibility of radar remote sensing of the glacial ice thickness using various frequencies in the VHF band from 30 MHz to 620 MHz.

The earliest work first focused on the Antarctic ice sheet. Later published — although largely based on research that was conducted in parallel to the work of Evans — was work looking at the Greenland ice sheet thickness. Some of the most pioneering of this work was conducted by Gudmandsen et al; at the Technical University of Denmark Laboratory of Electromagnetic Theory and reported on in 1969 [Gudmandsen, 1969]. Greenland is an independent country in the Kingdom of Denmark and therefore most early study of Greenland ice sheets was conducted by Denmark.

In 1965 a Canadian periodic survey campaign, initiated originally in 1962 to measure ice sheet thicknesses on Baffin Island, also began conducting radar ice thickness soundings. The work reported by Weber and Andreiux [Weber, 1970] was also based on measurements using an unmodified SCR-718 radar altimeter. The SCR-718, on-loan from the Canadian Royal Air Force, was mounted on a sled with 440-MHz parabolic section reflector antennas. The sled was then pulled slowly across the ice by a “motor-toboggan”. The radar has a resolution of  $\pm$  15 m of ice thickness, limited by the oscilloscope display sensitivity being used to measure the radar returns. The soundings on Baffin island provided important results that demonstrated that more temperate ice thickness can also be measured, in addition to the polar results in the Antarctic. As is discussed later, the type and temperature of the ice plays a key role in the electromagnetic properties of the ice and the effectiveness of radar signal penetration due to the

temperature dependence of attenuation.

In 1975, the radar measurements of thick polar ice sheets were correlated to gravitational measurements and more traditional geological seismic and bore-hole measurements conducted in East Antarctica. The comparison was conducted by Drewry et al [Drewry, 1975]. Of particular interest was determining the accuracy of the assumption about propagation velocity in various types of ice, both the density of the compaction and the temperature impact the  $\epsilon$ , as is discussed in 2.3: *Electromagnetic Properties of Ice and Snow*, and those assumptions are directly related to the accuracy of thickness measurements. Drewry found good agreement between all types of measurements but did find significant variability in the velocities of propagation when compared to bore-hole techniques based on the ice density and, to a lesser extent, the temperature [Drewry, 1975].

## 2.2 General Radar Remote Sensing Principles

Radar measurements, in general, are form of remote sensing in which an electromagnetic wave is launched from a transmitter, interacts with a target in some way, and then then some portion of the transmitted wave travels to a receiver. The time it takes the waves to travel to the target and then to the receiver along with the nature of the scattered signal allows the radar to infer parameters about the nature of the target.

To the first order, conventional ground penetrating radar (GPR) systems and special case of GPR that is ice-penetrating radar sounding of ice depth — finding the bottom of the ice — is essentially a time domain reflectometry (TDR) measurement [Peters, 1994]. That is to say, the primary purpose is to measure the gross distance to some reflector — the scattering body — by measuring the time that is required for the leading edge of the transmitted radar pulse to reflect back to the radar and then calculating the distance by from that round trip time using assumptions about the velocity of propagation

to the scattering target and back.

This all works quite nicely in a well-behaved medium like air or a homogeneous liquid. In mixed and stratified solids like earth and glacial ice, however, just determining or estimating the velocity of propagation requires a reference for comparison or *a priori* knowledge of the dielectric properties of the medium such as the electric permittivity, the magnetic permeability, and the conductivity for all the media that the wave travels through. Without such knowledge, certain assumptions must be made about the round-trip propagation path. Some of these assumptions can then be verified using other remote sensing techniques. Fortunately, much work on the electromagnetic properties of glacial ice has been completed and subsequently verified by the scientific community long before the work presented here began, allowing this thesis to make use of reasonable and prudent assumptions about the electromagnetic properties of ice when necessary. This is discussed further in Section 2.3: *Electromagnetic Properties of Ice and Snow*.

Traditional GPR — the general case of which IPR is a subset — uses wideband pulsed radar with pulse widths on the order of several nanoseconds and Pulse Repetition Frequency (PFR) from 1 to 100 kHz. The short pulse duration is used to allow blanking of the receiver system during transmission to avoid saturating and damaging the sensitive receiver circuitry with the high power of transmission pulse. The downfall of this technique is that it requires extremely high power levels to produce a strong enough return to be effectively detected by the receiver. This is the case for earth, though. Ice provides a very different set of challenges. The sections of this document which follow explore some known and published techniques for sounding of thick ice using radar remote sensing.

### 2.2.1 Radars for Snow Thickness

On the top of any glacial ice is a layer of fresh snow and firn that has begun to compact and recrystallize

into solid ice. Because it is the top layer, it seems logical to address sending of the snow pack first.

Radar have been developed to measure strictly the snow accumulation and thickness of the snow pack and firn. These radars tend to operate at higher frequencies to provide more detailed resolution of the stratification. The higher center frequency allows antenna arrays of practical size for aircraft to develop higher in-band aperture and thus sharper gain. The recent stratification is of specific interest to the scientific community [Panzer, 2010]. The radars were developed primarily by NASA and University of Kansas Center for Remote Sensing of Ice Sheets (CreSIS) [Ramasami, 2003]. The improved snow radar system that followed — developed by Panzer, Leuschen, Patel, Markus and Gogineni — are examples of FM types radars. The latest system developed at CReSIS transmits linear chirps of 2 GHz to 6.5 GHz over a 240 microsecond pulse and a PRF of 200 kHz [Panzer, 2010]. The system had an overall thickness resolution of 5.5 cm using the sampling hardware of that system.

## 2.3 Electromagnetic Properties of Ice and Snow

All materials have particular electromagnetic properties that affect the propagation of electromagnetic waves. These properties must be understood when using radar to perform remote sensing in or through those materials. This is particularly important in the case of GPR and IPR measurements where the media that the wave is traveling though is not simplistic, well-behaved, quasi-homogeneous air as in many atmospheric remote sensing applications.

Earth materials encountered in GPR can be extremely *lossy* — highly attenuating the wave passing though the materials — making radar sounding of the target difficult. Ice is less lossy than most earthen materials but the attenuation is not negligible. Earth materials like silt, sand, and rock, particularly when those materials contain highly-polarizable liquid water, present high electromagnetic attenuation. Ice, in contrast to earthen materials, has parameters that permit significant depths of probing [Peters, 1994].

For reference throughout this section, Maxwell's equations in the time domain differential form for heterogeneous isotropic media are [Balanis, 2005]:

$$\nabla \times \vec{E} = -\frac{\partial \vec{B}}{\partial t} \quad (2.1)$$

$$\nabla \times \vec{H} = \frac{\partial \vec{D}}{\partial t} + \vec{J} \quad (2.2)$$

$$\nabla \cdot \vec{D} = \rho \quad (2.3)$$

$$\nabla \cdot \vec{B} = 0 \quad (2.4)$$

Where  $E$  is the electric field strength vector in V/m,  $H$  is the magnetic field strength vector in A/m,  $\rho$  is the electric charge density in C/m,  $B$  is the magnetic flux density vector,  $J$  is the electric current density vector in A/m<sup>3</sup>, and  $D$  is the electric current displacement in A/m<sup>2</sup>.

At high frequencies where dispersion dominates, the general forms of the constitutive relations are given by Equations (2.5) to (2.7).

$$\vec{J}(t) = \int_0^\infty \sigma(\beta) \cdot \vec{E}(t-\beta) d\beta \quad (2.5)$$

$$\vec{D}(t) = \int_0^\infty \epsilon(\beta) \cdot \vec{E}(t-\beta) d\beta \quad (2.6)$$

$$\vec{B}(t) = \int_0^\infty \mu(\beta) \cdot \vec{H}(t-\beta) d\beta \quad (2.7)$$

At frequencies such as those used for GPR and IPR in which dispersion is not a factor, Equations (2.5) to

(2.7) simplify to (2.8) to (2.10), respectively. This form of Maxwell's equations and the constitutive relations are referenced throughout this chapter and in *Chapter 4: Antenna Design*.

$$\vec{D} = \epsilon \vec{E} \quad (2.8)$$

$$\vec{J} = \sigma \vec{E} \quad (2.9)$$

$$\vec{B} = \mu \vec{H} \quad (2.10)$$

The following subsections discuss particular material property terms that appear in the equations above. These are properties of all materials and in this specific research, the material properties of the ice and snow are of consequence.

### 2.3.1 Electric Permittivity

Electrical permittivity describes the ability of a material to store energy — charge — from electromagnetic fields. Some texts, particularly older publications, will refer to the real portion of permittivity as *Dielectric Constant* or  $K$ . In this thesis,  $K$  is not used at any time to refer to relative permittivity and newer literature does not use  $K$ . Permittivity for real-world materials is complex with both a real component given in Equation (2.12) that contributes to the storage of field energy and the imaginary component given in Equation (2.13), which is the loss mechanism for the field energy.

Because the imaginary component of complex permittivity contains a frequency term, the loss mechanism is frequency dependent. In general, the frequency dependence of permittivity is very difficult to deal with computationally when attempting to model in a precise way. Fortunately, the complex permittivity can be computed with simplified models that represent the true complex permittivity to varying degrees of accuracy at different frequencies.

Permittivity is often modeled by the Debye–Relaxation Method, the Cole–Cole method, the Havrillak–Negami Method, and the Djordevic–Sarkar Method. The most common modeling when used in full-wave E/M simulation is a simplified, linearized interpolation of conductivity samples at various frequency points. This typically yields results which error from true permittivity far less than the error resulting from the parasitic effects of practical antenna construction. The Cole–Cole method has also been used for near-field antenna effects of ice and snow in antenna modeling.

Debye–Relaxation Mechanism describes the total permittivity as a real portion and an imaginary portion, both with a frequency dependence. The Debye model is described via:

$$\epsilon = \epsilon_{\Re} - j \epsilon_{\Im} \quad (2.11)$$

$$\epsilon_{\Re}(\omega) = \epsilon_{\infty} + \frac{\epsilon_s - \epsilon_{\infty}}{1 + \omega^2 \tau^2} \quad (2.12)$$

$$\epsilon_{\Im}(\omega) = (\epsilon_s - \epsilon_{\infty}) \frac{\omega \tau}{1 + \omega^2 \tau^2} \quad (2.13)$$

$$\epsilon(\omega) = \epsilon_{\infty} + \frac{\epsilon_s - \epsilon_{\infty}}{1 + j \omega \tau} \quad (2.14)$$

The model makes use of a static permittivity that can generally be thought of as the “DC” component of permittivity and a high frequency limit of permittivity.

An alternative modeling of the frequency dependence of permittivity that is often used in full-wave electromagnetic simulations is the Havriliaka–Negami which is named for the work in [Havriliak, 1967]. The Havriliak–Negami model is a generalized form of the Debye model that allows for  $\alpha$  and  $\beta$  parameters which modify the broadness of the relaxation curve ( $\alpha$ ) and the asymmetry ( $\beta$ ) of the curve.

The Havriliak–Negami model is given by:

$$\epsilon(\omega) = \epsilon_{\infty} + \frac{\epsilon_s - \epsilon_{\infty}}{(1 + (j\omega\tau)^{\alpha})^{\beta}} \quad (2.15)$$

Another specialized model which accounts for a broadened relaxation curve but not asymmetry is the Cole–Cole model first published in [Cole, 1941]. The Cole–Cole model is given by

$$\epsilon(\omega) = \epsilon_{\infty} + \frac{\epsilon_s - \epsilon_{\infty}}{1 + (j\omega\tau)^{1-\alpha}} \quad (2.16)$$

Note that the Cole–Cole relaxation model is merely a special case of Havriliak–Negami where the symmetry parameter ( $\beta$ ) is set to 1, indicating that the relaxation is symmetric. For the case of  $\alpha = 0$ , the Cole–Cole model reduces to the Debye–relaxation model [Cole, 1941]. For the Cole–Cole model,  $\alpha$  typically varies from 0 to 0.7.

### 2.3.2 Magnetic Permeability

The magnetic permeability of almost all ice formations is virtually indistinguishable from that of the vacuum permeability since there are very few ferromagnetic materials in the ice [Olhoeft, 1998]. For almost all IPR applications, magnetic effects have little impact on the propagation and are simplified to the vacuum permeability value of  $1.26 \times 10^{-6}$  H/m in calculations of loss and propagation velocity.

### 2.3.3 Conductivity

The limiting factor on the realistic achievable depth of measurement of IPR, like with most general GPR systems, is the attenuation of the signal traveling through the lossy ice or earth materials. Attenuation generally results from several mechanisms. In casual discussions, some texts lump the reduction in

received signal due to the spreading of the spherical wavefront as it propagates from the transmit antenna and the spreading of the reflected wave as it propagates back to the target. This is not strictly attenuation, although it results in an attenuated received signal. The dominant factor in IPR is the exponential loss with depth in the material due to conversion of the electromagnetic energy into heat in the ice through conduction, dielectric relaxation, or diffusion-limited loss in minerals contained in the ice sheet [Beres, 1991].

Conductivity describes the ability of the material to pass free charge carriers and is highly related to the mineral content of the ice [Olhoeft, 1998]. The chemical and mineral content, particularly acidity, relates directly to the number of free charge carriers available for conduction. The “DC” conductivity is given as  $\sigma_s$  or the static conductivity and represents the low frequency conductivity term associated with the ability of the medium in which the electromagnetic wave is propagating to sustain conduction current. This  $\sigma_s$  term is typically sufficient at lower frequencies such as those at which GPR and IPR are used since the free charge carriers are able to move quickly enough to remain in-phase with the applied electric field and all collisions of the charge carrier with other atoms, ions, or electrons convert some of the field energy into heat in the collision.

At higher frequencies, typically those well above the ones used for GPR and IPR, the conduction currents are no longer able to align to the applied field quickly enough to remain in phase. This translates to an imaginary component of complex conductivity. The physical implication of this complex conductivity is that it contributes to the stored energy component within the medium related to the stored energy component of permittivity [Turner, 1994]. For IPR, the frequencies are sufficiently low that the energy loss of the real portion of conductivity — considering it to be static as  $\sigma = \sigma_s$  — is appropriate.

It should be noted that, for most ice sheets, as is true in the more general case of GPR, conductivity is not a constant and is a function of frequency. Attenuation will, therefore, vary with radar frequency [King,

1981]. For certain narrow frequency bands of interest, particularly above the non-dispersive transition frequency, conductivity can be approximated as constant within that band.

### 2.3.4 Propagation Velocity

The simplified equation for determining velocity in a medium is given by:

$$V_m = \frac{c}{\sqrt(\epsilon_r)} \quad (2.17)$$

Where  $c$  is the speed of light in a vacuum,  $\epsilon$  is the electric permittivity,  $\epsilon_r$  is the dimensionless relative permittivity, and  $\epsilon_0$  is the vacuum permittivity. The computed  $V_m$  is the velocity in the medium. Literature gives the value of  $\epsilon_r = 4$  for typical ice. Applying Equation (2.17) gives a value of 150 m/us. Research has consistently shown a measured propagation velocity fresh water ice sheet of 167 m/μs [Jacobal, 1995] to 168 m/μs [Corr, 2002]. This would imply true  $\epsilon_r = 3.203$  for such sheets. These values are variable based on the acid content of the ice, temperature, and most importantly, the compaction of the ice, i.e. density [Corr, 2002].

$$\epsilon = \epsilon_r \cdot \epsilon_0 \quad (2.18)$$

$$c = 299792458 \frac{m}{s} \quad (2.19)$$

$$\epsilon_0 = 8.854 \times 10^{-12} \frac{F}{m} \quad (2.20)$$

$$\mu = \mu_r \cdot \mu_0 \quad (2.21)$$

$$Z_m = \sqrt{\frac{\mu}{\epsilon}} \quad (2.22)$$

### 2.3.5 Refractive Index and Reflection Coefficient

In the end, the ability of scientists to use IPR to determine the thickness of glacial ice is dependent on using reflections within the ice and off of the bottom of the ice shelf or ice sheet to determine the thickness. These reflections are based on boundaries at which the refractive index of the material — ice — changes, causing a reflection of signal. The amount of signal reflected can be characterized by reflection and transmission coefficients.

Inhomogeneities and discontinuities in dielectric properties lead to reflections [Gogineni, 1998]. The reflections are due primarily to the acid and mineral content of the ice [Beres, 1991]. The strongest reflections will be due to changes from ice to bedrock or ice to liquid water. It has been shown in the literature that the refractive index of ice and firn is linearly related to the density of that ice and density of the ice, to the first order, depends only on depth and is otherwise spatially and temporally constant [Jenkins, 2003].

Internal reflections within the ice sheet or ice shelf are based on inhomogeneities within the composition of the ice. If a sufficiently large inhomogeneity exists, on the order of the scale of a wavelength, the returned scatter may dominate the attenuation [Olhoeft, 1984]. The dielectric properties permitting detection of layering in the ice sheet is made possible by changes in conductivity driven primarily by acidic fallout from volcanic eruptions [Jacobal, 1995] [Kuchikulla, 2004]. This is due to destructively interfering internal echoes [Moore 1998]. *Table 2* provides published data for some of the materials that may produce the discontinuities.

Material	Conductivity [S/m]	Relative Dielectric Constant	Calculated Propagation Velocity [m/μs]
Air	0	1	299.7
Pure Water	~ $10^{-2}$	~ 81	33.3
Ice	~ $10^{-3}$ to $10^{-5}$	~ 4	149.9
Sea Water	~ 4	~ 4	149.9
Dry Sand	~ $10^{-4}$	~ 5	134.1
Silt (Saturated)	~ $10^{-2}$	~ 10	94.8
Clay (Saturated)	~ 1	~ 10	94.8
Sandstone (Wet)	~ $4 \times 10^{-2}$	~ 6	122.4
Limestone (Wet)	~ $2.5 \times 10^{-2}$	~ 8	106.0
Basalt (Moist)	~ $10^{-2}$	~ 8	106.0
Granite (Moist)	~ $10^{-3}$	~ 7	113.3

Table 2: Electrical Properties of Earth and Ice Sheet Materials (Data from [Beres, 1991])

GPR and IPR specifically differ from traditional radar work in three principal ways: the antenna placement and scattering typically do not satisfy the far-field conditions that are implicit in the derivation of the classical radar range equation; there is typically ground interference (loading and premature reflection) in the immediate vicinity of the transmit and receive antennas; and the medium of propagation between the radar and the target is extremely lossy [Peters, 1994]. This attenuation plays a significant role.

Attenuation factor,  $\alpha$ , is given by

$$\alpha = \frac{1}{2} \cdot \sigma \cdot \sqrt{\left(\frac{\mu}{\epsilon}\right)} \quad (2.23)$$

for waves with frequency above the transition frequency to non-dispersive propagation — approximately 4–5 MHz for ice. Splitting the permittivity and permeability of the media into the vacuum permittivity and relative permittivity and vacuum permeability and relative permeability gives

$$\alpha = \frac{1}{2} \cdot \sigma \cdot \sqrt{\left(\frac{\mu_0}{\epsilon_0}\right)} \cdot \sqrt{\left(\frac{\mu_r}{\epsilon_r}\right)} = \frac{1}{2} \cdot \sigma \cdot \eta_0 \cdot \sqrt{\left(\frac{\mu_r}{\epsilon_r}\right)} \quad (2.24)$$

where the former terms reduce to the impedance of free space.

$$\nabla^2 \vec{E} = \mu \epsilon \frac{\partial^2 \vec{E}}{\partial t^2} + \mu \sigma \frac{\partial \vec{E}}{\partial t} \quad (2.25)$$

Where, energy dissipation is the second term of the right hand side and energy stored is the the first term of the left hand side.

$$\nabla^2 \vec{B} = \mu \epsilon \frac{\partial^2 \vec{B}}{\partial t^2} + \mu \sigma \frac{\partial \vec{B}}{\partial t} \quad (2.26)$$

$$\vec{E}(x, t) = \vec{E}_0 e^{j(kx - \omega t)} \quad (2.27)$$

$$\vec{B}(x, t) = \vec{B}_0 e^{j(kx - \omega t)} \quad (2.28)$$

where k is wavenumber and omega is the angular frequency.

Simplifying these terms gives the complex wave number

$$k^2 = \omega^2 \mu \epsilon \left(1 + \frac{\sigma}{j \omega \epsilon}\right) \quad (2.29)$$

phase velocity, in radians per second, is given by

$$v = \frac{\omega}{\Re(k)} \quad (2.30)$$

where the wavelength in meters given by

$$\lambda = \frac{2\pi}{\Re(k)} \quad (2.31)$$

and the index of refraction given by

$$n = \frac{c \cdot \Re(k)}{\omega} \quad (2.32)$$

### 2.3.6 Path Loss through Ice and Snow Media

Based on this understanding of the refractive index, the propagation velocity, and attenuation through the ice sheet, it is possible to calculate the approximate received power at the VNA from the discontinuity in the sheet using the modified Friis transmission equation. The standard form of the equation, for free space, is given by

$$P_R = P_T \left( \frac{\lambda}{4\pi R} \right)^2 G_T G_R \quad (2.33)$$

This equation is typically modified to a more convenient form by expressing the frequency dependence in more convenient units, MHz, the antenna gains in dBi, the powers in dBm instead of watts, and the slant range to the receiver in kilometers instead of meters. This form is given by While meters may be more convenient for IPR, convention of the dB form requires km. Notice that all constants associated with the unit conversions are gathered and lumped into a term converted to a dB quantity.

$$P_{R \text{ dBm}} = P_{T \text{ dBm}} + G_{R \text{ dB}} + G_{T \text{ dB}} - 20 \cdot \log(R_{km}) - 20 \cdot \log(f_{MHz}) - 32.44 \quad (2.34)$$

This can further be modified for the purposes of this thesis by realizing that the slant range to the receiver is actually  $2h$  where  $h$  is the depth of the main reflection. This modified the expression to the form found in (2.35). The constant is then modified from the classic form to include the factor of two, which gives

$$P_{R \text{ dBm}} = P_{T \text{ dBm}} + G_{R \text{ dB}} + G_{T \text{ dB}} - 20 \cdot \log(h_{km}) - 20 \cdot \log(f_{MHz}) - 38.44 \quad (2.35)$$

This form of the transmission equation, though, still assumes transmission through a homogeneous medium of air. To correct the equation for this, the attenuation of the ice and snow must be included as well as a term for the imperfect reflection of the internal discontinuity at the bottom of the ice sheet. From the Beer–Lambert law, the intensity of the wave at a depth  $X$  into the medium will have the initial value multiplied by the exponential of the the attenuation coefficient and the depth.

$$I = I_0 \cdot e^{-\alpha X} \quad (2.36)$$

The loss is modified to be the two way path loss to the ice bottom and back using the term  $h$  for thickness.

$$L = e^{-\alpha 2h} \quad (2.37)$$

Then, similarly to the dB form of the Friis equation, this is converted to dB from of attenuation loss given

by

$$L_{dB} = -17.374 \cdot \alpha \cdot h_m \quad (2.38)$$

Using this term, the Friis equation can then be modified to include the approximate attenuation loss. This form is

$$\begin{aligned} P_{R \text{ dBm}} = & P_{T \text{ dBm}} + G_{R \text{ dB}} + G_{T \text{ dB}} - 20 \cdot \log(h_{km}) - 20 \cdot \log(f_{MHz}) \\ & - 17.374 \cdot \alpha \cdot h_m - 38.44 \end{aligned} \quad (2.39)$$

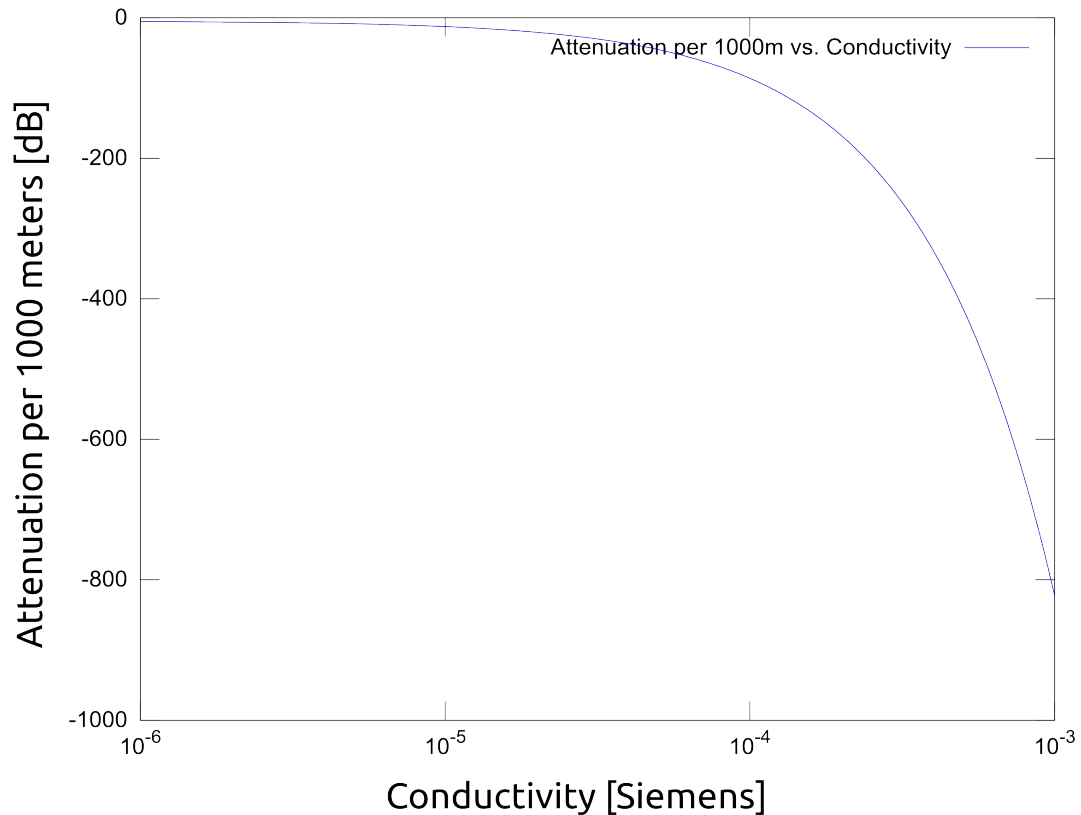


Figure 1: Attenuation of ice for various conductivities from  $10^{-6}$  to  $10^{-3}$

Note that the  $h$  thickness appears inside the log operation for the range term but outside a log term for attenuation since the latter was converted from an exponential eliminating the log term in the conversion to dB. Loss in quantities of dB per thousand meters of travel, not depth, is presented over a wide range of conductivities in *Figure 1* and over a smaller, more realistic range of conductivities in *Figure 2*. Note that this form of the transmission equation assumes perfect reflection off of the lower discontinuities. In practice, there will be additional loss from imperfect reflection.

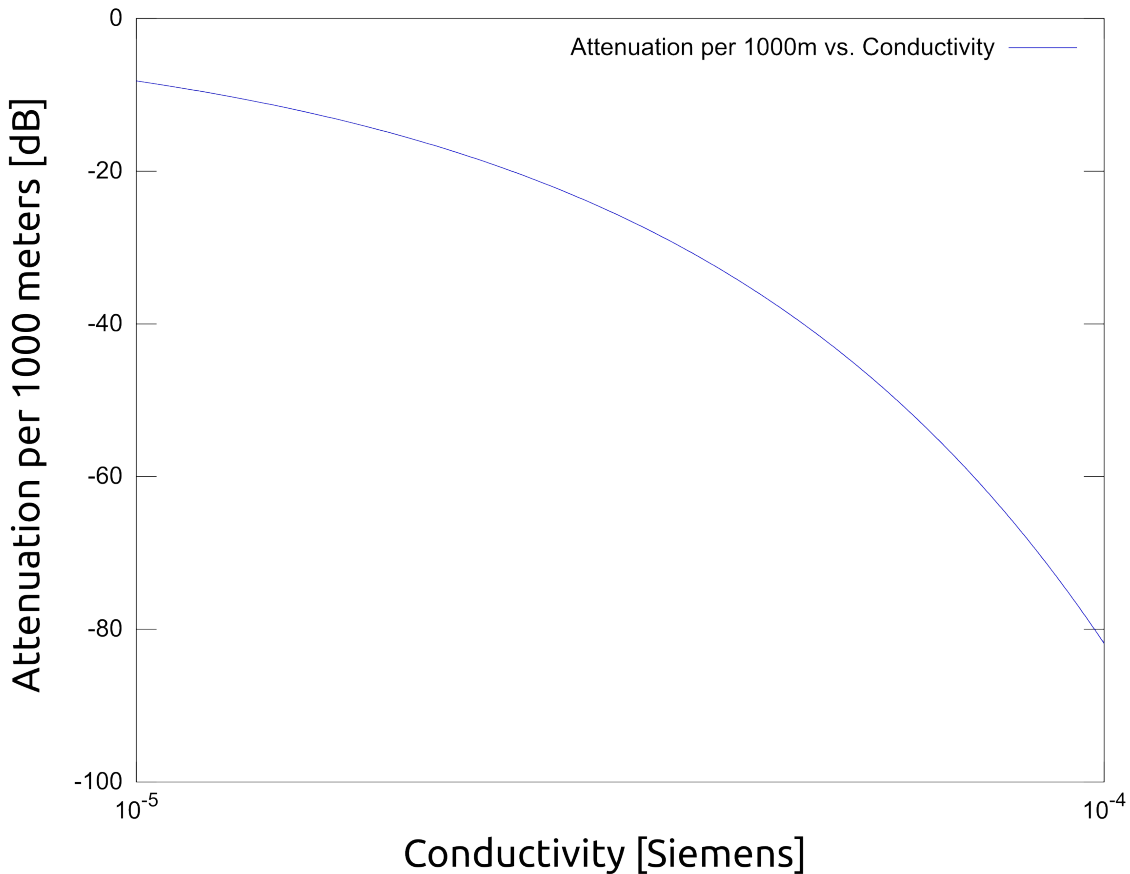


Figure 2: Attenuation of ice for various conductivities from  $10^{-5}$  to  $10^{-4}$

## 2.4 Types of Radars for Ice-Thickness Sounding

There are several different general types of radars that are well-suited to remote sensing measurements of the thickness of ice sheets and ice shelves. Historically, as discussed in 2.1: *Historical Context*, the first ice-penetrating radars used early radar altimeters to determine ice sheet thicknesses. These radar altimeters were simply CW radars. Other types of radar systems that provide improved performance have subsequently been developed. Some of these are discussed in the following subsections and the positive

and negative characteristics of each is explored to determine the best system-level approach for making the ice thickness measurements that are the goal of this research.

#### **2.4.1 Monostatic, Psuedo-Monostatic, and Bistatic Radars**

General types of radars systems can be characterized by the relative locations of the transmitter and the receiver. All radars can be classified as passive, monostatic, bistatic, or multistatic. Some texts make a distinction between monostatic systems and psuedo-monostatic systems.

Passive radar systems are ones in which there is no transmitter and the determination of the position, motion, or nature of the target is based on signals emitted from the target or on scatter of existing “ambient” electromagnetic energy. In arctic environments, when dealing with geophysical phenomena, there is not sufficient ambient electromagnetic energy to make any sensible determination of ice thickness.

A monostatic radar is one in which the transmitter is collocated with the receiver. This is typically the case of GPR and IPR systems. In a technical sense, to be truly monostatic, the radar must transmit and receive with the same antenna to maintain the same aperture position and phase center of the antenna pattern.

A bistatic radar is one in which the transmitter and the receiver are separated by some distance and which distance is comparable to the range to the scattering target being studied. In practice, almost all ground penetrating radars are technically bistatic since the transmit and receiving antennas are usually separated to provide some isolation due to the power levels involved. These radars are generally regarded as being monostatic or psuedo-monostatic since the separation of transmitter and receiver are small fraction of the range to target. Because the separation of the transmitter and receiver is small, the angle subtended between the transmitter to target and the receiver to target is close to zero — a straight, single-shot path.

## 2.4.2 Pulsed and Chirp Radars

Pulsed radar systems, which use short frequency chirp pulses, are common for GPR and IPR systems. Recently published work [Wenpeng, 2012] describes a system that is able to achieve thickness resolutions of up to  $\pm 1$  m in ice sheets up to 3000 meters thick. The radar uses short frequency-modulated chirp pulses centered at 125 MHz and with a bandwidth of 50 MHz. The system transmits at 100 watts. The receiver uses coherent pulse integration to provide high processing gain [Gogineni, 1998]. The PRF used was 4 kHz with pulse widths of 400 ns. The transmitting pulse chirp shaping used a Hamming window.

Dual-receiver configurations have sometimes been used to facilitate higher dynamic range of signal acquisition [Wenpeng, 2012]. High dynamic range systems would be capable of making high resolution measurements of near-surface features — thickness and layering of fresh snow features and partially-compacted firn — while using lower transmit power or a receiver with additional attenuation [Kuchikulla, 2004]. The second, more sensitive receiver would then be used to receive data from deeper features like prominent internal layering and ice sheet bottoms while blanking during the transmit pulse to avoid overloading the receiver. This blanking typically makes detection of near-surface features difficult.

A problem with pulsed chirp radars is the limit of pulsed power available in the bandwidth. In order to increase the bandwidth of the signal, the chirp pulse must be made shorter. However, a smaller amount of energy is transmitted in a shorter pulse for the same output power level. Because of this, the usable penetrating depth of the radar is reduced due to attenuation of the signal from all attenuation mechanisms (i.e., absorption, spherical spread, etc). To compensate for this, the transmit power of the pulse must be increased significantly to maintain the amount of energy within the measurement pulse. For a mobile system, this is not generally practical for reasons of available supply power and the build associated with

high-power-rated components in the transmitter and receiver stages.

### 2.4.3 Frequency-Modulated Continuous-Wave Radar (FMCW)

A way to work around the pulse power limit is to use wideband frequency-modulated (FM) continuous-wave (CW) radar that has long CW pulses that are longer than the transit time to the scattering target and back. This contrasts with typical pulsed chirp radar in which the chirp must be shorter than the round-trip travel time to the target and back.

The FM CW chirp can be made to reject the flash off the surface by use of filtering in the analog portion of the RF front end of the receiver. The front end of most RF radar receivers has an ultra wide dynamic range when compared to the very tight range of the digitizer circuitry.

The CW chirp is typically a linear chirp with a linear increase in frequency. The received scatter back from the target is the frequency. The current transmit signal is mixed with the receive signal providing a mix product with frequency offset beat frequencies. The range to targets is proportional to beat frequency. This gives, in essence, a range-to-frequency converter — the same methodology as standard radar altimeters.

Once the return signal has been converted to frequency products which frequency is proportional to range, it is easy to use inexpensive, Commercial-Off-The-Shelf (COTS) filters with incredibly steep roll-off characteristics if the IF has been properly chosen. The system designer can, in effect, range gate the received signal suppressing surface reflections from snow and surface water and eliminating the transmit antenna to receive antenna isolation problem.

#### 2.4.4 High Phase-Accuracy Network Analyzer Approach

Using magnitude and phase measurements from a network analyzer allows the calculation of both absolute thickness of the ice, either using an Inverse Fourier Transform (IFT) of the frequency domain data or by using two-phase measurements at different frequencies. The network analyzer approach also allows relative measurements of melt between two successive measurements of a single frequency by direct comparison of the phase response.

There are at least two methods that allow the measurement of absolute thickness of the ice to within the desired accuracy. The first approach collects the frequency response of the radar, the transmission  $S_{21}$  measurements, both magnitude and phase. The frequency steps are then operated on by an IFT or Inverse Fast Fourier Transform (IFFT) to produce the response of the ice.

To understand the IFT method, consider that the ideal radar pulse for a very accurate measurement of the position of a reflector or scatter would be infinitely narrow and contain an infinite power. This allows the smallest ambiguity in the range to the reflector or scattering target. The definition, essentially, of an impulse function  $\delta(t)$  in the time domain is such a pulse that is infinitely short but has infinite power and integrates to 1 over all of time.

Recall next that the time domain impulse is used, for among other things, to compute the impulse response of a linear time-invariant system. In this context, the system is the propagation path for the radar signal. This impulse response in the time domain is absolutely equivalent to the frequency response of the system in the frequency domain when transformed by the Fourier transform (or the inverse case of IFT when moving from frequency domain to time domain). The frequency response of the system, magnitude and phase, at all frequencies is thus an equivalent to the time domain response of the system to the infinitely short impulse.

Consider that a fictional, “ideal” Vector Network Analyzer is an instrument that would essentially measure the frequency response of the system, magnitude and phase response, at all frequencies as the VNA sweeps through the spectrum. If the VNA could measure magnitude and phase information for all of the frequency domain, one could then simply perform the IFT on that frequency domain frequency response to obtain the exact time domain response of the system to the impulse.

Of course a practical network analyzer measures in only a finite bandwidth and using a finite number of frequency steps. But this approach is not without merit. Performing the IFT on a set of frequency data with a finite number of discrete frequency steps and with a truncated bandwidth still produces a result which, when transformed into the time domain, approaches that of an impulse response as the number of sample points and the bandwidth grow. This is the fundamental principle that allows the use of the IFT to transform the frequency domain response into an approximate response of the system (the travel path of the radar) to a very, very narrow radar pulse. This is the principle by which all laboratory grade network analyzers that perform time domain measurements (e.g., distance-to-fault measurements) function.

Given certain conditions, a calculation of the thickness of the ice can also be made using the phase response of two discrete frequencies. In this process, measurements are made at two frequencies,  $f_1$  and  $f_2$  with

$$f_2 > f_1 \quad (2.40)$$

The two way distance traveled by the wave,  $2d$ , is some multiple of the wavelength in the medium. The distance traveled by the wavefront is

$$2d = M_1 \lambda_I \quad (2.41)$$

$$2d = M_2 \lambda_2 \quad (2.42)$$

Since  $f_2$  is greater than  $f_1$ ,  $M_2$  is  $M_1$  plus some phase shift  $\varphi$ . In this general case, phase shift  $\varphi$  can be any arbitrary number of radians. It will later be restricted to prevent ambiguous measurements of multiple wavelength differences. Using the relationship between  $M_2$  and  $M_1$  and rearranging (2.41) gives

$$M_2 = M_1 + \frac{\varphi}{2\pi} \quad (2.43)$$

and

$$M_1 = \frac{2d}{\lambda_1} \quad (2.44)$$

$$2d = \left( M_1 + \frac{\varphi}{2\pi} \right) \lambda_2 = \left( \frac{2d}{\lambda_1} + \frac{\varphi}{2\pi} \right) \lambda_2 \quad (2.45)$$

$$1 = \frac{1}{2d} \left( \frac{2d\lambda_2}{\lambda_1} + \frac{\varphi\lambda_2}{2\pi} \right) = \left( \frac{\lambda_2}{\lambda_1} + \frac{\varphi\lambda_2}{2\pi d} \right) \quad (2.46)$$

$$1 - \frac{\lambda_2}{\lambda_1} = \frac{\varphi\lambda_2}{4\pi d} \quad (2.47)$$

$$d(\lambda_1 - \lambda_2) = \frac{1}{4\pi} \varphi \lambda_1 \lambda_2 \quad (2.48)$$

This expression is then solved for the depth  $d$

$$d = \frac{1}{4\pi} \frac{\varphi \lambda_1 \lambda_2}{(\lambda_1 - \lambda_2)} \quad (2.49)$$

and then expressed in terms of frequencies instead of wavelengths

$$d = \frac{\varphi}{4\pi} \frac{\left(\frac{V_m}{f_1}\right) \left(\frac{V_m}{f_2}\right)}{\left(\frac{V_m}{f_1}\right) - \left(\frac{V_m}{f_2}\right)} = \frac{\varphi}{4\pi} \frac{V_m}{(f_2 - f_1)} \quad (2.50)$$

In order for the phase difference measurements between two frequency points to give a valid result when calculating absolute thickness of the ice layer, the frequency points must be sufficiently close in frequency such that the number of whole wavelengths traversed in the medium at the two frequencies is within one wavelength. If the difference is greater than one wavelength, the difference between thicknesses corresponding to phase changes of  $\varphi$ ,  $\varphi+2\pi$ ,  $\varphi+4\pi$ , ... are indistinguishable. Again,  $\varphi$  is the phase difference between the returns at two frequencies  $f_1$  and  $f_2$ .

For a depth  $d$  and a two-way travel of  $2d$ , the absolute maximum resolvable phase change is given by calculating the ratio of  $f_2$  to  $f_1$  at which a signal of  $f_1$  traverses  $M$  wavelengths and a signal of  $f_2$  traverses  $M+1$  wavelengths. This gives

$$2d = M \lambda_1 \quad (2.51)$$

and

$$2d = (M+1) \lambda_2 \quad (2.52)$$

Rearranging these gives

$$\lambda_1 = \frac{2d}{M} \quad (2.53)$$

and

$$\lambda_2 = \frac{2d}{M+1} \quad (2.54)$$

Using these and substituting into the frequency ratio gives

$$\frac{f_2}{f_1} = \frac{\frac{V_m}{\lambda_2}}{\frac{V_m}{\lambda_l}} = \frac{\lambda_l}{\lambda_2} = \frac{\frac{2d}{M}}{\frac{2d}{M+1}} = \frac{M+1}{M} \quad (2.55)$$

Equation (2.51) is then rearranged into

$$M = \frac{2d}{\lambda_l} \quad (2.56)$$

and substituted into (2.55) to give

$$\frac{f_2}{f_1} = \frac{M+1}{M} = \frac{\frac{2d}{\lambda_l} + 1}{\frac{2d}{\lambda_l}} = 1 + \frac{\lambda_l}{2d} = 1 + \frac{V_m}{2df_1} \quad (2.57)$$

If both sides of the equation are then multiplied by  $f_1+1$  the result is

$$f_2 = f_1 + \frac{V_m}{2d} \quad (2.58)$$

Note that the result of maximum frequency spacing does not depend on frequency but only on the velocity in the media — ice — and on the maximum thickness being measured. The range of valid frequency spacings for maximum depths to be measured is given in *Figure 3*.

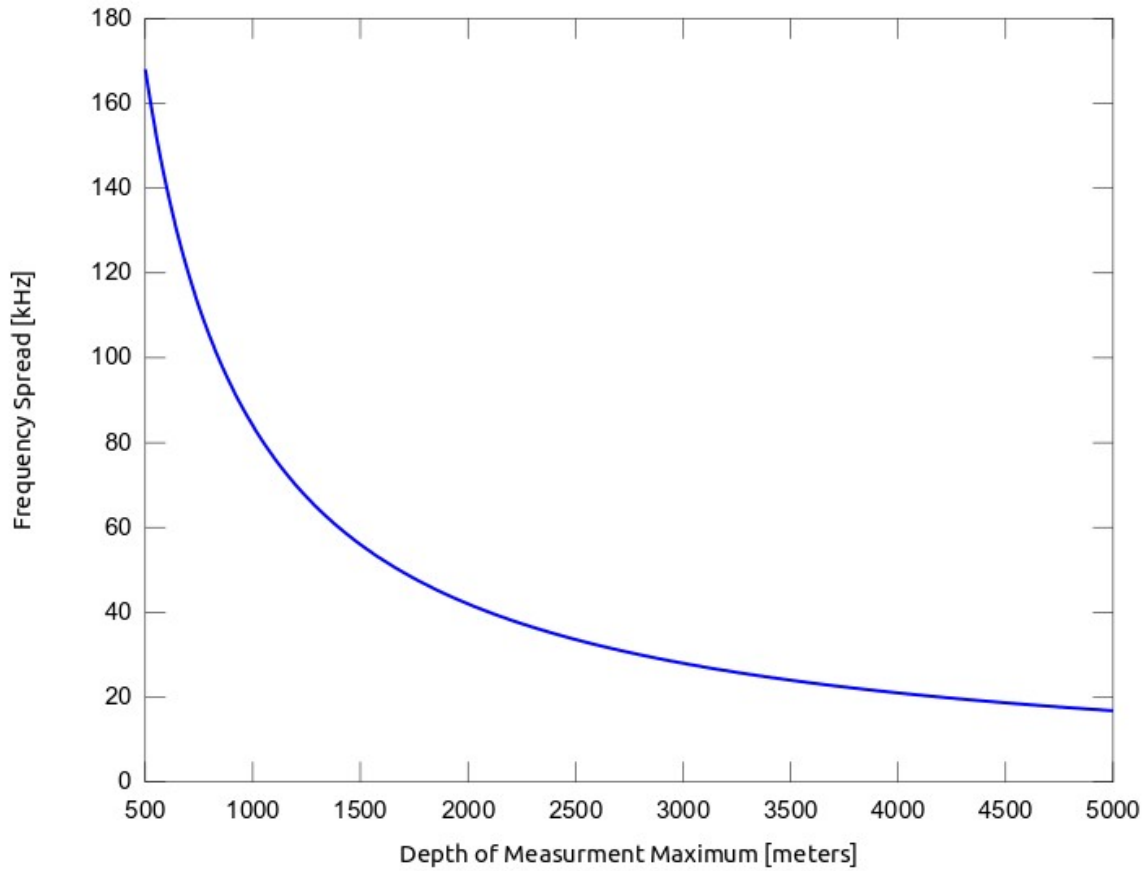


*Figure 3: Resolvable depth calculating sheet thickness based directly on frequency spread*

## 2.5 Considerations for an IPR System

This section details how the theory of operation of ice-penetrating radar systems impacts the practical system design and measurement techniques employed. Basic operating parameters of the system are defined for later use in this thesis.

### 2.5.1 Receiver Power Sensitivity and loss Mechanisms

The sensitivity of the radar receiver used, along with transmit power and antenna performance, determine the usable measurement depth of the antenna. As discussed in 2.3: *Electromagnetic Properties of Ice and Snow*, there are a number of factors in GPR and IPR systems that lead to very high signal attenuation between the radar and the target.

Another factor that leads to signal-level degradation is the time dispersion of the reflected signal wavefront. Consider a quasi-spherical wavefront — which is not perfectly spherical given the angle of incidence at which the wavefront from the antenna meets the interface between the air containing the antenna and the ground or ice medium — impinging on a planar boundary between the ice sheet and the bedrock. A spherical wavefront impinging on a flat surface will produce a return signal with time dispersion as the off-axis signal paths travel a greater distance. This causes a spreading of the signal. This can be compensated for by processing the return data to select the leading edge of the return discontinuities rather than an average or midpoint.

### 2.5.2 Sampling Rate

The sampling rate of the intermediate frequency output of the measurement and reference receivers, from which the magnitude and phase data are recovered from impacts the accuracy of the measurement.

Sampling the IF too slowly for the chosen IF frequency will lead to error, particularly in phase determination, of the magnitude and phase data of the frequency sweep. Errors in the magnitude and phase data translate directly to errors in the IFFT result which give the impulse response of the ice.

### **2.5.3 Implications of Phase Stability and Jitter**

Phase stability and phase jitter impact the accuracy of small-scale, phase-change-based relative measurements of the ice melt rate. If the frequency or phase of the reference oscillator, the PLLs, or the LOs deviates for any given measurement, the measurement results will vary significantly.

For example, when basing thickness change on a phase change between successive measurements at 100 MHz, a 1 degree relative phase error in either measurement results in a 2.3mm depth error. Total thickness measurement error, when using relative phase between successive measurements to determine depth change, is dependent on both depth and the frequency error.

Jitter, referred to as either phase jitter, clock jitter, or phase noise, depending on the literature and context, it is the undesired deviation of true periodicity of a periodic signal in relation to a perfect signal of the same frequency or a reference point in time. Literature quantified the jitter or phase noise components in units of time, phase, or frequency. When characterized as a time quantity, the deviation is described as the seconds, microseconds, or picoseconds of deviation from true periodicity. When characterized as a phase jitter, units of radians per second are typically used. Jitter can also be characterized as a frequency quantity, typically in Hz or mHz of deviation from true periodicity.

The quantification of the jitter measurement is typically specified a Root-Mean-Square (RMS) or peak-to-peak (p-p) quantity for the time domain measurements (i.e., seconds or radians/second) and as a power spectral density over a specified bandwidth (i.e., W/Hz or dB/Hz) when in the frequency domain.

As a broad category, clock jitter can typically be classified as either random jitter or deterministic jitter. Random jitter is the clock uncertainty that arises from the broadband stochastic processes like Johnson thermal noise within system components. While the value of random jitter superimposed on the true clock signal is technically unbounded, it is also Gaussian distributed and so averaging of an infinite number of clock cycles will cause the average period and phase to converge to the mean value with mean jitter approaching zero. In practice, a large number of averaged samples will reduce, if not eliminate, the effect of the random jitter on the clock performance.

Deterministic jitter is a periodic variation superimposed on the true reference signal and is generated by something within or interacting with the system. Deterministic jitter is either periodic or aperiodic but with a correlation to signals within the system or interacting with the system. Periodic deterministic jitter is characterized, unsurprisingly, with a specific discernible period and is typically correlated to system clocks (e.g., digital-electronics clocks within the system, serial data clocks, switching power supply noise coupled into the clock lines, etc). Aperiodic deterministic jitter does not have a discernible regular periodicity and is typically correlated to digital data lines within the system (e.g., serial data controls).

Sometimes jitter and phase noise are described as being either correlated or uncorrelated jitter. Correlated jitter is jitter that is statistically correlated to other signals within the system and can typically be abated by careful design practices such as good clock distribution technique, groundplane techniques, and shielding of subsystems at the PCB level. Deterministic jitter correlated jitter. Uncorrelated jitter is not correlated to any other signals within the system. Random jitter is always uncorrelated because it is not statistically relatable in any way to signals within the system.

#### **2.5.4 Phase Measurement Reference Selection**

A source of error that must be considered is the careful selection of a phase reference point between any

two successive measurements if direct phase differential is used to calculate the the change in thickness. If one wishes to obtain the highest resolution measurement of a changes in ice layer thickness, the reference phase of the antenna should be set such that the zero crossing of the sine wave is the initial measurement and the second measurement produces some small change from that. This is due to the fact that, for a fixed minimum resolvable amplitude change, in this case the discretization of the ADC, a larger phase change — indicating a larger ice thickness change — is observed near the zero crossing where the slope of the sine wave is maximum rather than the peak of the sine wave where the slope is minimal. The simplified relationship between the ADC resolution in bit and the minimum resolvable angular change between successive measurements for an arbitrary reference is

$$\Delta\phi = \arcsin(V_0) - \arcsin(V_0 - \frac{1}{2^b}) \quad (2.59)$$

In this relationship,  $V_0$  is the reference of a unity amplitude sine wave and  $b$  is the number of bits of ADC resolution.

*Table 3* shows tabulated values for the minimum resolvable angles for popular ADC resolutions near the zero crossing and near the peak of the sine wave. *Table 4* shows the angular implications of the angular resolutions for various frequencies of operation, assuming a velocity  $V_m = 168$  m/μs [Jacobal, 1995] within the ice sheet.

<b>Bit ADC Resolution</b>	<b>Levels of Discretization</b>	<b>1 LSB</b>	<b>Change in Phase for 1 LSB at 0 Degrees</b>	<b>Change in Phase for 1 LSB at 90 Degrees</b>
8 bits	256	$3.91 \times 10^{-3}$	0.223	5.065
10 bit	1024	$9.76 \times 10^{-4}$	0.056	2.532
12 bit	4096	$2.44 \times 10^{-4}$	0.014	1.266
14 bit	16384	$6.10 \times 10^{-5}$	0.004	0.633
16 bit	65536	$1.53 \times 10^{-5}$	0.001	0.316

*Table 3: Phase Resolution by ADC Bit Depth and Reference Phase*

<b>Bit ADC Resolution</b>	<b>Levels of Discretization</b>	<b>1 LSB</b>	<b>Change in Phase for 1 LSB at 0 Degrees</b>	<b>Change in Phase for 1 LSB at 90 Degrees</b>
8 bits	256	$3.91 \times 10^{-3}$	0.223	5.065
10 bit	1024	$9.76 \times 10^{-4}$	0.056	2.532
12 bit	4096	$2.44 \times 10^{-4}$	0.014	1.266
14 bit	16384	$6.10 \times 10^{-5}$	0.004	0.633
16 bit	65536	$1.53 \times 10^{-5}$	0.001	0.316

*Table 4: Ice Sheet Thickness Resolution by ADC Bit Depth and Reference Phase*

## 2.6 System Level Block Diagram of Proposed Approach

Figure 4 presents the overall block diagram of the approach at a systems level. More detail on individual subsystems can be found in the relevant sections of this thesis.

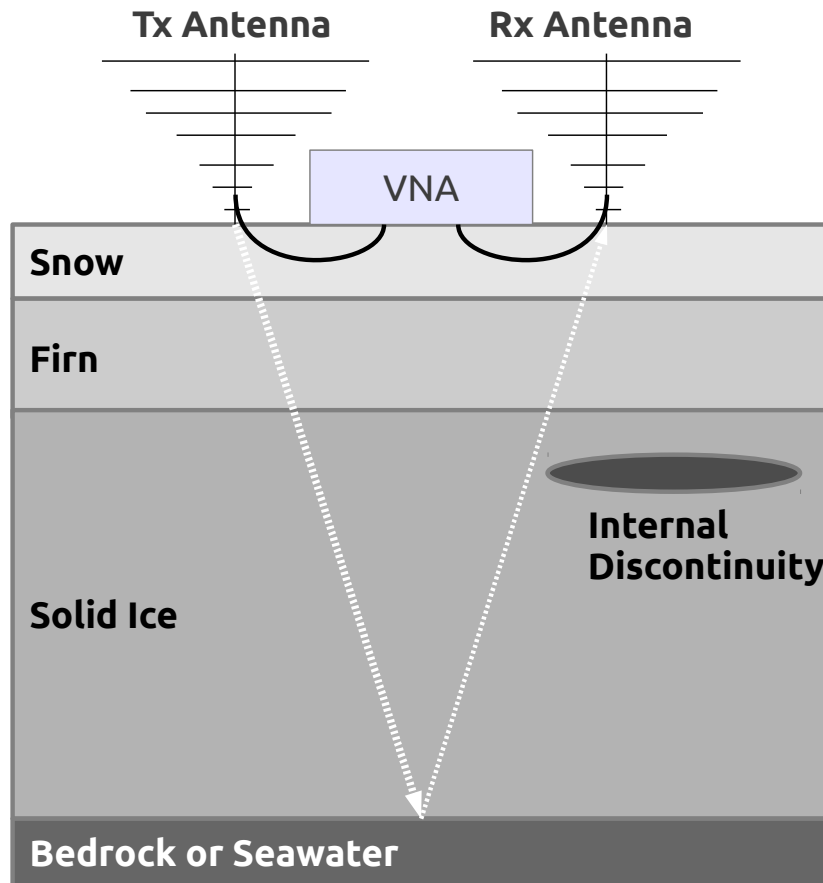


Figure 4: Ice-Penetrating radar block diagram

## 2.7 System Functional Requirements

Most specific requirements of the system were left to the author by the university researchers directing this thesis. The principal requirement of the system is to be able to measure the thickness of an ice sheet of 2-km thickness in 1-mm resolution to facilitate measurement of melt rates over relatively short time scales. Achievement of the 1-mm resolution is practical as we demonstrated in [Corr, 2002]. Particular observations of melt rates have shown that changes on the order of  $2.78 \pm 0.08$  m/yr can be expected. This, if averaged over a year — an unrealistic assumption — would equate to 7.72 mm/day. With a measurement resolution of 1 mm, changes would be observed in a period of as little as 187 minutes of observation.

*Table 5: Abbreviated System Requirements*

Num	Name	Requirement Text	Source
1	Thickness Resolution	The system shall be able to resolution the thickness change in the ice sheet between two successive measurements to less than $\pm 1$ mm.	Driven by the scientific objective.
2	Long Term Frequency Stability	The system long-term aging stability of shall be such that differential thickness resolution drifts by less than $\pm 1$ mm/year.	Driven by the scientific objective.
3	Operating Frequency Min	All system components shall be designed for operation as low as 50 MHz without damage or significant performance degradation.	Driven by the scientific objective.
4	Operating Frequency Max	All system components shall be designed for operation as high as 500 MHz without damage or significant performance degradation.	Driven by the scientific objective.

5	Minimum Operating Temperature	All system components shall survive exposure to temperatures up to 125°C.	Standard environmental parameters per MIL-STD-810G and MIL-HDBK-310 for the region of operation.
6	Maximum Operating Temperature	All system components shall operate in exposure to temperatures up to +85°C.	Standard environmental parameters per MIL-STD-810G and MIL-HDBK-310 for the region of operation.
7	Minimum Non-Operating Survival Temperature	All system components shall survive non-operating exposure to temperatures down to -46°C.	Standard environmental parameters per MIL-STD-810G and MIL-HDBK-310 for the region of operation.
8	Maximum Non-Operating Survival Temperature	All system components shall survive non-operating exposure to temperatures up to +125°C.	Standard environmental parameters per MIL-STD-810G and MIL-HDBK-310 for the region of operation.
9	Maximum Power Consumption	The system components shall operate without degradation while consuming not more than 500 mA DC power at 5V nominally.	Driven by measurement condition
10	Minimum Supply Voltage	The system components shall operate without degradation while with power at a voltage not less than 4.5 VDC.	Driven by USB interface specification
11	Maximum Supply Voltage	The system components shall operate without degradation while with power at a voltage not more than 5.5 VDC.	Driven by USB interface specification
12	Corrosion Resistance	The system components should be designed with standard best commercial practices to ensure no corrosion occurs in normal conditions.	Standard environmental parameters per MIL-STD-810G and MIL-HDBK-310 for the region of operation.

13	Immersion	There is no specific provision for survivability in liquid immersion.	Standard environmental parameters per MIL-STD-810G and MIL-HDBK-310 for the region of operation.
14	Shock and Vibration	The system components shall survive standard commercial carrier transportation shock and vibration condition to the measurement area.	Standard environmental parameters per MIL-STD-810G and MIL-HDBK-310 for the region of operation.
15	Maximum Mass	The mass of any unit component of the system shall not exceed 25-kg.	All system component must be portable by one person without assistance.
16	Maximum Operating Humidity	All system component shall survive, without damage or degradation, prolonged operating exposure to relative humidity as high as 100%	Standard environmental parameters per MIL-STD-810G and MIL-HDBK-310 for the region of operation.
17	Minimum Operating Humidity	All system component shall survive, without damage or degradation, prolonged non-operating exposure to relative humidity as low as 0%	Standard environmental parameters per MIL-STD-810G and MIL-HDBK-310 for the region of operation.
18	Maximum Non-Operating Survival Humidity	All system component shall survive, without damage or degradation, prolonged non-operating exposure to relative humidity as high as 100%	Standard environmental parameters per MIL-STD-810G and MIL-HDBK-310 for the region of operation.
19	Minimum Non-Operating Survival Humidity	All system component shall survive, without damage or degradation, prolonged non-operating exposure to relative humidity as low as 0%	Standard environmental parameters per MIL-STD-810G and MIL-HDBK-310 for the region of operation.

## **CHAPTER 3: VECTOR NETWORK ANALYZER BACKGROUND**

In this chapter, a general background is discussed and the theory of operation of Vector Network Analyzers (VNA) is explored including how various design and construction choices affect the performance of the VNA for magnitude, phase, and time domain measurements. The purpose of this chapter is to provide the context for later chapters that describe the specific VNA implementation for readers who are not familiar with the details of VNA system design. This chapter is the result of significant literature review on the design of a VNA and its subsystems. Design equations are presented in this chapter rather than as a matter of implementation in later chapters.

A VNA is a subclass of instruments known as a network analyzer. The general network analyzer is a device that is used to characterize the response of a circuit — specifically a linear network — to signals of various frequencies. A network analyzer can be a scalar type which measures only the magnitude response of a circuit to stimuli of various frequencies. In practice, scalar network analyzers are rarely used in modern test and measurement. As a newer class of network analyzers, modern VNAs measure both the magnitude and phase of the response of a network to stimuli. The measurements are made of both the reflection of the signal looking into a port and the transmission of signal through that port.

A VNA can be of any arbitrary number of ports. Common types of VNA architecture are a two-port, four-port, and a special case of VNA that is used for the radar of this thesis and called a Transmit-Reflect (T/R) VNA. The T/R VNA is essentially a 1.5 port VNA with only one port with independent stimulus signals but two physical ports each with a receiver mixed by the common referenced local oscillator to allow measurement of three parameters. The T/R can also be thought of as a full two-port VNA with the special

condition that the port two stimulus is always set to zero.

A single VNA port consists of a reference stage, a test set which separates the transmitted wave and the reflected wave; a measurement and reference receiver; analog to digital conversion stage; and a processing stage. The reference stage is responsible for stable generation of the stimulus signal that excites the linear circuit network, called the Device Under Test (DUT) — in this case, the series combination of transmit antenna, ice sheet, and receive antenna. The test set is formed by a VSWR bridge or a directional coupler, which is used to separate or determine the separate components of the transmitted and reflected signals. The receiver and conversion stage converts the reference signal, the reflected signal, and any received signal to digital data. Processing is then used to perform any calibration and provide the calculated resultant DUT network parameters from the test.

### 3.1 Scattering Parameters and the Device Under Test (DUT)

In the general case, the VNA is used to measure the reflection and transmission coefficients of a DUT. For a one-port DUT, there is an incident wave  $a$  that is generated by the VNA and supplied to the DUT and a reflected wave  $b$  returning to the VNA. *Figure 5* shows the one-port case measuring a DUT.

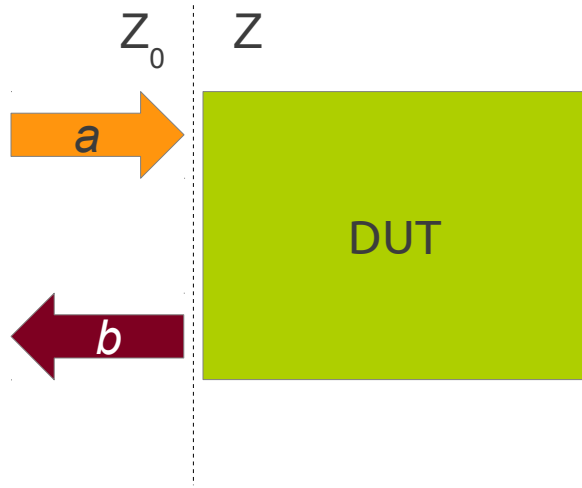


*Figure 5: One-Port Network as viewed from VNA*

Wave quantities  $a$  and  $b$  in this example have units of  $\text{W}^{-1/2}$  the power incident to the device is given by  $|a|^2$  and the power in watts reflected from the device is  $|b|^2$ . For a one-port DUT, the incident and reflected waves are related by the reflection coefficient which is defined by

$$\Gamma = \frac{b}{a} \quad (3.1)$$

If the normalized complex characteristic impedance  $z$  is defined by

$$z = \frac{Z}{Z_0} \quad (3.2)$$

from the characteristic impedance of the system  $Z$  and the arbitrary reference impedance  $Z_0$  in Equation (3.1) then can be then can be rewritten as

$$\Gamma = \frac{z-1}{z+1} \quad (3.3)$$

This means that the ratio of reflected power to transmitted power can be completely determined by the

relationship between the complex impedance of the DUT and the system reference impedance for a one-port system.

When this concept is extended to a two-port DUT, as is typical for the majority of VNA measurements and is also true for the radar that is the topic of this thesis, a scattering parameter (S-parameter) matrix is a more effective way to describe the response of the DUT to stimulus from the VNA. *Figure 6* shows the typical two-port DUT. In the case of this thesis, a T/R VNA will be used and there will be no stimulus at port two.

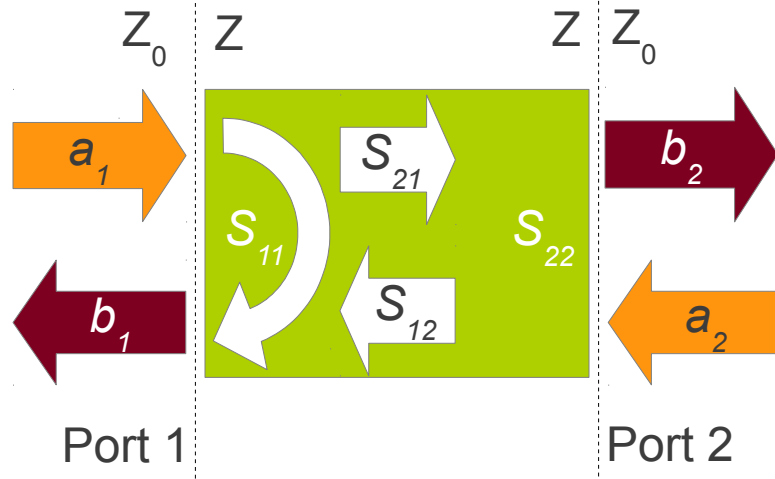


*Figure 6: Two Port Network as seen from the VNA*

A complete set of scattering parameter measurements is made by setting the incident waves at Port 1 and then port two to zero and observing the system responses in each case due to a stimulus at one port only. In the case of the VNA radar system, there will be no stimulus at Port 2. The subscripts of the S-parameters denote the port at which the response is observed,  $i$  and the port at which the stimulus is presented,  $j$ , in the form  $S_{ij}$ . This gives

$$S_{11} = \frac{b_1}{a_1} \Big|_{a_2=0} \quad (3.4)$$

and

$$S_{21} = \frac{b_2}{a_1} \Big|_{a_2=0} \quad (3.5)$$

And, similarly, by considering there to be a perfect match at port one ( $\Gamma_1 = 0$ ) and no incident stimulus ( $a_1 = 0$ ) the reverse terms can be obtained as

$$S_{22} = \frac{b_2}{a_2} \Big|_{a_1=0} \quad (3.6)$$

and

$$S_{12} = \frac{b_1}{a_2} \Big|_{a_1=0} \quad (3.7)$$

Any combination of reflection coefficients and stimuli at the two port interfaces is then just a superposition of these terms.

From these equations, expressions for the expected waves traveling into the VNA at Ports can be found as a function of the stimulus and the scattering parameters of the DUT — in this case, the ice sheet. These expressions are given as

$$b_1 = S_{11} a_1 + S_{12} a_2 \quad (3.8)$$

and

$$b_2 = S_{21} a_1 + S_{22} a_2 \quad (3.9)$$

When he calibration terms are introduced later in this document, it becomes more convenient to think of these quantities in matrix form which can be obtained by inspection of Equations (3.8) and (3.9). The matrix form is given by

$$\begin{bmatrix} b_1 \\ b_2 \end{bmatrix} = \begin{bmatrix} S_{11} & S_{12} \\ S_{21} & S_{22} \end{bmatrix} \begin{bmatrix} a_1 \\ a_2 \end{bmatrix} \quad (3.10)$$

This can be extended to a 3x3 matrix or a 4x4 matrix for three-port and four-port VNAs, respectively. For analysis of the directional element, it will be modeled as a three-port network in Section 3.5: *Test Set and Directional Circuitry*.

## 3.2 VNA Measurements, Modes, and Figures of Merit

While a VNA can be of an arbitrary number of ports and employ differing circuit topologies to achieve the performance of its measurements, all VNAs essentially measure the same quantities and use post-processing to display the measurement results in a number of different ways. All VNAs essentially measure the transmitted signal being generated and supplied by the VNA as the stimulus to the DUT — the reference signal — the reflected signal returning to the VNA from the DUT, and the received signal that is transmitted through the DUT to another port of the VNA.

While observing a commercial VNA, it may appear as if this happens across all frequencies simultaneously in a continuous sweep, but in reality those data are constructed from a series of measurement points taken at discrete frequencies. The measurements of transmission and reflection are made at a single frequency, allowing the DUT response to settle at the frequency point of interest. The VNA measures the the output stimulus signal as a reference point for the output level being generated

and then measures the reflected and received signal, magnitude, and phase, at a single frequency point. The frequency stimulus is then stepped to the next frequency of the sweep and the measurement is repeated. Data from all frequency points are then stitched together in post processing to enable measurement of many parameters.

#### Typical VNA Measurements Derived for Magnitude & Phase Data

- All S-Parameters
- Input and Output Impedance
- Reflection Coefficient
- Transmission Coefficient
- Return Loss
- Voltage Standing Wave Ratio (VSWR)
- Group Delay
- Phase Delay
- Stability
- Feed-through
- Isolation
- Conversion Loss

There are several key performance figures for the VNA. These include, in qualitative terms, the number

of ports, power level, input power range, frequency range, the timing accuracy, the amplitude accuracy and resolution, and stability over time. Some parameters, like the number of ports of the VNA, have been addressed already. For this application, a T/R VNA is all that is required.

The output power range for the VNA simply specifies the minimum output, maximum output, and the step size of power level available for the stimulus signal provided by the VNA to the DUT. For the case of this radar, only a single output level is required since the system designer is in control of the system and is able to determine the output power level required to ensure a measurable return signal from the ice sheet discontinuities. In future, more complex systems that seek to also probe surface phenomena, output power control may be advantageous. Power levels in VNA are almost always specified in literature in units of dBm by convention.

The input power level is typically specified to correspond directly to the maximum output power level of the VNA stimulus although some systems will tolerate more received power on the inputs (port receiving a transmission measurement) than can be supplied by the stimulus for applications such as measurement of amplifiers. This is not necessary for the radar application of this thesis.

Frequency range simply specifies the minimum and maximum frequencies that limit the VNA. The implementation of the internal circuitry inside the VNA and fabrication technique limits its frequency range. For the purpose of the radar that is the subject of this thesis, a frequency sweep of 50 MHz to 500 MHz is sufficient. It should be noted, however, that the upper frequency range of the VNA sets the point at which the frequency domain reflection data truncates and therefore limits the time-resolution — equivalent to spacial resolution assuming a known propagation velocity — to which discontinuities in the material properties within the propagation path can be unambiguously resolved by time domain transformation of the frequency data alone.

The timing accuracy, an umbrella term for a number of parameters, has serious implications for the performance of the VNA as the radar system that is the subject of this thesis. The timing accuracy encompasses the initial accuracy of the reference oscillator that drives all measurements, its phase noise, its susceptibility to coupled EMI, its noise figure, its drift with time, and its drift with temperature. These imperfections of the base reference oscillator then flow to the stimulus via a path through the clock fanout buffer circuitry, Voltage-Controlled Oscillators (VCOs), and Local Oscillators (LOs), which are mixed with the measurement signals in the receiver stages. This results in phase or frequency errors of the Intermediate Frequency (IF), which are measured by the sampling circuitry in the VNA.

The response magnitude accuracy and the resolution, while critical in many applications, are less critical for this radar. This is because a meticulous three-point or enhanced-response calibration can remove many magnitude errors and the absolute reflection coefficient magnitude measurement has no direct impact on thickness measurements assuming that the return from the internal discontinuities within the ice sheet is sufficiently strong to be discernible in the time domain transformation of the return. The dynamic range of the receiver and the directivity of the directional element do have implications on the tolerable amount of path loss in the radar and on the minimum discontinuities in the glacial ice that can be determined.

### 3.3 VNA System Block Diagram

*Figure 7* shows the general architectural layout of a typical single channel VNA system. The major system blocks include the directional element, shown as a VSWR bridge, the power splitter, the RF generator source, the Local Oscillator generator source, the measurement receiver, the reference receiver, and the digitization and processing circuitry. Some subsystems and components like input protection, baluns, biasing, etc. are not shown for the purposes of simplicity. The sections of the VNA are discussed in more detail in the following sections and expressions for performance metrics and analyses of the non-

idea properties are presented.

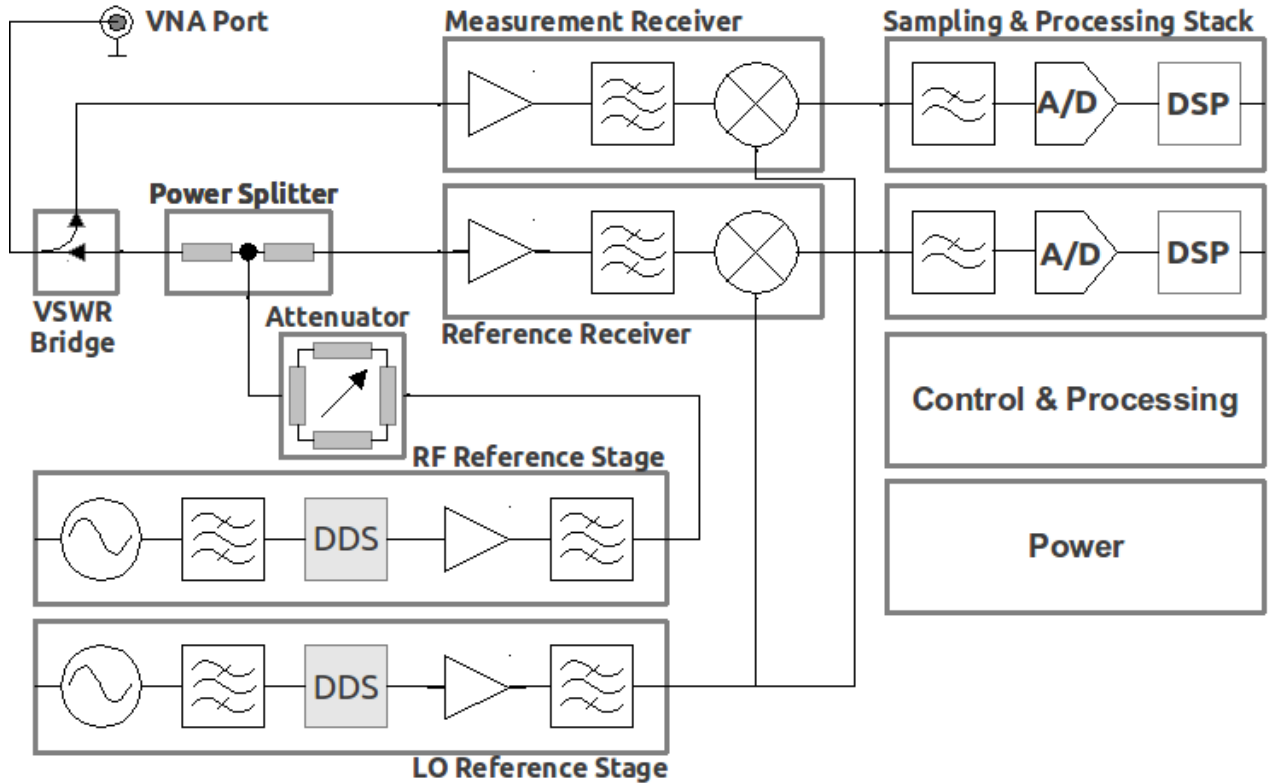


Figure 7: Simplified VNA single channel block diagram

### 3.4 Input Protection Circuitry

Input protection circuitry is generally required for all test instruments but care is used in the design such that any input protection circuitry does not interfere with the operation of the measurements or affect the input and output impedances of the system ports. Loading effects on the system impedance can usually be compensated for by careful design of the directional element to include the loading as well as by using a three-point calibration method (Open-Short-Load) [Baier, 2009] or the enhanced-response calibration. Input protection is typically required to prevent possible damage to the system discussed in this thesis from three primary sources: overloading of signal at the input resulting from normal operation of the

VNA, damaging common-mode voltage between system devices, and ElectroStatic Discharge (ESD) into the electronics from personnel and equipment contact with the system ports.

Because the design of the system is totally within the control of the author, because a VNA provides its own stimulus, and by observing standard design principals for a VNA, the input to the receiving port cannot realistically exceed the design limitation. This is due to the fact that the VNA is designed to tolerate a dead-short from the stimulus port to the receiving port. In any practical application, the receiving port will always experience a lower level input signal than the stimulus.

AC coupling at the input ports is typically implemented with the VNA by use of large-value, high-voltage tolerant DC blocking caps, possibly integrated with the receiver bias tee. If appropriate AC coupling is used into the VNA and appropriate design steps are taken with isolation of the digital interface to processing host PC, common-mode voltages are not likely to present problems. In the case of a VNA that is directly powered from the processing PC, the VNA circuitry is also powered by the USB supply and shares a common ground point with the PC. This leaves only the ESD problem presented at the terminals of the sensitive VNA electronics.

Typical input protection requirements for test equipment are the ability to withstand static discharge on the input ports at or above the HBM 4-kV Level 2 [Diep, 2001]. This is particularly true since the gear required for cold weather expeditions is typically subject to significant static buildup in the arid polar climates. The antennas and cabling are passive devices within the system and require no additional special protections from general static buildup.

Practical circuits for implementation of input protection on an RF system in this frequency range without loading of the VNA port input impedance — particularly capacitive loading effect — are the use of Gas Discharge Tubes (GDTs) for high voltage arc over connections from the antenna; a high inductance, high

resistance choke to bleed any static energy from the antenna [ADI, 2000]; and transient voltage suppression by means of either resonant L-C sections without or Silicon-Germanium transorb diodes that are designed for RF frequencies [Hyvoven, 2005]. Since the system of this thesis only need to function to a few hundred megahertz and not several gigahertz as is common of many COTS VNAs, the tasks of selecting appropriately high-speed TVS diodes is greatly simplified.

The modeling of static discharge events is commonly done using the standard Human Body Model (HBM) with test procedures specified by applicable sections of both US Mil Standards — the original standard in MIL-STD-883 — and later the joint JEDEC standard. The HBM method of analyzing, protecting against, and testing for static discharge models the source of charge as 100-pF capacitor and 1500-ohm series resistance. The standard then specifies the voltage on the capacitor and the rise time of the discharge. In industry, 2-kV and 5-kV usage of the standard is quite common.

In consideration of the above concerns about the environment and use-case of the system making it susceptible to large discharges, standard industry practice [Diep, 2001] is to recommended that the test ports exposed to the user be compliant with MIL-STD-883, Method 3015.8, Electrostatic Discharge Sensitivity Classification and the JDEC JS-001 standard [JEDEC, 2011] for 5.1 kV HBM.

### 3.5 Test Set and Directional Circuitry

The test set is the portion of the VNA that is used to measure the reflection coefficient,  $\Gamma_x$  where  $x$  is the port of the DUT, whether  $S_{11}$ ,  $S_{22}$ , etc. depending on the number of ports. The test set separates the outgoing reference signal from the reference section, the reflected signal from the DUT when the port is transmitting, and the received signal when the port is receiving. The directional element is, conceptually, a three-port device that separates the wave incident to the DUT and reflected from the DUT. In practice, the directional element is typically implemented as a four-port device with an additional

isolation port or with the power dividing circuitry to provide the reference channel to the receiver as the fourth port. *Figure 8* shows the function of the directional element of the test set in the conceptual three-port form, assuming that the reference signal has been divided off from the oscillator reference section externally using an appropriate resistive power splitter tee [Pozar, 2005], 6-dB resistive bridge hybrid [Bryant, 1993], or Wilkinson power divider [Wilkinson, 1960].

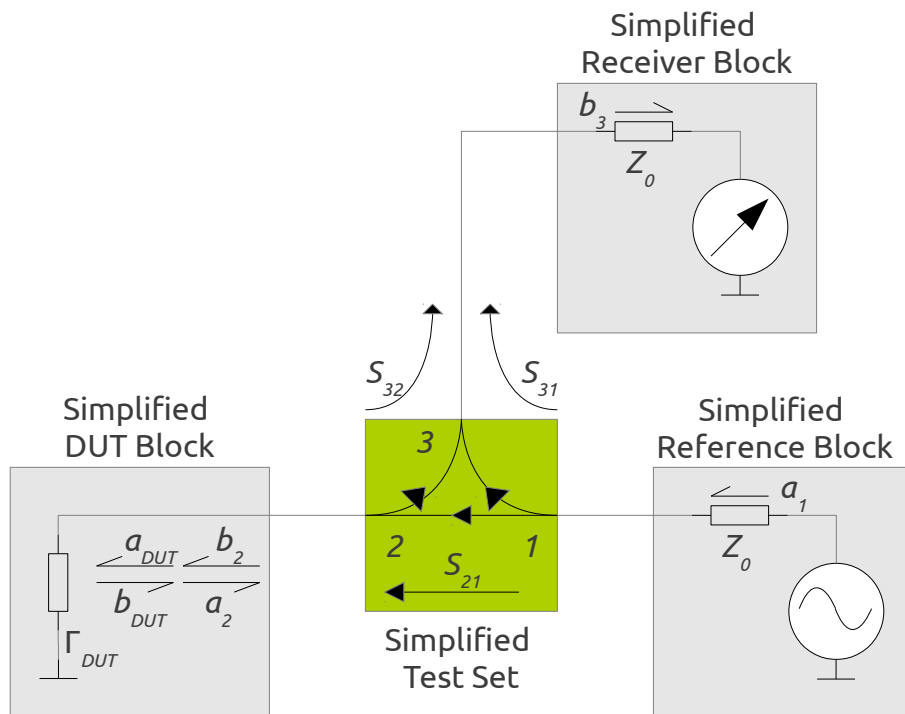


*Figure 8: Test Set represented as a three-port network to the VNA system*

The conceptual reference generator produces a output signal  $a_1$ , which is supplied to the test set by its port one. That signal passes through the test set with some forward transmission coefficient  $S_{21}$ . In practice,  $S_{21}$  will always be less than 1 since some portion is sampled as the reference signal and the directional element is neither perfectly directional nor lossless and the impedances of the reference oscillator and the

test set are never perfectly matched.

The signal traveling from the DUT to the measurement receiver is transmitted with a transmission coefficient of  $S_{32}$ . In practice, the transmission coefficient of the signal traveling back to the directional element from the DUT will always be less than one as well since the directional element is not perfectly directional nor is it lossless.

Using standard network theory convention, it can be observed that the signal from the DUT,  $b_{DUT}$ , to the test set is simply the product of the signal into the DUT,  $a_{DUT}$ , and the reflection coefficient of the DUT when the DUT contains no independent stimulus. This is given by

$$b_{DUT} = \Gamma_{DUT} a_{DUT} \quad (3.11)$$

and

$$a_2 = \Gamma_{DUT} b_2 \quad (3.12)$$

Ideally the ratio of the signal present at port three to the signal present at port 1 would represent the reflection coefficient of the DUT if the directional element were perfectly directional and lossless. In practice, the measurement result at the receiver including the non-ideal bridge characteristics,  $M_{Ref}$ , will be this true reflection coefficient multiplied by the imperfect transmission coefficients of the theoretical three-port directional element. This product of  $S_{32}$  and  $S_{21}$  is called the *Reflection Tracking* or  $R_{track}$  of the VNA and is one of the standard figures of merit of VNA design performance. Some texts will refer to reflection tracking as simply  $R$  or  $R_t$ . The non-ideal nature of  $R_{track}$  affects the measurement accuracy of the VNA since any measured impedance will scale with the magnitude of  $R_{track}$  and be rotated in phase angle by the phase of  $R_{track}$ . Fortunately, as will be shown later in this thesis, a three-point calibration can effectively remove the reflection tracking error. The received signal at the measurement receiver is then

$$M = \frac{b_3}{a_1} \quad (3.13)$$

and the reflected portion of the signal then becomes

$$M_{Refl} = \Gamma_{DUT} \cdot R_{track} \quad (3.14)$$

with the real tracking error reducing to

$$R_{track} = S_{32} \cdot S_{21} \quad (3.15)$$

Another non-ideal characteristic associated with this model of the directional element is the assumption that the directional element is perfectly directional (i. e. assuming  $S_{31} = 0$ ). This is not a valid assumption. In reality, there will be *crosstalk* from the reference oscillator directly to the measurement receiver, bypassing the DUT. This crosstalk manifests as  $S_{31}$  and will be a complex quantity. The quantity *Directivity* of the element,  $D$ , is a ratio of  $S_{31}$  and  $R_{track}$  given by the received component

$$M_{dir} = S_{31} + R_{track} \cdot \Gamma_{DUT} \quad (3.16)$$

with the directivity then reducing to

$$D = \frac{S_{31}}{R_{track}} \quad (3.17)$$

The important implication of directivity is that a VNA cannot measure reflection coefficients smaller than the directivity of its directional element (e.g. VSWR bridge). Directivity error can be reduced by calibration but the true reflection coefficient of the DUT must be less than the effective value of directivity of the directional element. For extremely small reflection coefficients, other techniques must be used such as estimating reflection from the transmission coefficient.

Until now, the analysis has assumed that the ports of the directional element are all perfectly matched. For port 1 and port 3, this may be a valid assumption since there is typically good isolation in the directional element and the source impedance of the oscillator and the input impedance of the measurement receiver are within the control of the design. For port 2, however, connected to the DUT, there can be large mismatches leading to large reflection coefficients.

Consider that the DUT may be of arbitrary impedance. Even if the output impedance of the directional element is designed so as to be perfectly matched to the nominal system impedance, connection of a very low or very high impedance DUT will still cause reflections to arise between the DUT and the directional element.

The reflection coefficient  $S_{22}$  limits the the ability of the VNA to measure large reflection coefficients. This is intuitive since large reflection coefficients will lead to a larger  $S_{22}$  and a dominance of this term. Finally, with these three main sources of error accounted for, the result  $M$  becomes that given by

$$M = R_{track} \left( D + \frac{\Gamma_{DUT}}{1 - S_{22} \cdot \Gamma_{DUT}} \right) \quad (3.18)$$

For lower frequency VNA, those below about 1–2 GHz, implementation of the directional element of the test set as a microwave directional coupler is difficult due the physical dimensions — the couplers are specific fractions of wavelengths — and material constraints on the fabrication of such a device [Pozar, 2005]. Because of this, in lower-frequency VNAs, the test set directional element is typically implemented as a VSWR bridge. In commercial VNAs that span kilohertz to many gigahertz, a combination of VSWR bridge and directional coupler is used, switched in a manner transparent to the end user. Since the topic of this thesis is confined to frequencies of 50 to 500 MHz, and the first few harmonics thereof, a VSWR bridge alone is sufficient to the design.

### 3.5.1 VSWR Bridge

A VSWR bridge, in the most simplistic sense, functions much like a balanced Wheatstone bridge in which, when a matched impedance is presented at the DUT terminals, the voltage across the two nodes of the bridge will be zero. When the impedance of the DUT does not track the reference impedance of the system, a voltage proportional to the difference in impedance will be detected across the bridge. *Figure 9* shows the classic bridge design.

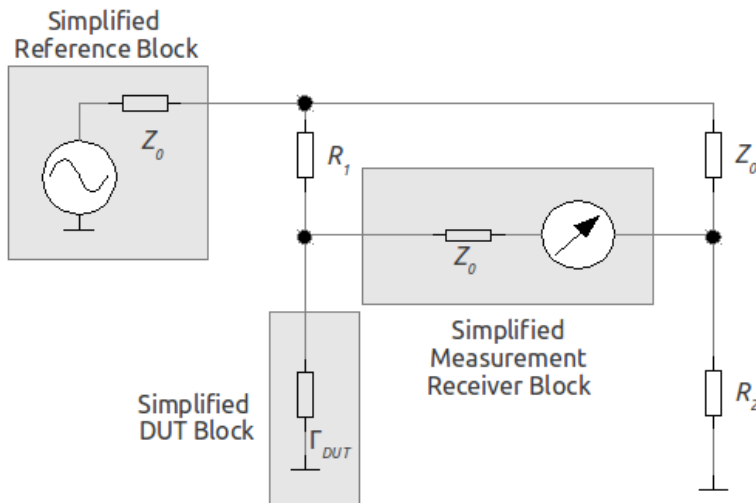


Figure 9: Standard VSWR bridge block diagram

In almost all RF VNA designs, the nominal system impedance,  $Z_0$ , is 50 ohms. This is the case with the radar system and VNA of this thesis. The output impedance of the generator section is designed such that it is equal to the nominal system impedance as is the input impedance of the receiver circuitry section.

The bridge is comprised conceptually of the two resistances,  $R_1$  and  $R_2$ . Using simple circuit theory,  $S_{22}$  looking into the bridge at the DUT terminals,  $S_{22}$  is given by

$$S_{22} = \frac{R_1 R_2 - Z_0^2}{2(R_1 + Z_0)(R_2 + Z_0)} \quad (3.19)$$

To give matched conditions, it can easily be shown that the product of  $R_1$  and  $R_2$  should be set to the square of the system characteristic impedance.

$$R_1 R_2 = Z_0^2 \quad (3.20)$$

For convenience,  $R_1$  is usually chosen equal to  $R_2$ .

Given these choices and returning to the simple circuit theory, the transmission coefficients for the bridge are calculated to be, for forward transmission through the bridge

$$S_{21} = \frac{Z_0}{Z_0 + R_2} \quad (3.21)$$

and, for reflection transmission to the measurement receiver

$$S_{32} = \frac{R_2}{Z_0 + R_2} \quad (3.22)$$

and for isolation

$$S_{31} = 0 \quad (3.23)$$

Substituting these into Equation (3.15) gives the reflection tracking for this configuration of VSWR bridge

$$R_{track} = S_{32} \cdot S_{21} = \left( \frac{Z_0}{Z_0 + R_2} \right) \left( \frac{R_2}{Z_0 + R_2} \right) = \frac{1}{4} \approx 12 dB \quad (3.24)$$

Which simplifies to 12-dB.

### 3.5.2 RF Directional Coupler

As was discussed in Section 3.5: *Test Set and Directional Circuitry*, the directional coupler fabricated with microstrip is not particularly well suited for a VNA in this frequency range. A directional coupler is typically implemented as a 90-degree-long section of closely-coupled coplanar microstrip with impedances set to excite specific TM modes within the strip resulting in coupling in the reverse direction and isolation in the forward direction in the coupled line [Pozar, 2005]. Because the line section must be 90 degrees electrical length within its frequency band, neglecting the stepped and tapered strip required to provide broadband response [Bryant, 1993], still necessitates microstrip segments on the order or 10s of centimeters for performance in VHF and UHF bands. This is why the use of directional couplers below 1–2 GHz is not ideal. Design guidelines for directional couplers can be found in [Gupta, 1996], [Pozar, 2005], [Bryant, 1993] as well as other common RF and microwave design texts should one wish to implement one.

## 3.6 Step Attenuators and Signal Level Control

Most VNA systems include fixed or switched step attenuators on the generator set as well as the receiver set to facilitate operation over a larger dynamic range of power levels. They are used to attenuate the received signal when active components are placed in the DUT path resulting in received power greater than the stimulus supplied by the reference generator.

For step attenuators in the receive path, the VNA reference plane can be extended to include the attenuator as part of the test test and modified values for the reflection tracking, match, and directivity can be calculated. If the attenuator is a two-port network with the usual S-parameters and is a reciprocal

passive network — almost always the case — then  $S_{12\text{att}}$  will equal  $S_{21\text{att}}$  and the expressions for reflection tracking, match, and directivity can be calculated as

$$S_{21\text{att}} = S_{12\text{att}} \quad (3.25)$$

and

$$R_{\text{trackatt}} \approx S_{21\text{att}}^2 \quad (3.26)$$

and

$$S_{\text{att}} \approx S_{11\text{att}} \quad (3.27)$$

Note that, while the attenuator always degrades the directivity of the test set it will almost always improve the impedance match since a passive attenuator can be physically-fabricated with exacting balanced, broadband impedance-matched characteristics quite easily [Pozar, 2005]. The directivity with attenuation is given by

$$D_{\text{att}} \approx \frac{D + S_{22\text{att}}}{S_{21\text{att}}} \quad (3.28)$$

Generator step attenuators are also typically included in the generator path between the reference generator PLL and the power splitter prior to the test set to allow the selection of lower power levels should the DUT be unable to tolerate input signals at the VNA's full output. For an application such as the work of this thesis, step attenuators are unnecessary in the signal chain because the designer of the VNA is in total control of the system design and can select a constant output power level suitable for the measurements. Because generator step attenuators are included after the oscillator circuitry but before the test set, no additional adjustments are needed to the reflection tracking, match, and directivity terms.

If power level control is desired to permit probing of shallow features without saturating receivers or to permit the probing of widely varying depths with minimal power consumption during a sweep, the amplifier in the generator signal chain can be a digitally controlled variable gain type. Attenuators are typically used due to frequency response but at sub-gigahertz frequencies, variable gain amplifiers are appropriate.

### 3.7 Core Reference Oscillator

The reference oscillator section provides the clock reference for the entire VNA, drives the RF source that is used to excite the output wave stimulus, and provides the local oscillator reference for the mixers in the receivers. Almost all VNA architectures use a single, high-precision reference oscillator as the basis for clock generation and then generate the various reference clocks from that single source using Phase-Locked-Loops (PLL) and clock distribution integrated circuits — typically called clock fanout buffers — rather than using separate oscillators for the RF output and LO functions. This is done because the cost of multiple stabilized references is high and the circuitry required to synchronize the references using multiple independent PLLs is very difficult to implement without introducing further phase errors into the signal chain [HP, 1997].

There are several types of reference oscillators currently used in production test equipment. The published hobbyist VNA concept that is the starting point of this thesis [Baier, 2009] uses simple quartz crystal in a classic Pierce oscillator configuration [Pierce, 1923] without temperature compensation to provide a reference. There are alternative oscillator options as explored in [Corr, 2002].

While the simplest oscillator is a tuned LC tank circuit, which is resonant at a particular frequency, it is relatively inaccurate. LC resonant oscillators are easy to fabricate and very inexpensive, but their performance is not sufficient for test and measurement applications. The primary shortcomings of LC

oscillators are found both in initial accuracy and long-term stability. The initial accuracy of an LC tank is determined by the tolerance of the inductor and capacitor, the component quality factor (' $Q$ '), and layout considerations since a frequent source of error and instability is the parasitic magnetic field created by the inductor even when components of the highest tolerance are used [Mazzanti, 2006]. The aging of the capacitor, in particular, causes significant long-term stability problems as even the most reliable RF capacitors — Teflon based — are subject to significant and unpredictable drift with aging [Pease, 1991]. Typically, all capacitors lose capacitance as they age due to deterioration of the dielectric.

The best oscillators are ones that are based on piezoelectric response of crystals, typically quartz, since the degree of physical manufacturing precision required to achieve the same initial accuracy as other techniques is much more practical when compared to processes that rely on dielectric properties or lumped circuit element values of wound or microstrip inductors [Vig, 2004]. Crystal piezoelectric oscillators are also far less subject to coupled EMI from outside source [Koleshov, 2005].

The basic building block of the crystal oscillator is a quartz crystal of specific dimensions that exhibits a piezoelectric response when a voltage is applied to it. The response of the crystal has a significant temperature dependence [Salzenstein, 2010]. The frequency stability of the oscillator is determined by the crystal's loaded quality factor ( $Q_L$ ).  $Q_L$  is inversely dependent on the frequency of oscillation and is dependent on the particular cut of the crystal itself [Vernotte, 1999]. The temperature sensitivity depends primarily on the cut orientation in the crystal lattice of the quartz. The temperature compensated cuts are chosen as to minimize frequency and temperature dependencies [Vernotte, 1999]. Because of this, crystals are often packaged in a metal can — shielding, both electromagnetic and thermal — with varactor diode tuning circuitry with a temperature coefficient proportional to the temperature coefficient of the crystal itself. The varactor's temperature coefficient compensates for the variation of resonant frequency with temperature. This configuration is the temperature-compensated crystal oscillator (TCXO).

Further improvement is made by packaging a TCXO in a package with significant thermal mass and heating the package with a thermostatically-controlled heating element to maintain constant temperature of the oscillator. This arrangement is the Oven-Compensated Crystal Oscillator (OCXO).

While an OCXO offers the best stability of any crystal oscillator, its power consumption, cost, and physical size make it impractical for a low-cost instrument which is the topic of this thesis. For this reason, design choices have been restricted to TCXO-based references.

### 3.8 Frequency Sweep Generation

There are several clocks references that are required for the operation of the VNA. All of these are typically generated from the common clock such that the phase reference of all sources is common — a requirement if quadrature phase detection is used for direct recovery of the real and imaginary components of the response. This should not be confused with distinguishing between whether the RF stimulus and the LO for receiver tuning are referenced to the same clock.

There are different configurations for the RF generation within the VNA: the homodyne and the heterodyne. In a homodyne configuration, the stimulus signal and the Local Oscillator (LO) signal for the receiver recovery are generated from the same clock. In a heterodyne arrangement, different clocks are used to drive the reference stimulus to the DUT and to provide the LO source to the tuned receiver mixers. Use of a different LO allows the mixing of the IF to an arbitrary band more suitable to the sampling circuitry. Use of homodyne would necessitate mixing the RF input to an IF at DC if the lower band is taken. Mixing to DC is undesirable for a number of reasons including the DC accuracy of sampling circuitry and frequency response of biasing circuitry.

The signal chain for generation of the sweep of stimulus and receiver recovery signals begins with the

base reference oscillator. The high stability oscillator then feeds a divider or fanout buffer, depending on implementation, which provides the buffered signal to downstream components such as the digital hardware, the RF sources for stimulus, and the local oscillators for the receivers. The output of the splitter or fanout typically drives digital electronics directly since most microprocessors have internal Phase-Locked-Loops (PLLs) that generate their core clock frequencies. The RF and LO signals are typically generated by a combination of PLL and DDS circuitry downstream. The typical distribution architecture is shown in *Figure 10*.

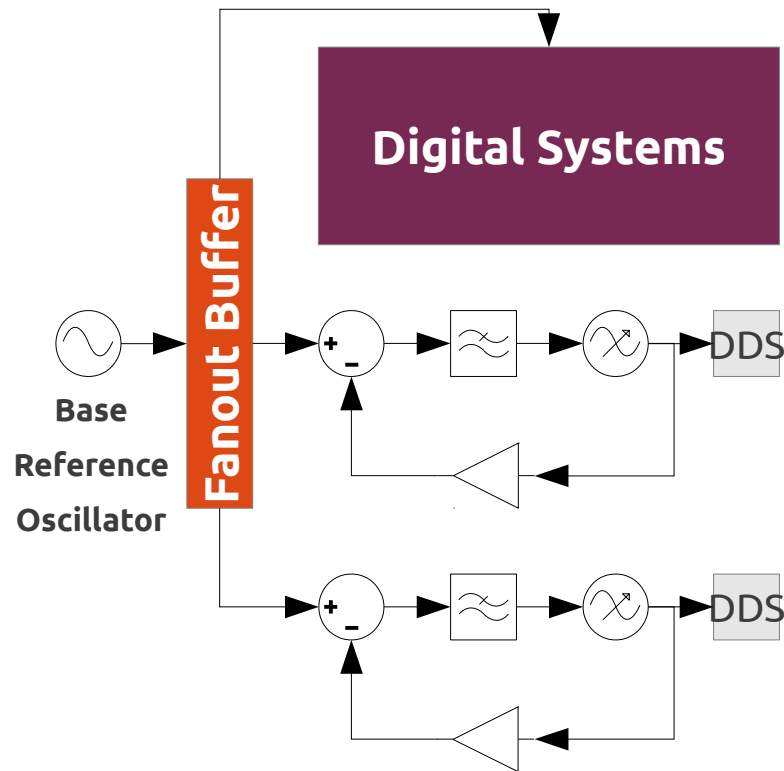


*Figure 10: Clock distribution architecture in typical VNA*

### 3.9 Phase-Locked-Loops (PLLs)

The PLL takes the base reference oscillator signal and generates from it the signals for use as the RF generator output — the stimulus — and any LO signals required for the receivers. A PLL uses the base reference oscillator, a phase-frequency detector, a feedback loop, and a Voltage-Controlled Oscillator (VCO) to generate the the output. Some VNA designs use fixed-frequency multipliers and digital synthesis — a DDS — to generate the RF and LO signals instead of a true PLL. This will be the case of the published design that serves as the basis for this thesis [Baier, 2009c].

The PLL locks the output clock phase to the input clock phase using feedback from the phase-frequency detector. In a settled, steady-state condition, the output of the phase–frequency detector is 0 and the PLL is locked. A PLL is shown schematically in *Figure 11*.

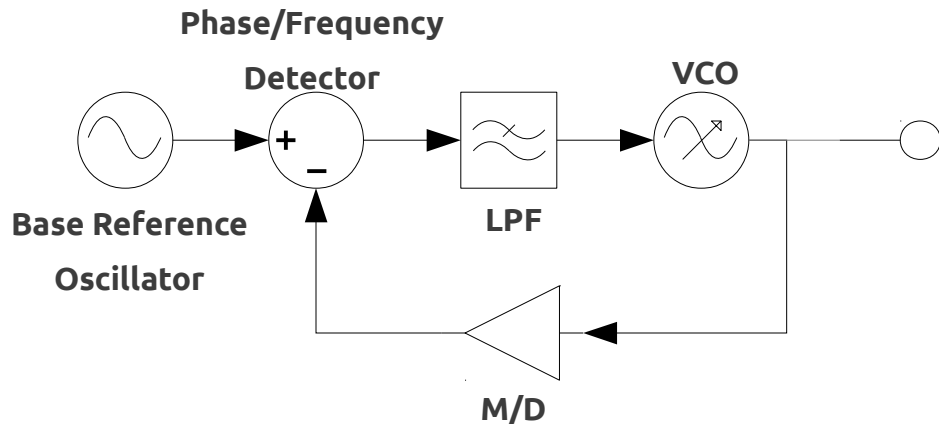


*Figure 11: Simplified PLL Topology*

Beyond its principal function of simply generating the required signals from the base reference oscillator, a carefully designed PLL can attenuate phase-noise and clock jitter of the base reference oscillator by

low-pass filtering the loop-gain of the PLL and by low-pass filtering the phase-frequency detector output signal . The low-pass filtering of the loop-gain is, by convention, taken as part of the M/D divider ratio transfer function where as the low-pass filtering of the phase-frequency detector output is taken as a discrete system filter block. Several commercial PLL control integrated circuits include this functionality.

One key measure of the performance of PLL or clock multipliers in the VNA configuration is that of the jitter transfer of the PLL. Jitter transfer is the amount of jitter or phase noise transferred from input clock — the base reference oscillator — to output clock. A jitter transfer function  $H_{jitter}(f)$  can be calculated, which shows the amount of jitter transferred through the PLL loop to the output clocks that feed the RF stimulus and the local oscillators for signal recovery in the reference, transmission, and reflection receivers.

Another PLL design metric as it relates to phase/jitter accuracy is the internal PLL generation. PLL jitter generation is the amount of jitter or phase noise that is internally generated by the PLL loop irrespective of the input jitter — input jitter set to zero — from the base reference oscillator. Phase noise or jitter internally generated by the PLL is typically a product of thermal noise processes within the VCO itself rather than a function of the loop or phase-frequency detector.

While the use of the phase-frequency detector filter and loop transfer function to attenuate phase noise of the base reference oscillator is a useful way to reduce the system phase noise, the filters cannot be made with arbitrarily low cutoffs and still maintain the response stability of the system. Jitter tolerance is the amount of jitter input that the PLL loop bandwidth is able to tolerate before the PLL becomes unstable and falls out of lock.

## 3.10 Receiver Sets

The receivers in a VNA can be implemented as either a narrowband receiver that is tuned to a specific bandwidth surrounding the stimulus frequency or a broadband receiver that is not tuned to the stimulus frequency. Almost all swept VNAs use tuned receivers that provide better dynamic range and better SNR in the measurement frequency because the narrow passband of the receiver restricts the broadband noise that is downconverted and sampled by the analog to digital conversion system. In this context, this means both thermal Johnson noise and EMI are coupled into the instrument.

The receiver sets in the VNA are implemented as either homodyne or heterodyne. As discussed in the previous section, almost all modern VNA systems use heterodyne type receivers in which the RF stimulus source and thus the RF received as a transmission or reflection are provided by one oscillator and the downconversion to an Intermediate Frequency (IF) is done by mixing with an LO that is different in frequency than the RF frequency. This allows greater system flexibility the two oscillators must be synchronized. If the RF signal were to be demodulated by mixing with the RF, the resultant (lower sideband) IF would be at 0 Hz and difficult to process. For convenience of circuit design, an IF on the order of audio frequencies are usually chosen to allow the use of fast A/Ds, high-precision amplifiers, and filters of reasonable size. Alternatively, some new VNAs use direct digital downconversion and bandpass (sub-Nyquist) sampling.

### 3.10.1 Quadrature Phase Detection

Some new VNA systems with advanced hardware use Direct Digital Synthesis (DDS), a form of a Numerically-Controlled Oscillator (NCO) to mix the IF down to 0 Hz — DC — after the analog operations on the IF. Once at DC, the signal can then be split using quadrature phase detection to

accurately separate the magnitude and phase components of the received signals. The magnitude and phase outputs of the quadrature detector are then sampled by a high-precision, low-speed A/D converter and processed to provide the S-parameter data. This implies a requirement for a high precision A/D converter with true DC accuracy.

The quadrature detection procedure works by first downconverting to a fixed an IF, which for the purposes of understanding the quadrature detection can be of any arbitrary value. The digitally controlled DDS is then set to provide a further low which frequency-shifts the IF to DC. The signals are given by

$$u_{IF}(t) = A_{IF} \cdot \cos(2\pi f_{IF} t + \varphi_{IF}) \quad (3.29)$$

and

$$u_{NCO}(t) = A_{NCO} \cdot \cos(2\pi f_{NCO} t) \quad (3.30)$$

with  $A_{IF}$  and  $A_{NCO}$  giving the in-phase magnitudes — the real component — and the quadrature magnitudes — the imaginary component. Phase offset is given by  $\varphi_{IF}$ .

It is then assumed that  $f_{IF}$  is equal to  $f_{NCO}$  and that the phase shift is 90 degrees, giving

$$f_{IF} = f_{NCO} \quad (3.31)$$

and thus

$$u_{\Re}(t) = \frac{1}{2} A_{IF} \cdot A_{NCO} [\cos(\varphi_{IF}) + \cos(4\pi f_{NCO} t + \varphi_{IF})] \quad (3.32)$$

and

$$u_{\Im}(t) = \frac{1}{2} A_{IF} \cdot A_{NCO} [\sin(\varphi_{IF}) - \sin(4\pi f_{NCO} t + \varphi_{IF})] \quad (3.33)$$

### 3.11 A/D Sampling

After the signal has been downconverted to a suitable IF, typically in the audio range, the signal is sampled to provide the received amplitude and phase. The sampling is done to the reference channel as well as to the receive channel in the case of transmission measurements or to the reflect channel in the case of reflection measurements, depending on whether the measurement being made is  $S_{21}$  or  $S_{11}$ . High performance VNAs have many independent A/Ds that are able to simultaneously sample many ports and measure the transmission and reflection channels simultaneously.

Several types of A/D converters are used to accomplish this task. Popular types include the simultaneous “flash” converter, sigma-delta converter, successive approximation, and dual slope integration types. Each type of converter has advantages and disadvantages for their use in this application.

Flash converters are very fast and can sample signals of gigahertz but are limited in resolution and tend to be very inefficient from a power-usage perspective. Flash converters would be a poor choice for this application because the sweep time need not be fast for IFs in the audio range and because the measurement resolution is critical. Sigma-Delta type A/D converters, in particular, are ill-suited to precision test and measurement applications because of their inherent non-linearity problems.

Successive-Approximation (SA) type A/Ds work by successively comparing the input voltage within the internal sample-and-hold circuit of the A/D to a recursively bifurcated reference voltage using a comparator. For example, for a 0–5 V A/D, the input is compared to see if it is less than or greater than half the measurement range, 2.5 V. The next comparison then compares the input to see if it is greater than or less than 1.25 V or 3.75 V, depending on the first measurements. The successive approximation process continues until the result is reached. SA D/A converters are very accurate and can work well in a VNA; however, their conversion times tend to be slow due to the number of approximation cycles

required to achieve test and measurement quality resolutions of 16, 18, or 24 bits.

Dual-Slope-Integration (DSI) type A/D converters have high levels of DC accuracy if properly designed; however, they tend to be very, very slow. For any reasonable IF bandwidth and desired sweep speed for the VNA, a DSI type A/D is typically unsuitable. There is published work showing their use in very slow VNA systems that require high accuracy reflection and transmission magnitude measurements of (primarily resistive) networks.

The primary figures of merit for A/D system performance are the number of bits of resolution and the resulting quantization error, DC accuracy, Effective Number Of Bits (ENOB), and linearity. In addition, the A/D must be chosen to ensure that it is operating within its input limits and clocked within its frequency range.

The number of bits of resolution of the A/D sets the smallest step in voltage that the A/D can measure, assuming all else is ideal. This leads to quantization error, which is the output error resulting from the finite step size of the digital data resolution. This quantization error, in a VNA, leads to both magnitude and phase errors if direct digitization of the IF is used. Computation of the error terms for a quadrature detector is more complex but the same holds true. The theoretical maximum signal-to-quantization-noise ratio achievable by the sampling is determined by the number of bits, given as

$$SQNR \approx 6.02 \cdot Q \text{ dB} \quad (3.34)$$

For a 14 bit A/D, the SQNR and upper bound on SNR is approximately 84.2-dB, 96.3-db for a 16 bit A/D, 108.4-dB for an 18 bit A/D and 144.4-dB for a 24 bit A/D. It should be noted that in practice, 144 dB of SNR in a practical A/D is impossible to achieve. The practical limit of SNR in real A/Ds is approximately 120 dB. Because many of the non-ideal characteristics of the A/D serve to reduce the signal-to-noise ratio

obtainable in a practical A/D, the metric of ENOB is sometimes used to describe the number of bits of resolution that would be obtained by applying (3.34) to the real SNR of the system instead of the SQNR.

Linearity is another concern when dealing with A/Ds for test and measurement applications in the VNA. Linearity is a measure of how well the digital value at the output tracks the analog value at the input of the A/D. The two primary figures of merit for linearity of the A/D are the Integral Non-Linearity (INL) and the Differential Non-Linearity (DNL). INL is a measure of maximum deviation between the ideal output of an A/D and the actual output level of the A/D for a given input disregarding and constant gain functions of the A/D. DNL is a measure of deviation of outputs of the A/D between successive values, which would ideally differ by only one Least Significant Bit (LSB). DNL measurements have more significance for applications such as this VNA where phase is a critical factor.

### **3.12 Signal Chain Accuracy and Calibration**

This section addresses the various errors terms and non-ideal performance of the VNA. The causes of the various errors are discussed and methods of mitigation are discussed. Implementation of error correction and calibration for the VNA is discussed in more detail in the conclusions section of this document.

The common error sources in VNA measurements are generally found to be systematic errors, random errors, or drift errors [Agilent, 2002].

Systematic errors in VNA measurements are those that are inherent to the design of the VNA and driven by the construction of the VNA with non-ideal components and subsystems (e.g. op-amps, which exhibit finite open loop gain; directional couplers and VSWR bridges, which do not have perfect directivity; resistive loss in the interconnects, etc.). These error sources typically do not vary with time and can be removed from the measurement by a standard calibration of the VNA. The calibration is a software

process that is applied to the measured result in post processing to correct the error terms.

Random errors are those resultant from statistical physical processes like the Johnson thermal noise in components and semiconductor devices, repeatability of mechanical components and connectors, and received EMI from outside sources. These types of errors cannot be predicted and cannot be removed through calibration. Many of these random error processes, however, occur with a known probabilistic distribution (e.g., additive white Gaussian noise — AWGN) and averaging of the response of many measurements will produce a more accurate result as the averaging of an AWGN response will tend to reduce out the error term. Other techniques are also used to reduce random errors like the narrowing of the bandwidth of the system — reducing the thermal noise term — or increasing the system power level to increase the signal to noise ratio and thus drown out received EMI.

Drift errors are ones that occur after calibration [Agilent, 2002] as the system ages, changes in temperature, or changes in environmental condition (e.g., humidity affecting PCB leakage). These drift errors are regarded in some literature as being not a separate class of error terms but rather systematic error that are not constant but instead have a time or temperature dependency [Rytting, 2009].

### **3.12.1 Types of Calibrations and Error Correction**

Two types of error correction and calibration are possible. A *response* correction looks at only the scalar portion of the frequency response and can only compensate for tracking error terms due to the frequency response of the system. In a response calibration, a measurement made in the system is used to normalize the result with respect to a reference trace across the frequency span of the VNA. This method is generally no longer used [Agilent, 2002].

A vector calibration of the system can compensate for all six major error terms on both one-port and

two-port VNAs — for a total of 12 error terms — using a calibration against known measurement standards.

### 3.12.2 Systematic Error Modeling

There are six principal error terms that present themselves in the VNA. The errors are typically classified as being:

- Poor directivity of the directional element
- Poor port-to-port isolation through crosstalk around the DUT
- Source impedance mismatches causing additional reflection terms
- Load impedance mismatches causing inconsistent signal generation
- Poor system frequency response due to imperfect reflection tracing
- Poor measurement frequency response due to imperfect transmission tracking

These six error contributions occur in both the forward and reverse direction for any general case of an arbitrary two-port DUT, as with this radar configuration. These errors occur in both the forward and reverse transmission case, giving 12 total error terms when measuring a two-port DUT with a two-port NA. In a practical implementation, the VNA used is not a true, two-port VNA and is capable of only transmission–reflection measurements and no stimulus in the reverse direction.

For the simplicity of calculations, the reflection coefficient of the DUT is redefined as simply  $S$  which can be found by Equation (3.35) where  $a_1$  and  $b_1$  and the incident and reflected waves as discussed previously. Differing literature defines the terminology in differing ways. A cross-reference to the various terminology can be found at the conclusion of [Baier, 2009]. In this document, Baier's terminology has been adopted since it is the most simplistic without loss of generality for the purposes of a enhanced-

response calibration.

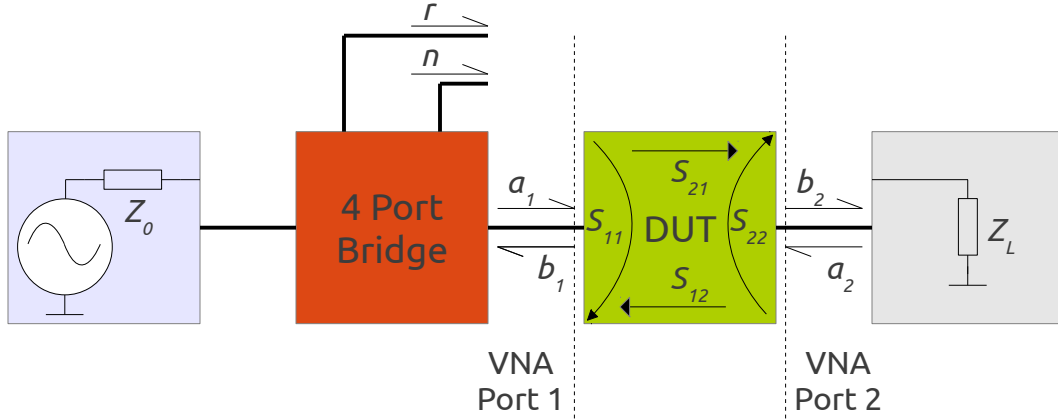


Figure 12: Model of two-port VNA with four port bridge error term calculation

The reflection coefficient looking into the terminated network is defined as  $S$ . In keeping with previous definitions, the complex signal incident to the DUT from the VNA is  $a_1$  and the total reflected signal is  $b_1$ .

$$S = \frac{b_1}{a_1} \quad (3.35)$$

In addition to the source signal and the output port to the DUT, the signals presented in the ideal test-set by use of a four-port bridge are the reflected signal  $r$  given by

$$r = \gamma \cdot a_1 + \delta \cdot b_1 \quad (3.36)$$

and the reference signal  $n$  is

$$n = \alpha \cdot a_1 + \beta \cdot b_1 \quad (3.37)$$

Since the networks are assumed to be linear, the total signal is given by a superposition of the components due to some proportion of  $a_1$  given by  $\gamma$  and  $\alpha$ , and some proportion of  $b_1$  given by  $\delta$  and  $\beta$ . This means that the total measured return to the measurement receiver,  $M$ , is given by

$$M = \frac{r}{n} = \frac{\gamma \cdot a_1 + \delta \cdot b_1}{\alpha \cdot a_1 + \beta \cdot b_1} \quad (3.38)$$

which then simplifies to

$$M = \frac{\gamma + \delta \cdot S}{\alpha + \beta \cdot S} \quad (3.39)$$

The Moebius transform [Baier, 2009] is then applied to give the equation in the form found by

$$M = \frac{S + a}{b \cdot S + c} \quad (3.40)$$

The variables  $a$ ,  $b$ , and  $c$  in the equations that follow are not related to the incident and reflected signals  $a_1$  and  $b_1$ . Notation was chosen to be consistent with notation in [Baier, 2009].

The reflection coefficient of the DUT can then be calculated using

$$S = \frac{a - c \cdot M}{b \cdot M - 1} \quad (3.41)$$

The VNA performance is then measured with known calibration standards which are open, shorted, and with a broadband 50-ohm load corresponding to the nominal system impedance  $Z_0$ . These measurements give responses  $M_{open}$ ,  $M_{short}$ , and  $M_{load}$ . Using Equation (3.41), the responses can be written as

$$M_{open} = \frac{S_{open} + a}{b \cdot S_{open} + c} \quad (3.42)$$

$$M_{short} = \frac{S_{short} + a}{b \cdot S_{short} + c} \quad (3.43)$$

and

$$M_{load} = \frac{S_{load} + a}{b \cdot S_{load} + c} \quad (3.44)$$

Solving for the parameters  $a$ ,  $b$ , and  $c$  gives

$$a = \frac{M_{load}(M_{open} - M_{short})}{M_{load}(M_{open} + M_{short}) - 2 \cdot M_{open} \cdot M_{short}} \quad (3.45)$$

$$b = \frac{2M_{load} - M_{open} - M_{short}}{M_{load}(M_{open} + M_{short}) - 2 \cdot M_{open} \cdot M_{short}} \quad (3.46)$$

and

$$c = \frac{M_{open} - M_{short}}{M_{load}(M_{open} + M_{short}) - 2 \cdot M_{open} \cdot M_{short}} \quad (3.47)$$

Finally, this can be generalized back to the performance of the bridge to show that, for any received response  $M$ , the result is comprised of the true reflection coefficient of the DUT,  $S$  and the terms  $a$ ,  $b$ , and  $c$  found in the three-point calibration with the open, short, and load terminations, i.e.,

$$M = \frac{S + a}{c \left( \frac{b}{c} \cdot S + 1 \right)} \quad (3.48)$$

While the terms  $a$ ,  $b$ , and  $c$  in the calibration do not have strict physical meanings beyond their mathematical definitions, they have been shown [Agilent, 2002] to be generally related to specific

parameters of the measurement bridge. It should be noted, however, that the true value of  $S$ , the reflection coefficient of the DUT, can be determined completely by parameters  $a$ ,  $b$ , and  $c$  without knowledge of the output impedance or directivity of the bridge. Those parameters, in turn, can be completely determined by measurement of known open, short, and load standards. This assumes that the standards are electrically perfect.

The parameter  $a$  is loosely related to the directivity error of the bridge [Agilent, 2002]. Only parameter  $c$  changes if the gain of the reflection or reference signals change [Rytting, 2009] and so this parameter is closely associated with reflection and transmission tracking errors. The  $b/c$  term is developed effectively in [Baier, 2009] by modeling the system as an ideal, perfectly matched four-port directional bridge and an additional two-port error network with scattering parameters  $E_{11}$ ,  $E_{21}$ ,  $E_{22}$  and  $E_{12}$  corresponding to  $S_{11}$ ,  $S_{21}$ ,  $S_{22}$  and  $S_{12}$  of the error network, each respectively. This is shown in *Figure 13*. Note that, in this document, the terminology for incident and reflected signals between the DUT and port two remains  $a_2$  and  $b_2$  for the sake of consistency and the signals  $a_{1'}$  and  $b_{1'}$  are introduced to account for the signals between the DUT and the error network, again following convention for the direction of flow between  $a_x$  and  $b_x$  signals.

The conventional definition of reflection coefficient looking into any arbitrary network is used to define  $E_{22}$ . The output resistance and output reflection coefficient looking into port one of the VNA when the stimulus  $a_1$  is set to zero is given by

$$S_s = \frac{b_{1'}}{a_{1'}} \Big|_{a_1=0} = E_{22} \quad (3.49)$$

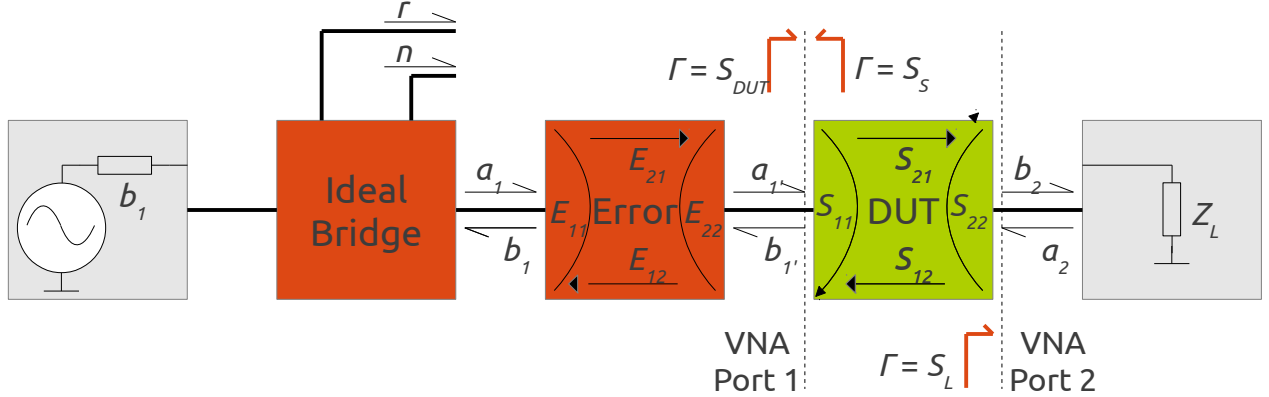


Figure 13: VNA model with error network and ideal bridge

When looking into the two cascaded networks, the error network followed by the DUT terminated by  $S_L$  at port two of the VNA, the input reflection coefficient is given by [Rytting, 2009] as

$$S_{DUT} = \frac{b_1}{a_1} = (E_{11}E_{22} - E_{12}E_{21}) \cdot \frac{S - E_{11}}{E_{22} \cdot S - 1} \quad (3.50)$$

Equation can be rearranged into the more familiar form given in [Baier, 2009] as

$$M = \frac{\frac{E_{11}}{S - \frac{(E_{11}E_{22} - E_{12}E_{21})}{(E_{11}E_{22} - E_{12}E_{21}) \cdot S - \frac{1}{(E_{11}E_{22} - E_{12}E_{21})}}}}{(E_{22} \cdot S - \frac{1}{(E_{11}E_{22} - E_{12}E_{21})})} \quad (3.51)$$

Equation (3.51) is of the same form as Equation (3.41) with the terms  $a$ ,  $b$ , and  $c$ , given as

$$a = -\frac{E_{11}}{(E_{11}E_{22} - E_{12}E_{21})} \quad (3.52)$$

$$b = \frac{E_{22}}{(E_{11}E_{22} - E_{12}E_{21})} \quad (3.53)$$

and

$$c = -\frac{1}{(E_{11}E_{22} - E_{12}E_{21})} \quad (3.54)$$

If the ratio  $b/c$  is then calculated, the result is

$$\frac{b}{c} = \frac{\frac{E_{22}}{(E_{11}E_{22} - E_{12}E_{21})}}{-\frac{1}{(E_{11}E_{22} - E_{12}E_{21})}} = -E_{22} \quad (3.55)$$

Then, using Equations (3.55) and (3.49), the real reflection coefficient looking into port one of the VNA including the ideal bridge and error network is

$$S_s = E_{22} = -\frac{b}{c} \quad (3.56)$$

When measuring the transmission magnitude and phase, as in this radar application, a transmission calibration must be performed in addition to the reflection coefficients. The signal detected by the receiver at port two, with the port two is a superposition of the signals  $a_2$  and  $b_2$ . The detected signal  $M_R$  is given by

$$M_R = a_2 + b_2 \quad (3.57)$$

Note that this notation is consistent with that used in HP technical information on VNA and corresponds to  $u_{det}$  in [Baier, 2009]. This can then be expanded to

$$M_R = a_2 + b_2 = b_2 + b_2 \cdot S_L = b_2(1 + S_L) \quad (3.58)$$

which then gives

$$\tau_F = \frac{M_R}{n} \quad (3.59)$$

### 3.12.3 Base Reference Oscillator

The work in [Tim, 2012] presented an analysis of oscillator stability for the published hobbyist VNA design. That analysis is repeated here with additional details and refinements, particularly in considering that the aim is to compute the error in relative depth between successive measurements, not to calculate the absolute depth error. For the purposes of this analysis, the terms depth and thickness are used interchangeably to indicate the true ice sheet thickness change between measurements whether described as a change in the depth of the ice bottom or as the total ice thickness.

First, the variability of the frequency of the oscillator is defined as a tolerance,  $T$ , for any measurement in which the ratio of the deviation in frequency to the actual frequency is merely the magnitude difference between desired frequency  $f_0$  and actual frequency of the oscillator  $f$ . This is given, with the  $T$  replaced with  $T_{freq}$  for clarity, by

$$T_{freq} = \frac{\Delta f}{f} = \frac{|f_0 - f|}{f_0} \quad (3.60)$$

Further, the prior work describes the error,  $E$ , in measured depth as

$$E_{depth} = \frac{|d_0 - d|}{d_0} \quad (3.61)$$

with  $d_0$  equal to true depth and  $d$  the measured depth. In this thesis,  $E$  is replaced with  $E_{depth}$  to prevent confusion.

Examining the error in absolute depth is not a particularly good way to look at error term resulting from frequency — that is, phase — errors since the purpose of this instrument is to measure relative changes in ice sheet thickness, not the absolute thickness. For the many reasons previously discussed, the absolute thickness error will be many times larger than the differential change in thicknesses between successive measurements. Therefore, in this thesis, the error in thickness differences between two are calculated later in this process in which differential thickness error between two successive measurements is given by

$$E_{\Delta d} = \frac{|\Delta d_0 - \Delta d|}{\Delta d_0} \quad (3.62)$$

Consider that for mixers, the output is the sum and difference frequencies of the mixer inputs, i.e.,

$$f_1 \otimes f_2 = \begin{cases} f_1 + f_2 \\ f_1 - f_2 \end{cases} \quad (3.63)$$

The true frequency output DDS,  $f_{DDS}$ , circuits is, neglecting alias, harmonic, and spur products, the input frequency from the XO,  $f_{XO}$  multiplied by some factor  $M_{DDS}$ , which is the sum of the total product of the DDS internal PLL's  $M$  multiplication ratio,  $1/D$  divisor ratio, and  $f_{tune}$  digital divide ratio frequency tuning word. The simplification that  $M_{DDS}$  is a strictly scalar frequency multiplication is considered here as the frequency sources are synchronized in phase reference to the XO.  $M_{DDS}$  is given by

$$M_{DDS} = M \cdot \frac{1}{D} \cdot \frac{1}{f_{tune}} \quad (3.64)$$

with

$$f_{DDS} = (M_{DDS} \cdot f_{XO}) \quad (3.65)$$

For each DDS, the RF generator and the local oscillator, Equation (3.65) gives

$$f_{DDSI} = (M_{DDSI} \cdot f_{XO}) \quad (3.66)$$

and

$$f_{DDS2} = (M_{DDS2} \cdot f_{XO}) \quad (3.67)$$

If (3.63) is then applied to the DDS frequency in the receiver mixers, the result is

$$f_{IF} = f_{DDSI} \otimes f_{DDS2} = \begin{cases} f_{DDSI} + f_{DDS2} \\ f_{DDSI} - f_{DDS2} \end{cases} \quad (3.68)$$

If the receiver mixer output is then low-pass filtered, the result is only the difference frequency product at an IF,  $f_{IF}$ , which is given as

$$f_{IF} \xrightarrow{LPF} |f_{DDSI} - f_{DDS2}| \quad (3.69)$$

The simplification of looking at only the low-pass filtered signal is a reasonable one because the frequency spread between the mix products is large given the choice of the LO frequency (DDS2) and the selectivity of the receiver is high and so only an appreciable component of the lower product — the difference — will be present.

Equations (3.66) and (3.67) are substituted into (3.69) to give

$$f_{IF} = f_{XO} |M_{DDSI} - M_{DDS2}| \quad (3.70)$$

the sampled IF frequency.

To introduce the frequency error, consider the true XO frequency,  $f_{XO}$ , to be some desired frequency  $f_{XO'}$  plus an error of  $\delta$  where  $\delta$  is in the same units as  $f_{XO'}$ . This gives the true XO frequency as

$$f_{XO} = f_{XO'} + \delta \quad (3.71)$$

Applying Equation (3.71) to (3.66) and (3.67) gives

$$f_{DDS1} = M_{DDS1}(f_{XO'} + \delta) \quad (3.72)$$

and

$$f_{DDS2} = M_{DDS2}(f_{XO'} + \delta) \quad (3.73)$$

Until this point, the analysis presented has followed that presented in [Tim, 2012]. In a departure from that analysis, three cases are presented here.

Case A is one presented in the prior work in which the instability of the XO manifests after the RF stimulus has been launched from the transmitting antenna, while the wave is propagating through the ice, and occurs before the wave is recovered at the receiver. This implies that for the purposes of calculating the IF, there is no error in the DDS1 terms but there is an error in DDS2 terms. This leads to a situation in which the reference is described by Equation (3.66) but the LO is described by (3.73). When the generally-applicable Equation (3.70) is populated with these  $f_{DDS}$  terms, the result is

$$f_{IF} = \left[ f_{XO'} |M_{DDS1} - M_{DDS2}| \right] + \delta \cdot M_{DDS2} \quad (3.74)$$

If tolerance is then computed using (3.60), the result is

$$T_{IF} = \frac{\delta \cdot M_{DDS2}}{f_{XO} \cdot |M_{DDS1} - M_{DDS2}|} \quad (3.75)$$

for Case A, identical to the result presented in [Tim, 2012].

Similarly, a Case B can be constructed when the instability of the XO manifests while the transmitting wave is being launched by the RF stimulus through the transmitting antenna, while the wave is propagating through the ice. If the XO then returns to normal frequency  $f_{XO}$  before the generated receiver LO is applied — before the wave is recovered at the receiver — then an error term with a  $M_{DDS2}$  product is found. This implies that for the purposes of calculating the IF, there is no error in the DDS2 terms but is an error in DDS1 terms. This leads to a situation in which the reference is described by Equation (3.72) but the LO is described by (3.67). When the generally-applicable Equation (3.70) is populated with these  $f_{DDS}$  terms, the result is

$$f_{IF} = [f_{XO} \cdot |M_{DDS1} - M_{DDS2}|] + \delta \cdot M_{DDS1} \quad (3.76)$$

If tolerance is then computed using (3.60), the result is

$$T_{IF} = \frac{\delta \cdot M_{DDS1}}{f_{XO} \cdot |M_{DDS1} - M_{DDS2}|} \quad (3.77)$$

for Case B.

Finally, a Case C can be constructed when the instability of the XO manifests both while the transmitting wave is being launched by the RF stimulus through the transmitting antenna, while the wave is propagating through the ice, and while the LO is generating the receiver output based on the XO input. This gives the simple case where the reference is described by Equation (3.72) but the LO is described by

(3.73). When the generally-applicable Equation (3.70) is populated with these  $f_{DDS}$  terms, the result is

$$f_{IF} = \left[ (f_{XO} + \delta) |M_{DDS1} - M_{DDS2}| \right] \quad (3.78)$$

If tolerance is then computed using (3.60), the result is

$$T_{IF} = \frac{\delta}{f_{XO} |M_{DDS1} - M_{DDS2}|} \quad (3.79)$$

for Case C.

The results for the above cases are correct, assuming everything else about the signal chain is accurate save the LO frequency — and by extension the phase. This is likely not the case. Moreover, the true goal of this thesis is to perform highly accurate relative thicknesses measurements between successive interrogations of the ice sheet thickness.

Having determined the effect of the instability in the base reference oscillator on output LO, it can be related back to the depth in two ways.

This treatment of the error is contingent on an assumption of a known, continuous phase velocity within the ice sheet. In reality, the phase velocity must be assumed. This is why it is foolish to attempt to determine absolute thickness with high accuracy.

A better way to think of the real error problem with the reference oscillator is to realize that the random jitter of the oscillator is distributed Gaussian about some mean frequency. If a sufficiently large number of phase and magnitude samples are taken and averaged, the mean of those samples will converge and eliminate the random jitter or phase noise. Averaging is the first part of the strategy.

The second step in understanding the real accuracy problem is to look at  $\delta$  as a long term drift with

temperature variation and aging and not as short time-scale random process. If the thickness change is the only concern between a series of 2 successive measurement, then the drift of the measured output IF frequency for a drift in the oscillator  $\delta$  is given as

$$f_{IF1} = [f_{XO'} |M_{DDSI} - M_{DDS2}|] \quad (3.80)$$

and with

$$f_{IF2} = [(f_{XO'} + \delta) |M_{DDSI} - M_{DDS2}|] \quad (3.81)$$

giving the reference term.

The error recorded in phase is the phase change over the two-way travel path between the two frequencies and is computed by using Equation (3.80) to arrive at a depth  $d_l$  and phase  $\varphi_l$ . Equation (3.81) is then used to find the same for the case with  $\delta$  introduced. First, notice that the returned phase of the signal,  $\varphi_r$ , is determined by the depth (thickness) or the ice given as  $d$ , the frequency, and the velocity of propagation in the ice. This is then multiplied by 2 to obtain the two-way travel phase. This is given by

$$\varphi_r = 2 d \cdot \left( \frac{2\pi f}{v_p} \right) = d \frac{4\pi f}{v_p} \quad (3.82)$$

The change in depth between measurements will then be the measured phase difference multiplied by the wavelength in the media, as given by

$$\Delta d = \frac{(\varphi_{r2} - \varphi_{rl})}{4\pi} \cdot \frac{v_p}{f} \quad (3.83)$$

If Equation (3.81) and (3.82) are then substituted into (3.82) to give the received phases  $\varphi_{rl}$  and  $\varphi_{r2}$  or the initial measurement assumed to be stable and the successive measurement with the frequency error  $\delta$ ,

the resulting expressions are given by

$$\varphi_{rl} = d \frac{4\pi f}{v_p} = d \frac{4\pi}{v_p} [(f_{xo'}) |M_{DDS1} - M_{DDS2}|] \quad (3.84)$$

and

$$\varphi_{r2} = d \frac{4\pi f}{v_p} = d \frac{4\pi}{v_p} [(f_{xo'} + \delta) |M_{DDS1} - M_{DDS2}|] \quad (3.85)$$

The error in the thickness change measurement can then be found by computing Equation (3.83) with the initial phase of Equation (3.84) and the phase with the frequency error of Equation (3.85). The result is

$$E_{\Delta d} = \frac{d \frac{4\pi}{v_p} [(f_{xo'} + \delta) |M_{DDS1} - M_{DDS2}|] - d \frac{4\pi}{v_p} [(f_{xo'}) |M_{DDS1} - M_{DDS2}|]}{4\pi} \cdot \frac{v_p}{f_{xo'}} \quad (3.86)$$

which can be reduced to

$$E_{\Delta d} = |M_{DDS1} - M_{DDS2}| \cdot [f_{xo'} + \delta - f_{xo'}] \cdot \frac{d}{f_{xo'}} \quad (3.87)$$

and then further simplified to

$$E_{\Delta d} = |M_{DDS1} - M_{DDS2}| \delta \cdot d \frac{1}{f_{xo'}} \quad (3.88)$$

When evaluating the repercussions of Equation (3.88), notice a number of implications about factors that impact the accuracy of the relative depth measurement. The error in depth measurement change between measurements is dependent on the depth measured. This is intuitive since when measuring a deep feature, the wave will need to travel more cycles and consistent errors of wavelength will compound more over the greater distance. Further, the total error is related to the difference between DDS frequencies. This is also intuitive since larger multiplication ratios mean larger multiples of the error terms as well. Finally,

note that the error is related inversely to  $f_{xo}$ . This may seem counter intuitive, but recall that the error has been treated as an absolute deviation in Hz, not as a percentage deviation from center frequency, which is a more logical way to express the deviation.

## **CHAPTER 4: ANTENNA DESIGN**

Traditional antenna designs for GPR and, by extension, IPR are dipoles that are heavily loaded with lossy material to dampen the ringing from the extremely wideband pulses that are typically employed [Peters, 1994]. However, in the case of this design, the transmit wave is highly linear and confined to VHF and UHF frequencies and thus such loading is unnecessary. The goal, therefore, is to produce optimal gain and T/R isolation since the waves are CW and not pulses which provides inherent T/R isolation via blanking.

When the propagating signal impinges on the ground, the wavefront can be characterized as a two-component system containing a spherical wavefront propagating out from the antenna and a plane wave in the ground traveling at the critical angle. Because this work uses horizontally polarized radiation and the direction of the antenna is nadir, the surface-wave term can be neglected in the far-field case.

### **4.1 Antenna RF Performance Requirements**

While the transmit and receive antennas for the radar system do not have explicit gain requirements, the idea of maximizing practical antenna gain realizable in an antenna that can be carried to the site by the research team is critical. To this end, the type of linearly-polarized antenna that is best suited for this application has been chosen, the log-periodic type antenna. The basic design goals are presented below with none being a strict requirement.

Design Goals:

- Gain  $\approx 10$  dBi
- VSWR  $\leq 2.0:1$

- Polarization: Horizontal Linear
- Cross-Polarization  $\leq$  -20 dB
- Weight  $\leq$  20 lbs
- Durability for Harsh Environment

The university has already available several CREATIVE Design Corp CLP5130-2 log-periodic type antennas from a previous ice-penetrating radar investigation. The published specifications for the antenna are given in *Table 6*.

Specification	Value
Low Frequency Limit	105 MHz
High Frequency Limit	1300 MHz
Antenna Type	Log-Periodic
Polarization	Linear (Horizontal)
Forward Gain	11–13 dBi
F-B Ratio	15 dB
Half-Power Beamwidth	65 degrees
Power Rating	500 W CW
Boom Length	1.4 meters
VSWR	VSWR $\leq$ 2.0:1

*Table 6: CLP5130-2 Log-Periodic antenna data*

The first design goal was to examine the previous work of [Mendoza, 2012] and model the antenna true performance in the ice environment. A combination of analysis of the supplied CLP5130-2 installation manual and measurements of a similar CDG antenna were used to reverse engineer an electromagnetic model of the antennas with reasonably high geometric fidelity. In the following sections, the antenna is analyzed mathematically where prudent approximations allow for use of closed-form analytical solutions. The most detailed work, however, is completed with full-wave electromagnetic simulation using FEKO.

## 4.2 Design Equation Background

The most important concept to consider when looking at the impact of antenna design on the overall IPR performance is that of the mutual coupling between the transmitting and receiving antennas. In general form, for simplistic dipole antenna, the actual impedance of the antenna *in situ* is the called driving point impedance. Driving point impedance is a combination of the self impedance of the antenna — the impedance seen at the antenna terminals in the absence of any other conductors or dielectrics — and the mutual impedance which accounts for the effect of these other structures and materials.

To find the mutual driving point impedance given the tranmitting and receiving antenna coupling, consider the voltage at the feedpoint of antenna 1 as

$$V_1 = Z_{11}I_1 + Z_{12}I_2 \quad (4.1)$$

with antenna 2 having voltage given by

$$V_2 = Z_{21}I_1 + Z_{22}I_2 \quad (4.2)$$

The impedance then seen at the terminals of antenna 1 is

$$Z_{12} = \frac{V_1}{I_2} \Big|_{I_1=0} \quad (4.3)$$

Likewise, the impedance seen at the terminals of antenna 2 is then given by

$$Z_{21} = \frac{V_2}{I_1} \Big|_{I_2=0} \quad (4.4)$$

This means that the the mutual term can be thought of as

$$Z_{22} = \frac{V_2}{I_2} \Big|_{I_1=0} \quad (4.5)$$

with

$$Z_{1d} = \frac{V_1}{I_1} = Z_{11} + Z_{12} \cdot \left( \frac{I_2}{I_1} \right) \quad (4.6)$$

$$Z_{2d} = \frac{V_2}{I_2} = Z_{22} + Z_{21} \cdot \left( \frac{I_1}{I_2} \right) \quad (4.7)$$

The impedances can then be found by integrating the current distribution over the length of the antenna. If an approximately dipole-like sinusoidal current distribution is assumed , this then gives

$$V_{21} = - \left( \frac{1}{I_{2i}} \right) \cdot \int_{-L_z/2}^{L_z/2} E_{z2l}(z') I_2(z') dz' \quad (4.8)$$

$$Z_{21i} = \frac{V_{21}}{I_{1i}} = - \left( \frac{1}{I_{1i} \cdot I_{2i}} \right) \cdot \int_{-L_z/2}^{L_z/2} E_{z2l}(z') I_2(z') dz' \quad (4.9)$$

$$V_{21} = - \left( \frac{1}{I_{2i}} \right) \cdot \int_{-L_z/2}^{L_z/2} E_{z2l}(z') I_2(z') dz' \quad (4.10)$$

Where  $I_z$  is the total current distribution on the conductor, for a diopole,

$$I_z = 2\pi a J_z = I_m \sin \left[ k \left( \frac{1}{2} - |z'| \right) \right] \quad (4.11)$$

For Side By Side (broadside) coupled antennas as were considered in [Mendoza, 2012],  $R_{21m}$  reduces to

$$R_{21m} = \left( \frac{\eta}{4 \cdot \pi} \right) [2C_i(u_0) - C_i(u_1) - C_i(u_2)] \quad (4.12)$$

The reactive components can then be calculated by

$$X_{21m} = -\left(\frac{\eta}{4\pi}\right)[2S_i(u_0) - S_i(u_1) - S_i(u_2)] \quad (4.13)$$

given that

$$\mu_0 = kd \quad (4.14)$$

and that

$$u_1 = k\left(\sqrt{d^2 + l^2} + l\right) \quad (4.15)$$

and

$$u_2 = k\left(\sqrt{d^2 + l^2} - l\right) \quad (4.16)$$

For collinear antennas as recommended for this application, the resistive and reactive components are given by

$$\begin{aligned} R_{21m} = & -\left(\frac{\eta}{8\pi}\right) \cdot \cos(v_0) \cdot [-2C_i(2v_0) + C_i(v_2) + C_i(v_1) - \ln(v_3)] \\ & + \left(\frac{\eta}{8\pi}\right) \cdot \sin(v_0) \cdot [2S_i(2v_0) - S_i(v_2) - S_i(v_1)] \end{aligned} \quad (4.17)$$

and

$$\begin{aligned} X_{21m} = & -\left(\frac{\eta}{8\pi}\right) \cdot \cos(v_0) \cdot [-2C_i(2v_0) + C_i(v_2) + C_i(v_1) - \ln(v_3)] \\ & + \left(\frac{\eta}{8\pi}\right) \cdot \sin(v_0) \cdot [2S_i(2v_0) - S_i(v_2) - S_i(v_1)] \end{aligned} \quad (4.18)$$

These driving point impedance approximations are factored into the full-wave simulation of the antenna given the calculated current distributions present on the antenna elements.

### 4.3 Full Wave Simulation of Antenna

Because rigorous analysis of a practical log-periodic antenna is difficult if not impossible analytically — it requires simplifications about the thickness of conductors, which is impractical — the most accurate way to analyze the performance of the antenna is with electromagnetic modeling using full-wave type simulation in FEKO. The geometry configuration for a single antenna is shown in *Figure 14*. The geometry with respect to the modeled snow surface is shown in *Figure 15*.

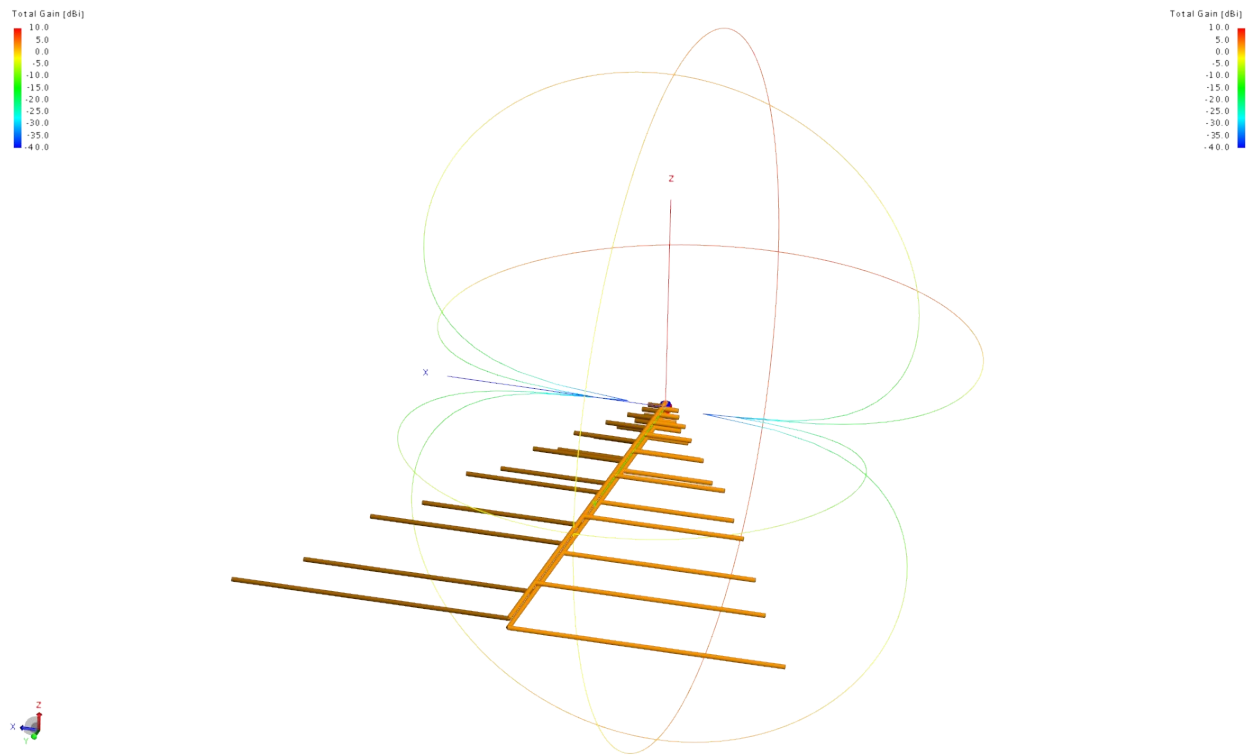


*Figure 14: Single antenna geometry with radiation pattern cuts, snow media suppressed*

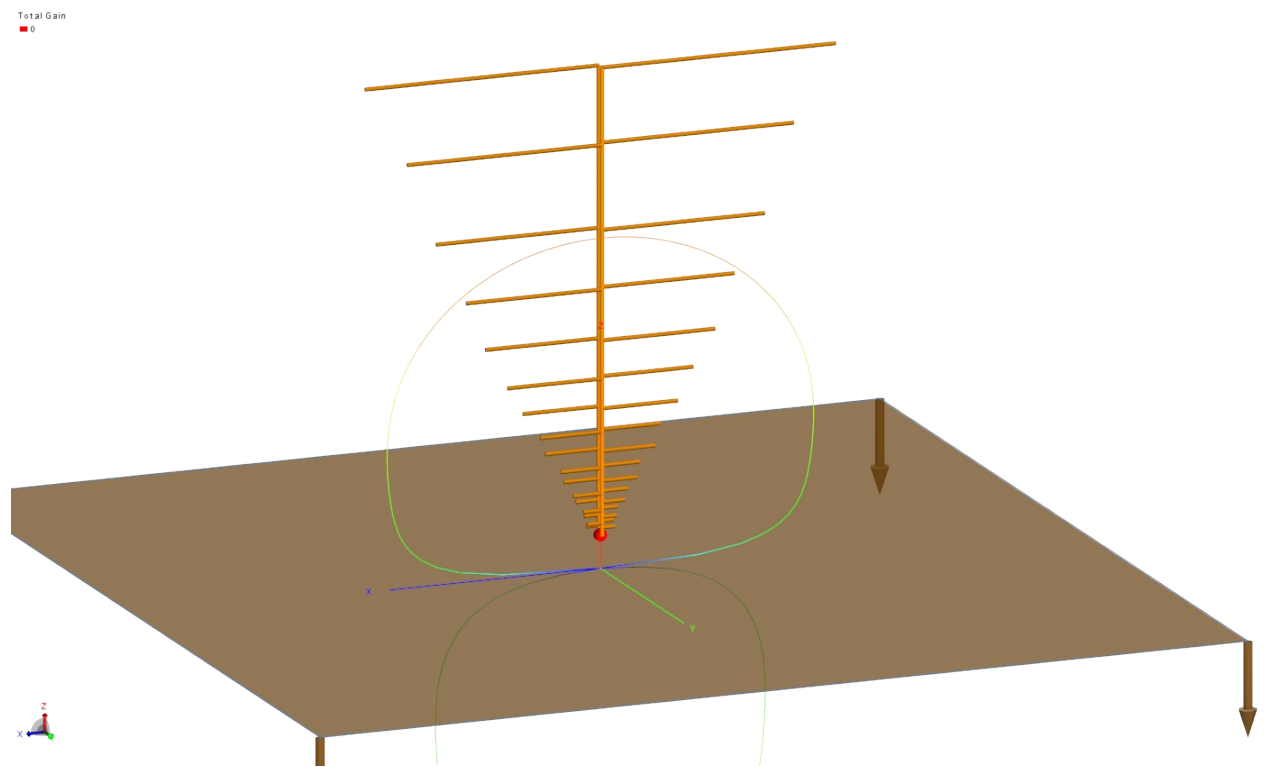
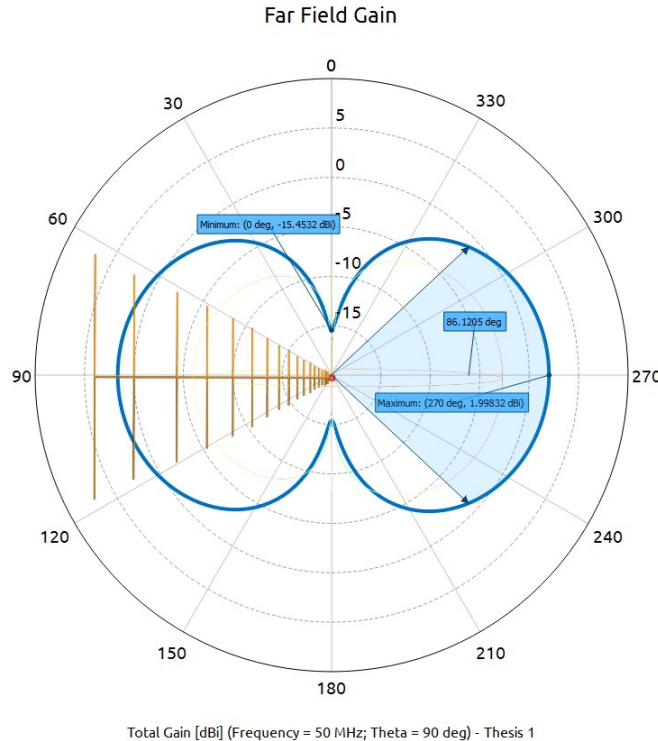
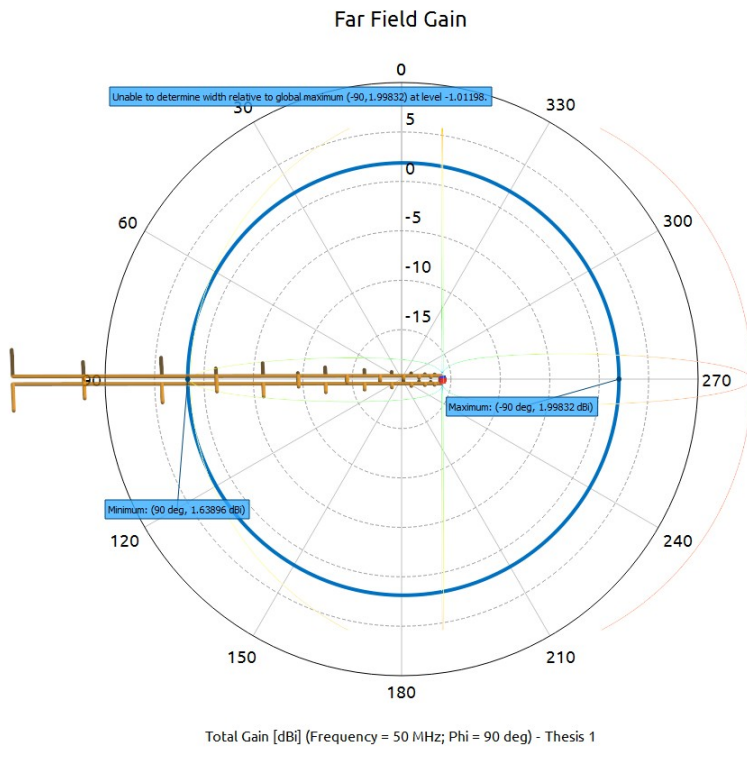


Figure 15: Antenna model setup with log-periodic position 10 cm above modeled snow



*Figure 16: Antenna gain with loading of snow media, 50 MHz, E-Plane*

The antenna performance was then swept from 50 MHz – 500 MHz in 50-MHz increments. The most critical pattern cut with show the radiation into the ice are presented below.



*Figure 17: Antenna gain with loading of snow media, 50 MHz, H-Plane*

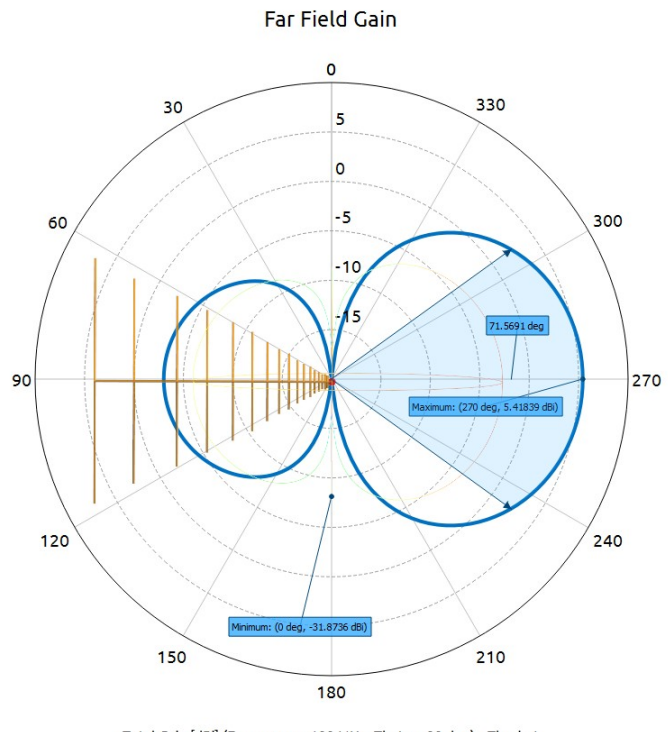


*Figure 18: Antenna gain with loading of snow media, 100 MHz, E-Plane*

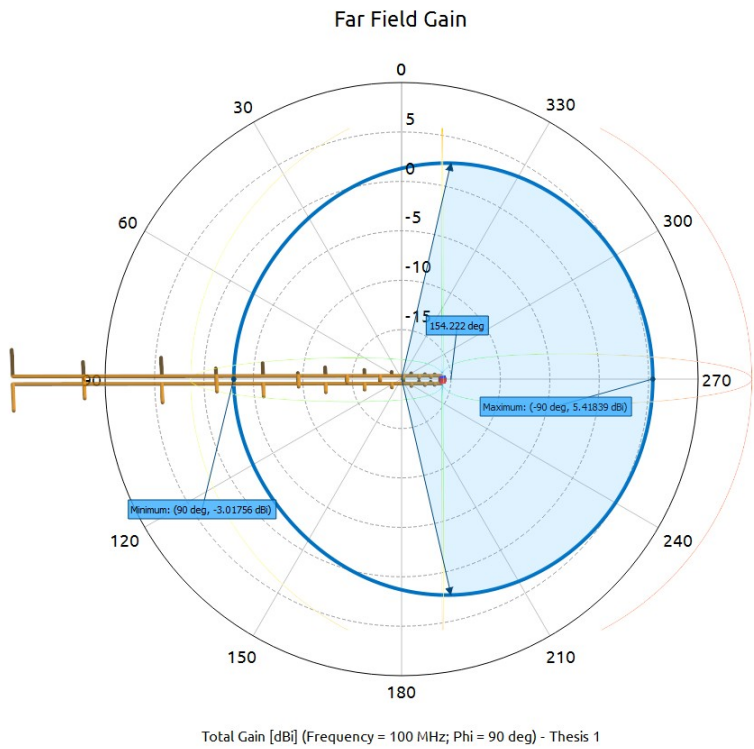


*Figure 19: Antenna gain with loading of snow media, 100 MHz, H-Plane*

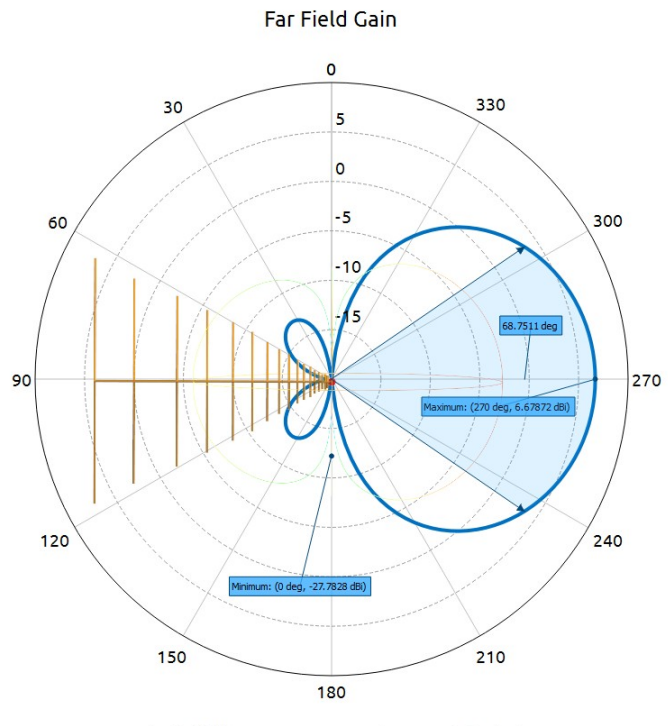


*Figure 20: Antenna gain with loading of snow media, 150 MHz, E-Plane*

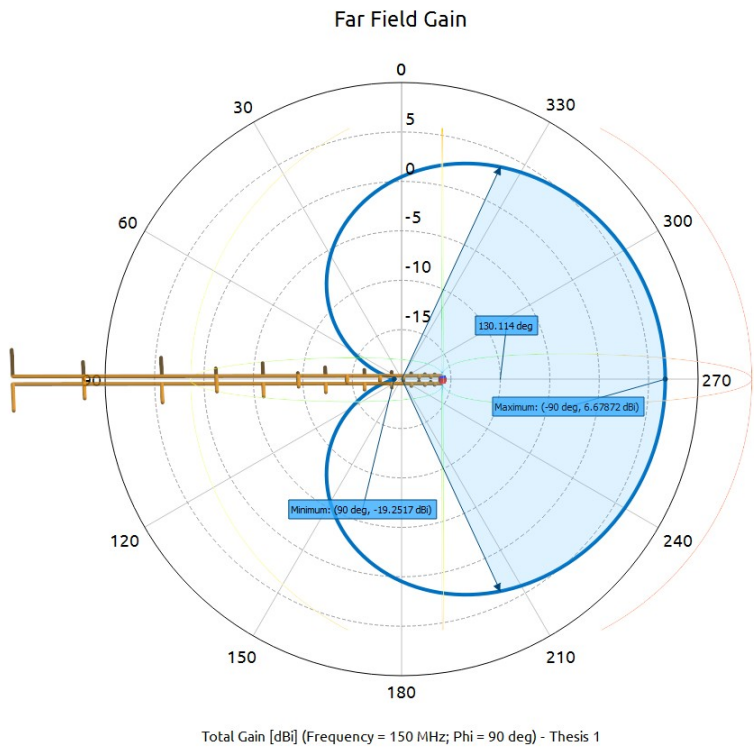


*Figure 21: Antenna gain with loading of snow media, 150 MHz, H-Plane*

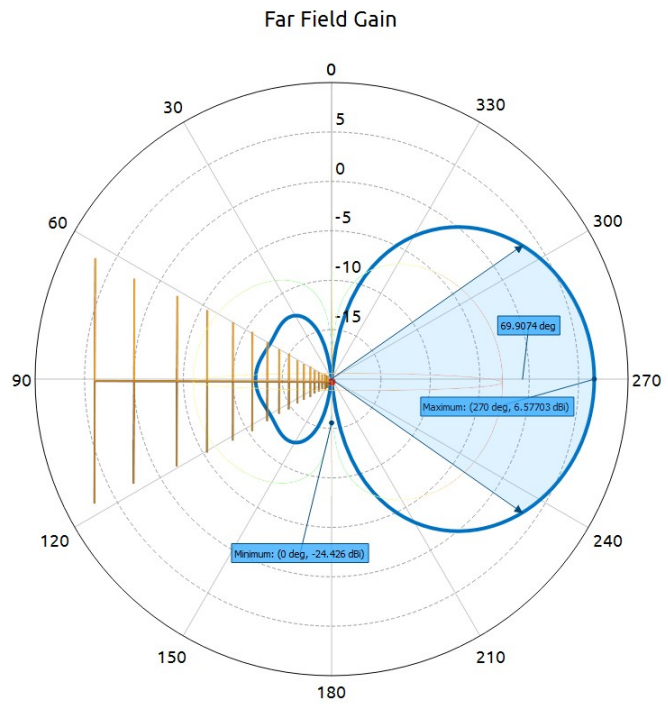


*Figure 22: Antenna gain with loading of snow media, 200 MHz, E-Plane*

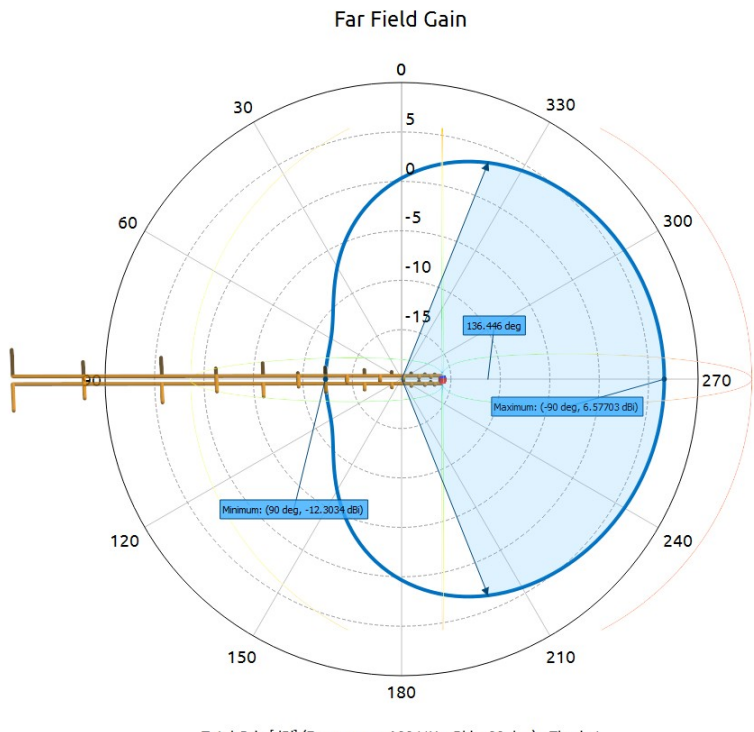


*Figure 23: Antenna gain with loading of snow media, 200 MHz, H-Plane*

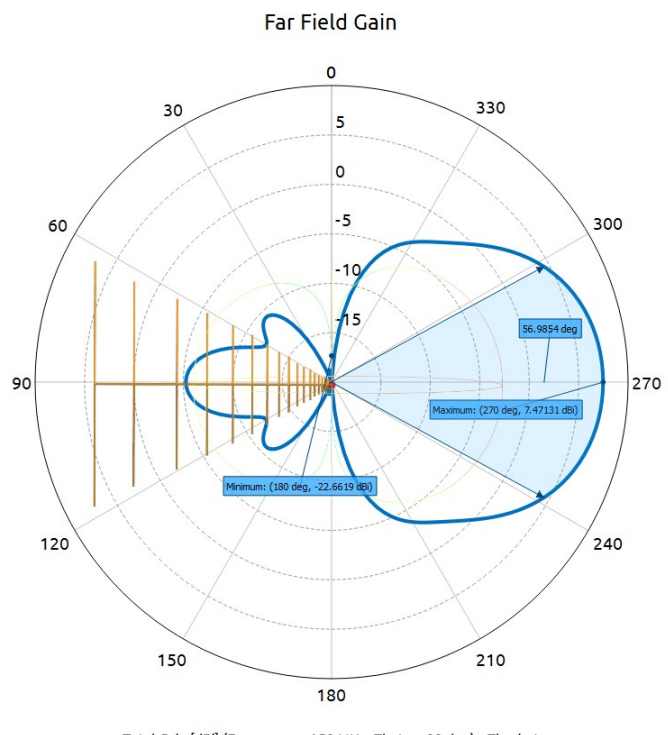


*Figure 24: Antenna gain with loading of snow media, 250 MHz, E-Plane*

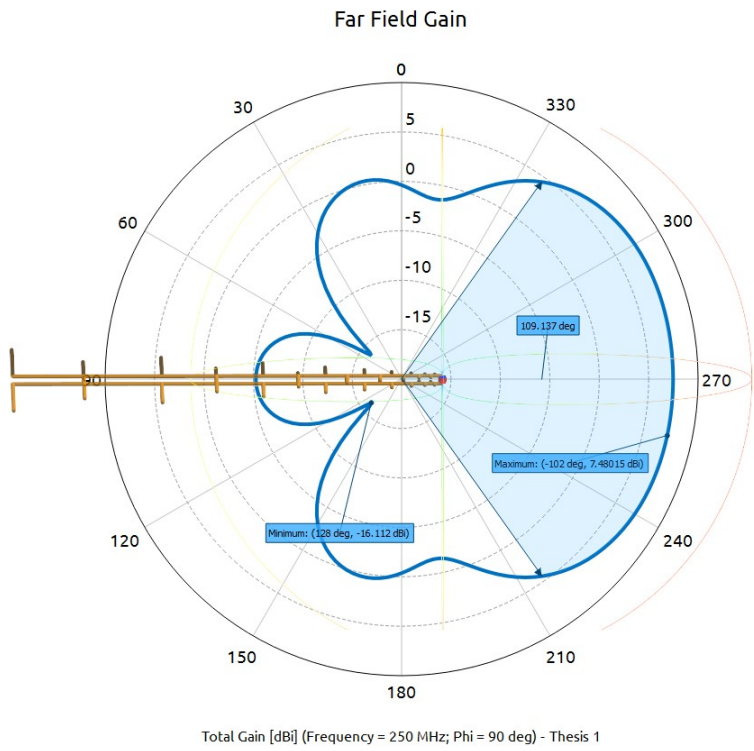


*Figure 25: Antenna gain with loading of snow media, 250 MHz, H-Plane*

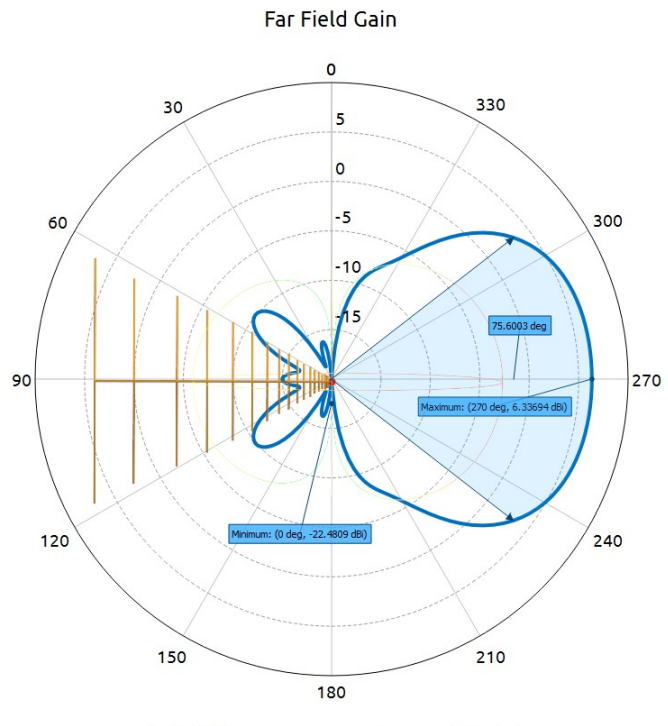


*Figure 26: Antenna gain with loading of snow media, 300 MHz, E-Plane*

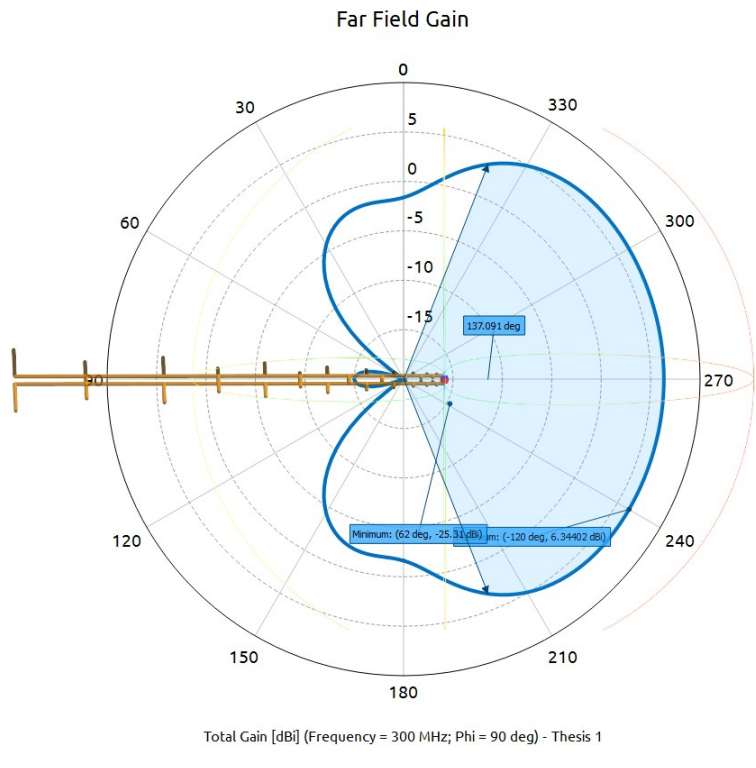


*Figure 27: Antenna gain with loading of snow media, 300 MHz, H-Plane*

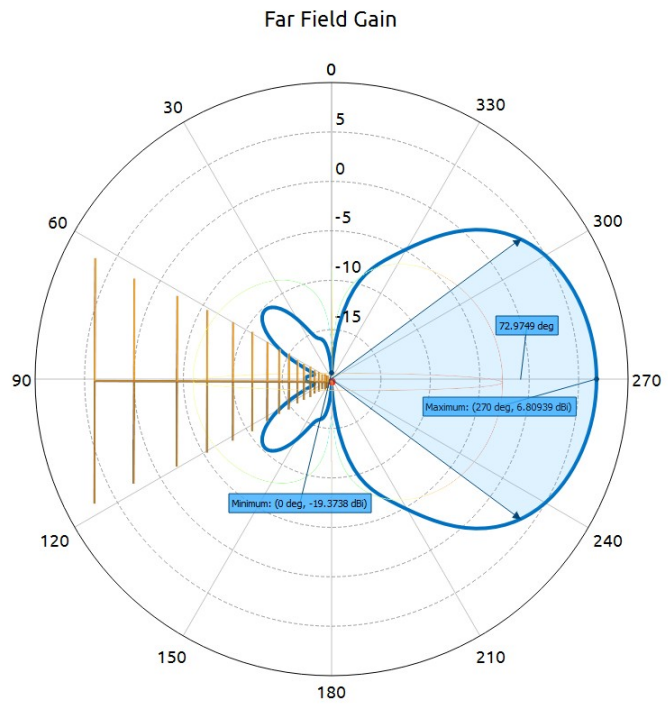


*Figure 28: Antenna gain with loading of snow media, 350 MHz, E-Plane*

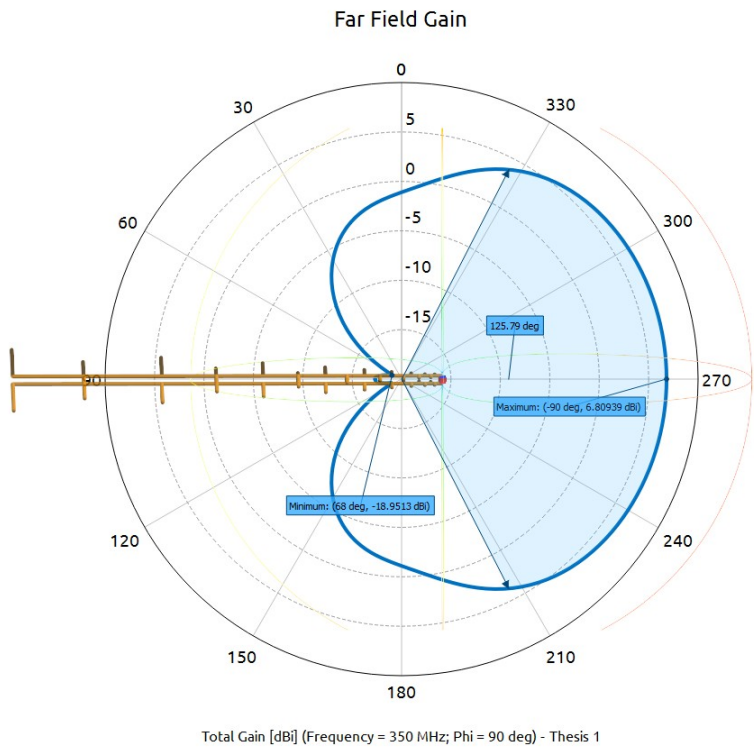


*Figure 29: Antenna gain with loading of snow media, 350 MHz, H-Plane*

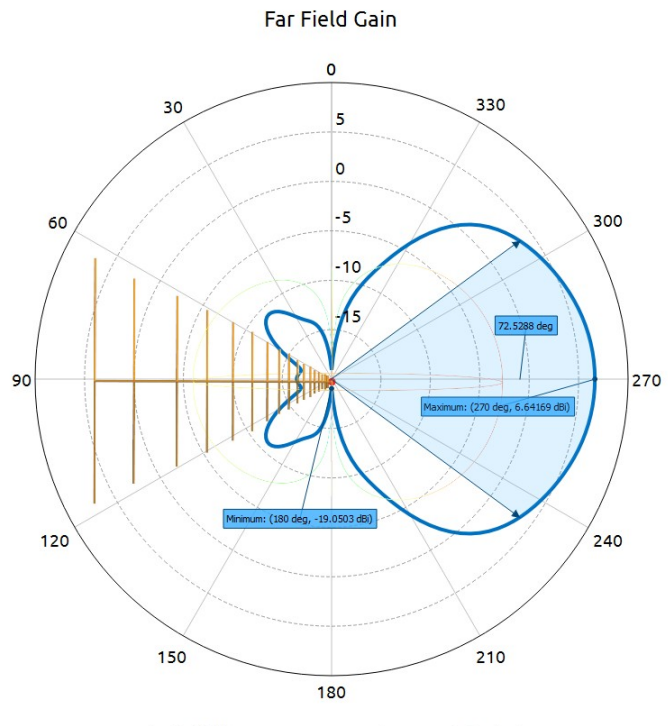


*Figure 30: Antenna gain with loading of snow media, 400 MHz, E-Plane*

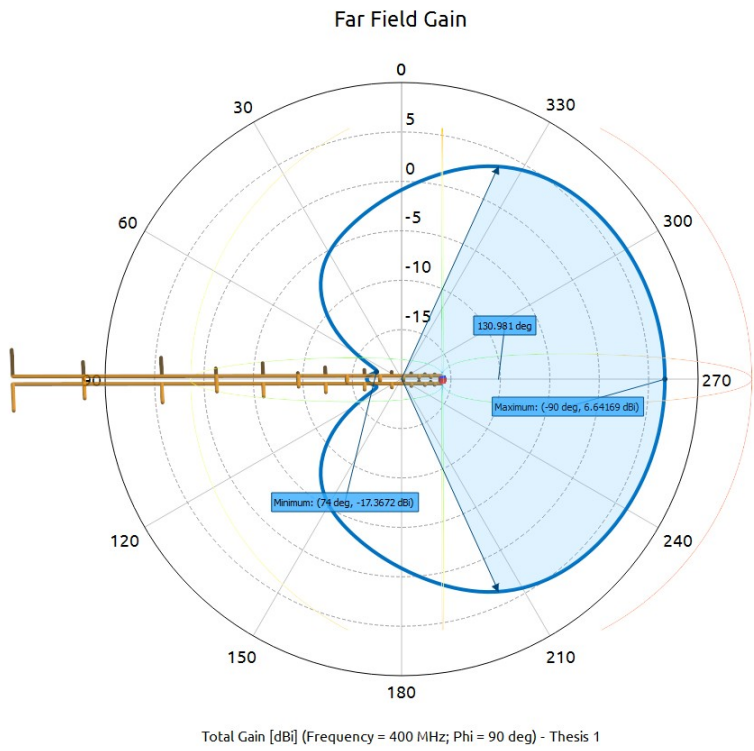


*Figure 31: Antenna gain with loading of snow media, 400 MHz, H-Plane*

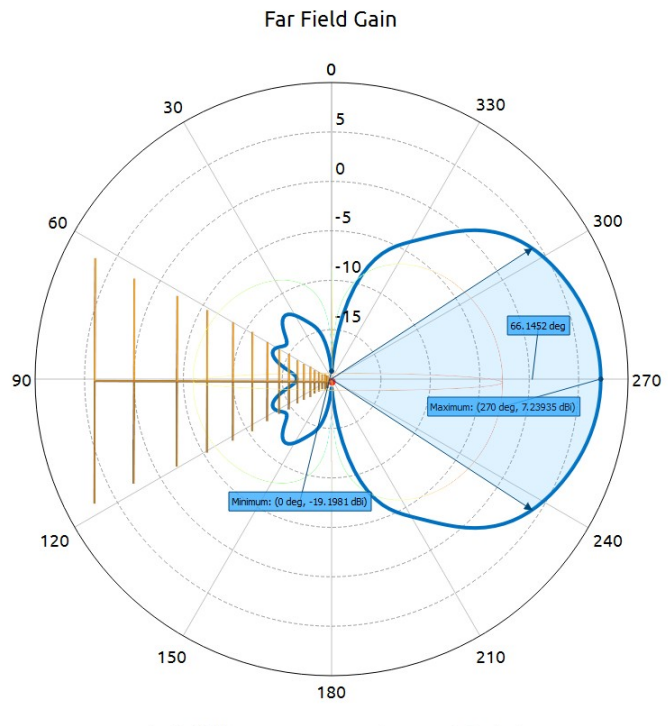


*Figure 32: Antenna gain with loading of snow media, 450 MHz, E-Plane*

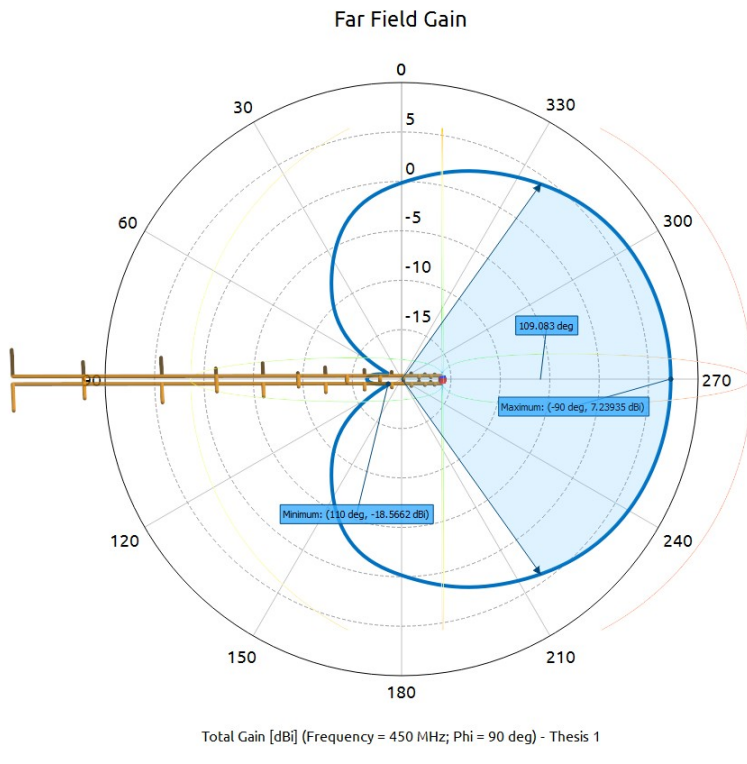


*Figure 33: Antenna gain with loading of snow media, 450 MHz, H-Plane*

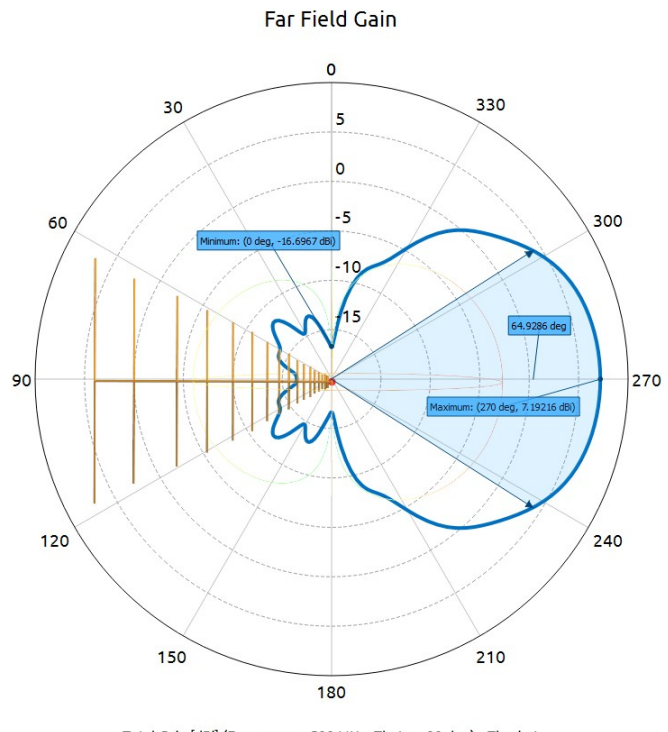


*Figure 34: Antenna gain with loading of snow media, 500 MHz, E-Plane*

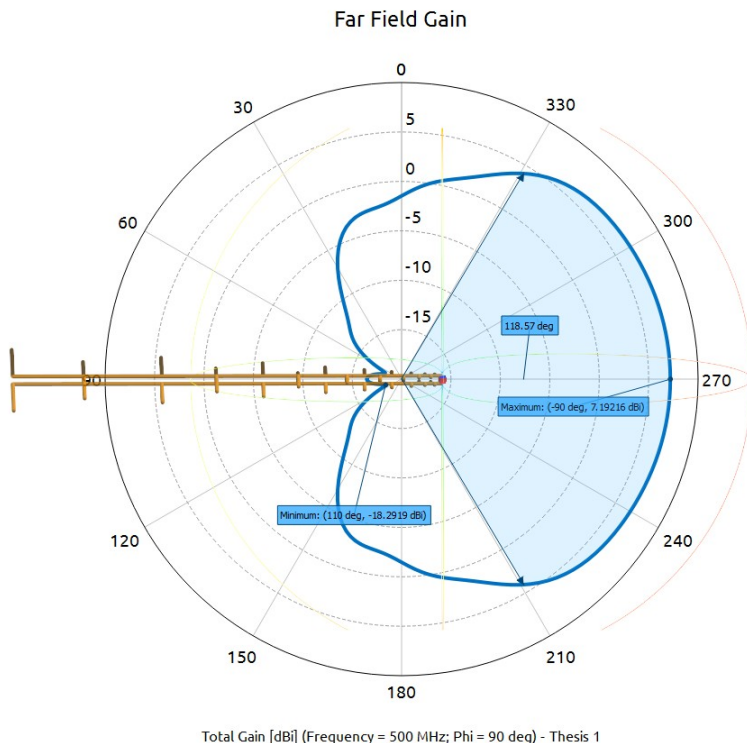


*Figure 35: Antenna gain with loading of snow media, 500 MHz, H-Plane*

## 4.4 Idealized Analysis of Transmit/Receive Coupling

Typical approaches to a reduction in coupling between transmit and receive antennas are the use of cross dipoles — wherein orthogonally polarized antennas are used — and the time domain-monopulse [Peters,1994] type antenna where parallel antennas of equal magnitude but opposite phase transmit and a receiving antenna is located between, experiencing a net of no signal [Barnes, 1994].

In previous ice-penetrating radars developed at the university, it appears that an antenna system error was made. Referring to the illustration of Figure 1-2 in [Mendoza, 2012], reproduced below as *Figure 36* , it appears that the log-periodic receive and transmit antenna arrays were configured parallel to one another such that they were directly broadside to one another. This exacerbates the coupling problem between transmitting and receiving antennas unnecessarily. It is important to consider the near-field interaction between the two rather than thinking in the context of far field gain at that angle. Using the above analysis, it can be approximated that the loading is significant. This was verified with full-wave simulation of the near-field interaction of the antennas using FEKO. The model setup for verification of this is shown in *Figure 37*.

For the work of this thesis, the recommendation is that that the antenna be placed coplanar — in their E-Plane — oriented such that the receive antenna is in the deep polarization mismatch null of the transmitting antenna. Because the antennas are pointed directly nadir, the angle subtended between them is virtually 0. From a far-field perspective, the propagation path is virtually identical but the near-field coupling problem is reduced significantly since the receive antenna is now in the deepest null of the transmitting antenna. The modeling configuration for full-wave simulation of this response in the near-field is shown in *Figure 38*.

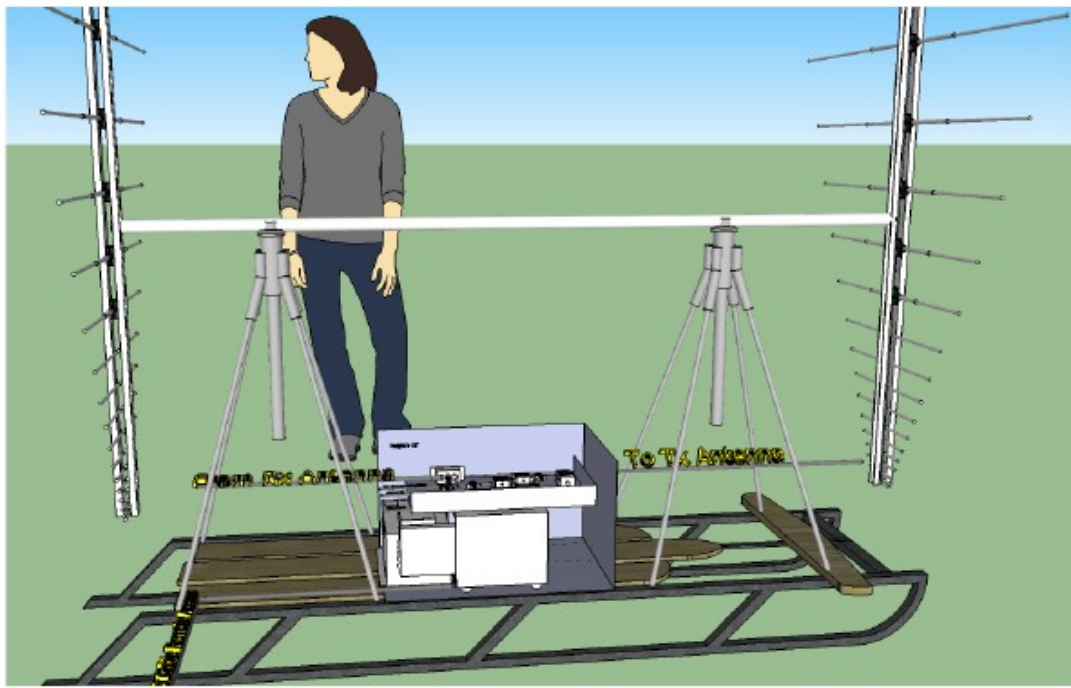


Figure 36: Previous Ice Radar system, reproduced from [Mendoza, 2012]

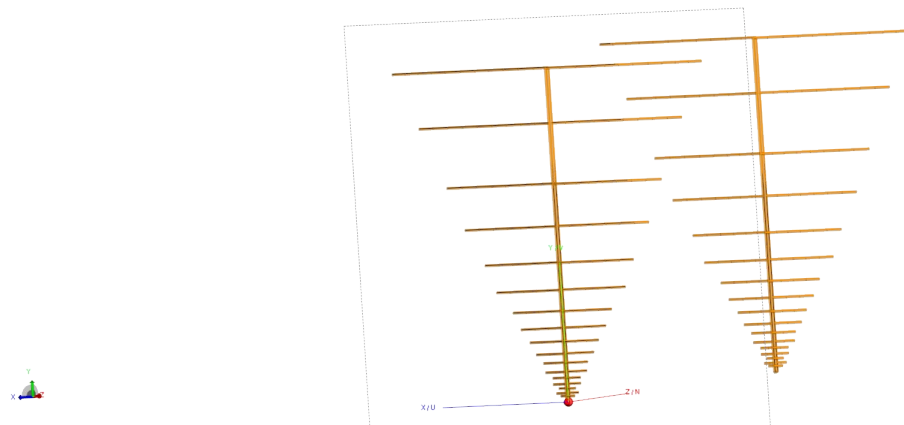


Figure 37: Previous antenna coupling model, antennas parallel and broadside

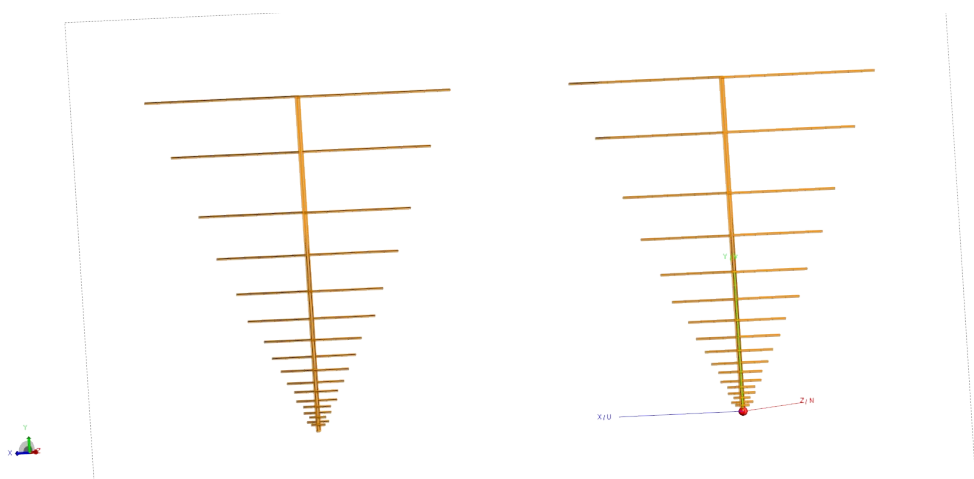
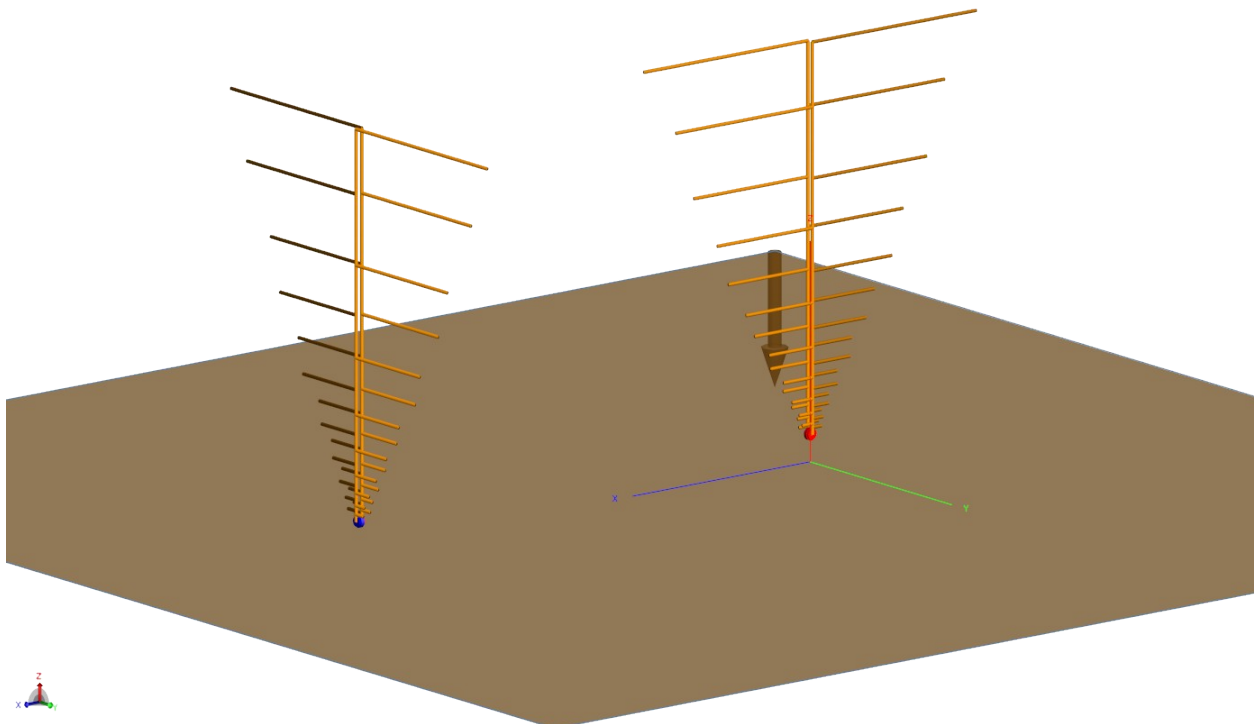


Figure 38: Antenna coupling model recommended collinear configuration

The other configuration that was studied was the case of the using the antennas mounted in an orthogonally polarization manner, i.e., with their polarizations 90 degrees with respect to one another. This is not the ideal configuration as it relies on rotation of the signal via the scatter of the internal reflectors and the ice bottom to permit reception. The research of this thesis has not determined what polarization rotation will occur at the ice sheet boundary but the coupling of the configuration was computed.



*Figure 39: Model setup for configuration with antennas oriented orthogonally polarized*

All the antenna configurations, the orthogonally polarized setup shown in *Figure 39*, the parallel polarization broadside configuration of *Figure 37*, and the parallel polarization collinear configuration of *Figure 38* were all modeled with moderate snow and ice conductivities to determine the coupling effects.

The model setup used a 1-V source on the transmitting antenna with a 50-ohm load as receiver on the receiving antenna. The absorbed power in the Rx antenna load was then modeled using the voltage and currents excited on the Rx antenna. The transmitted power levels and received power levels are plotted in *Figure 40*. The coupling, in dB, from the transmitting antenna to the receiving antenna is plotted in *Figure 41*.

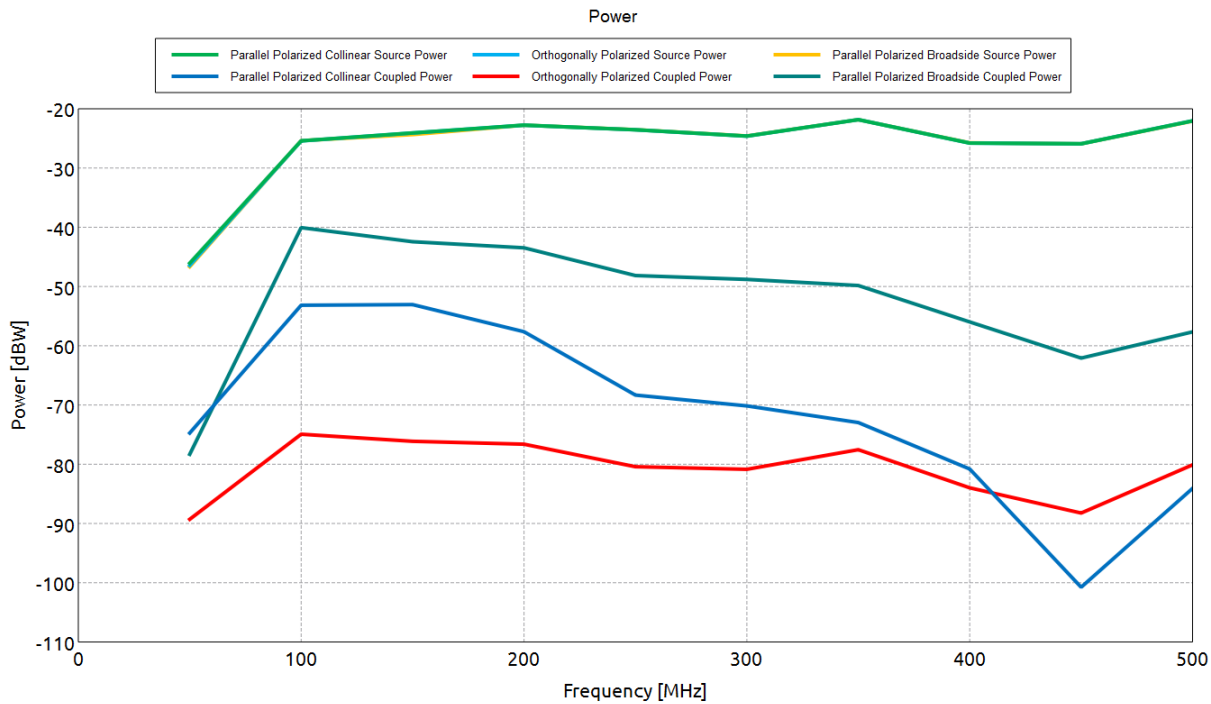


*Figure 40: Received power levels on coupled antennas of various configurations*

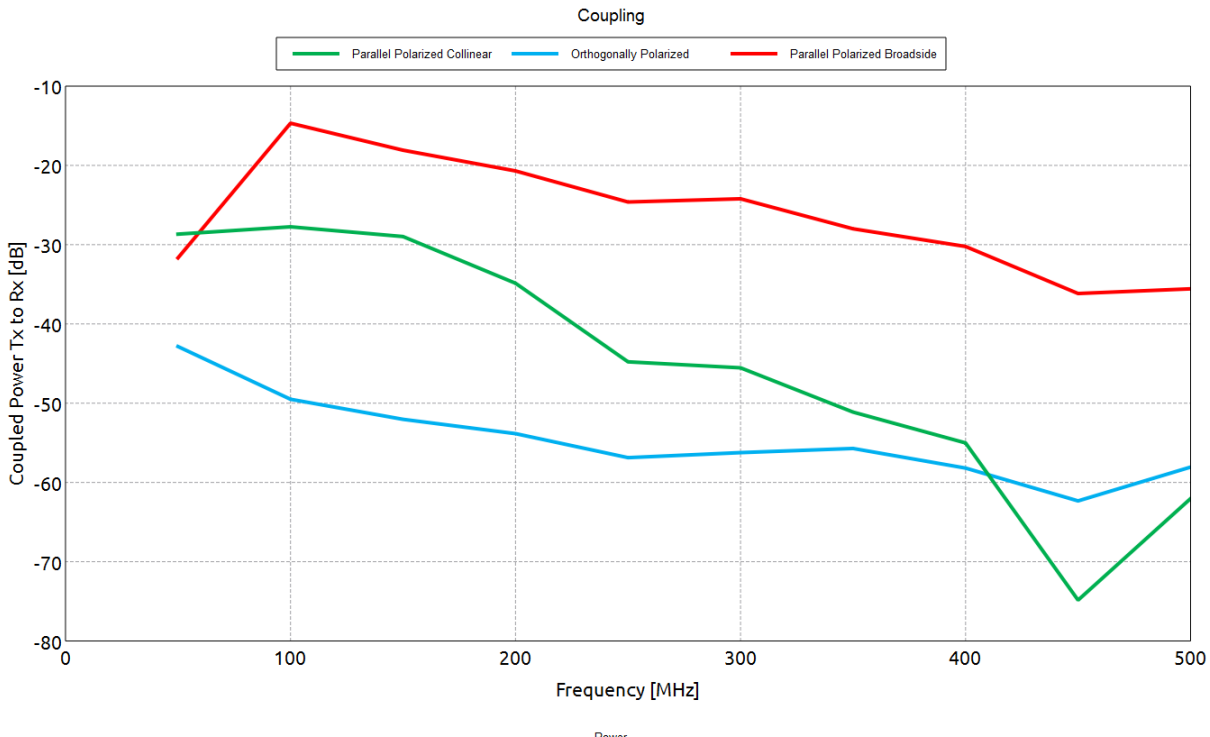
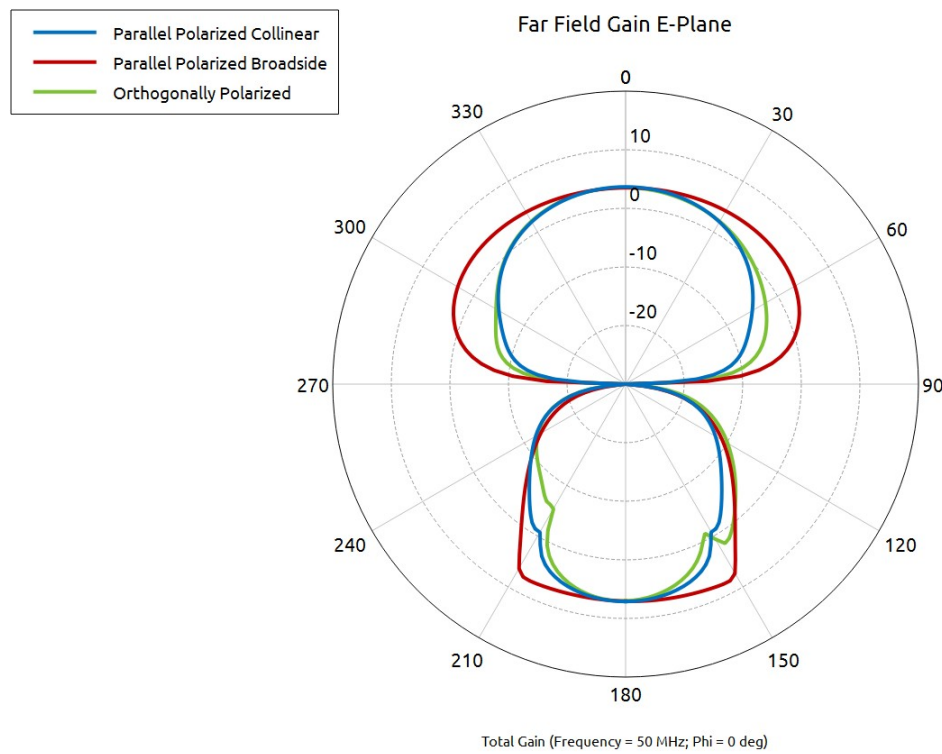
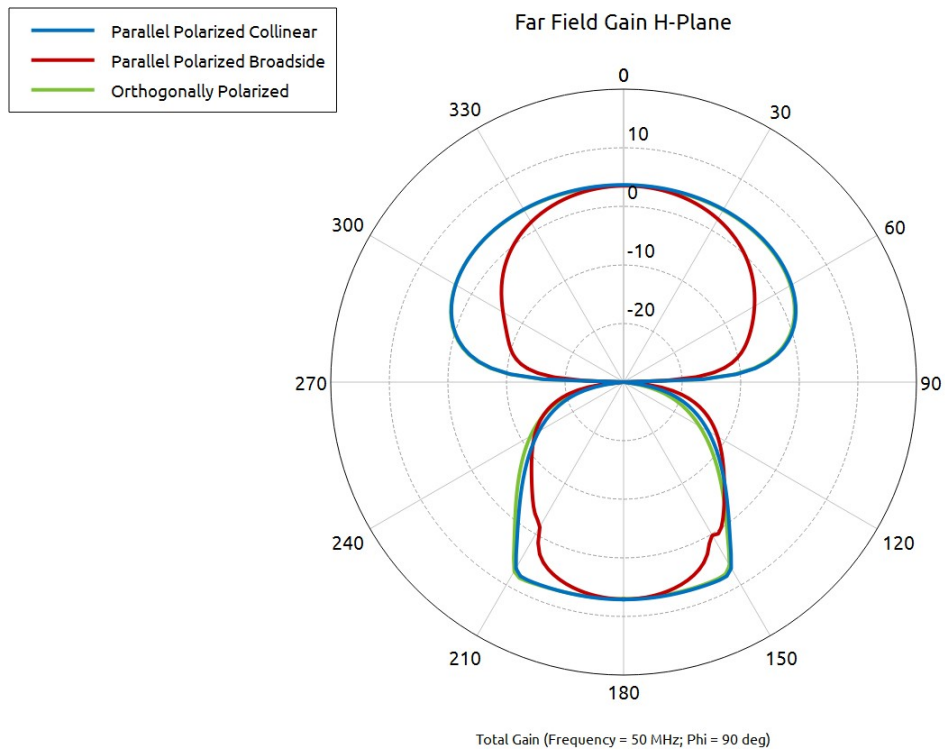


Figure 41: Coupling between Tx and Rx antennas for various orientations of the antenna

In addition to the total coupled power between the antennas, the coupling affects the antenna patterns for the purposes of both receive and transmit. The pattern perturbation effect of coupling was computed for a high-conductivity case as this is something of a worst-case scenario. A frequency series of the effect is presented in the following figures.



*Figure 42: Antenna pattern perturbation (E-Plane) from Tx/Rx coupling at 50 MHz*



*Figure 43: Antenna pattern perturbation (H-Plane) from Tx/Rx coupling at 50 MHz*

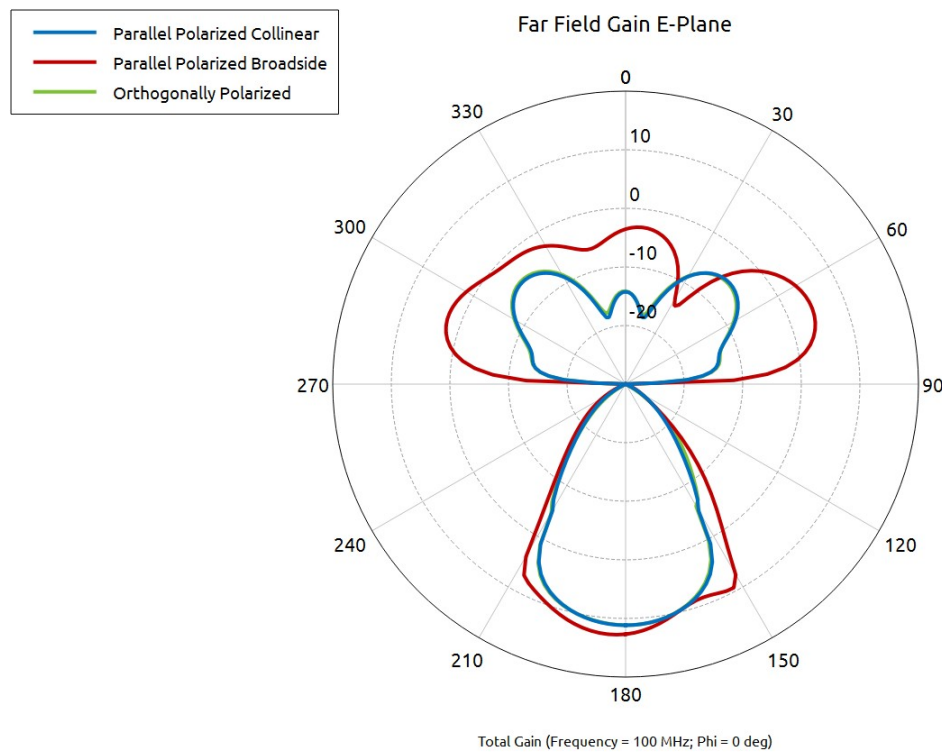


*Figure 44: Antenna pattern perturbation (E-Plane) from Tx/Rx coupling at 100 MHz*

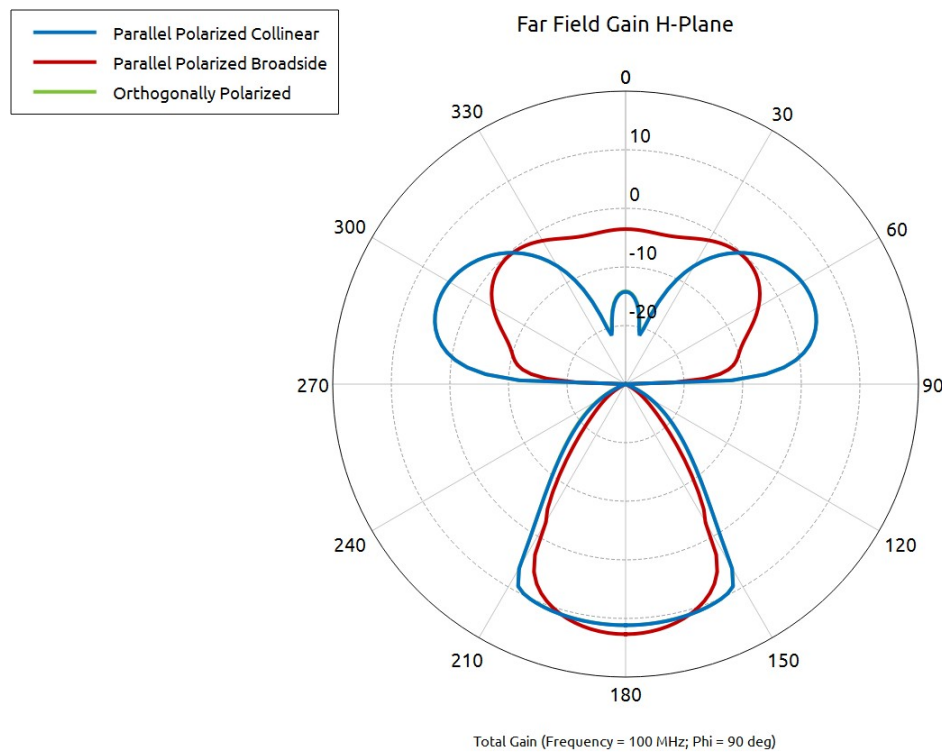


*Figure 45: Antenna pattern perturbation (H-Plane) from Tx/Rx coupling at 100 MHz*

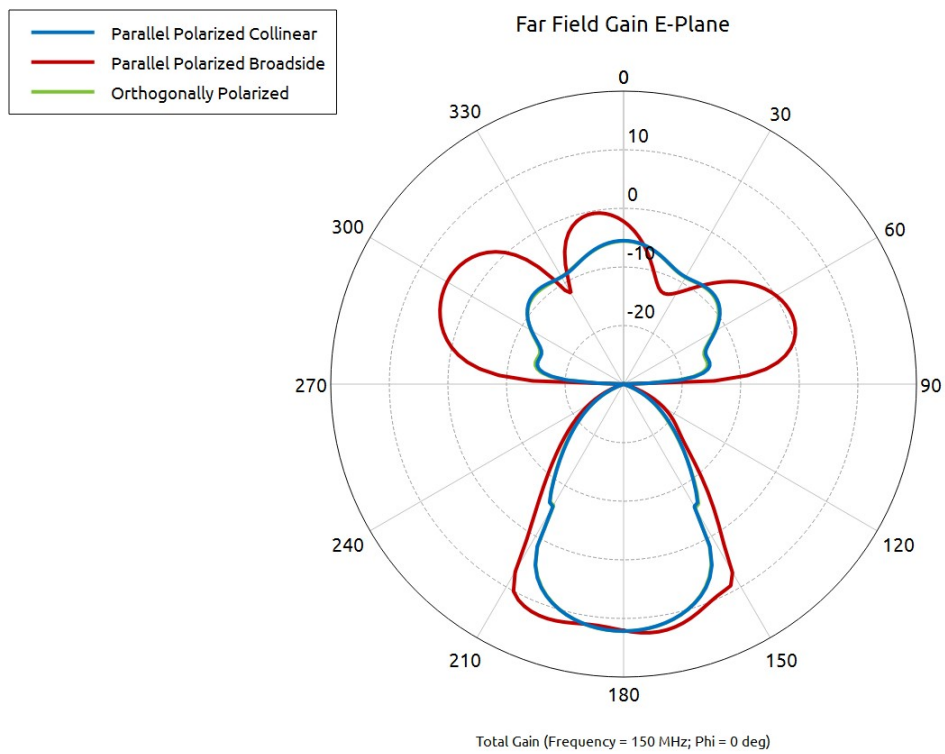


*Figure 46: Antenna pattern perturbation (E-Plane) from Tx/Rx coupling at 150 MHz*

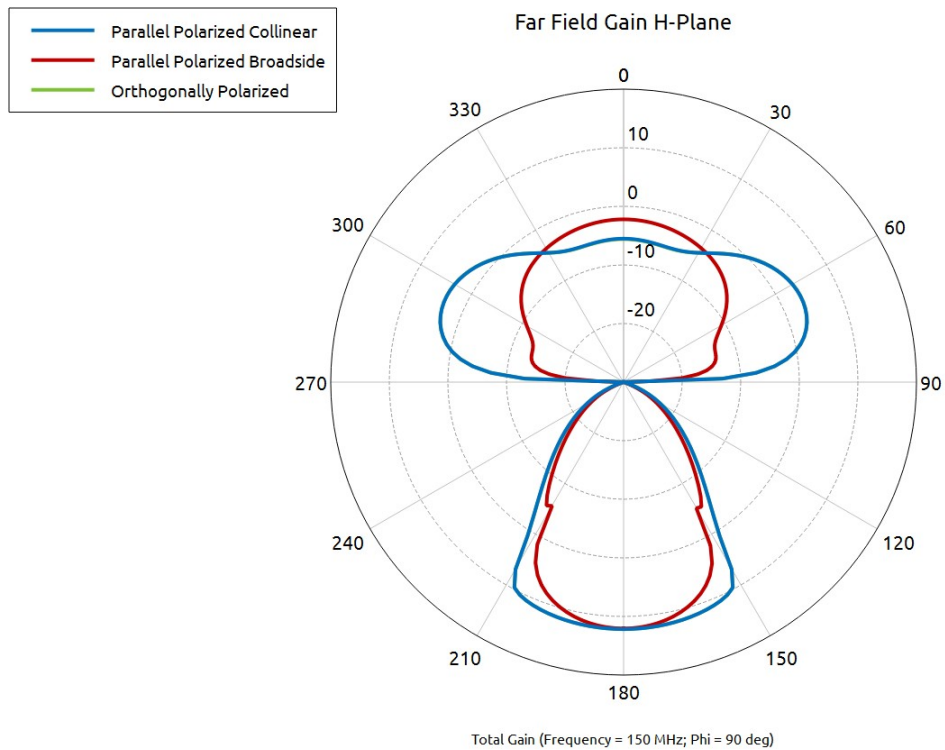


*Figure 47: Antenna pattern perturbation (H-Plane) from Tx/Rx coupling at 150 MHz*

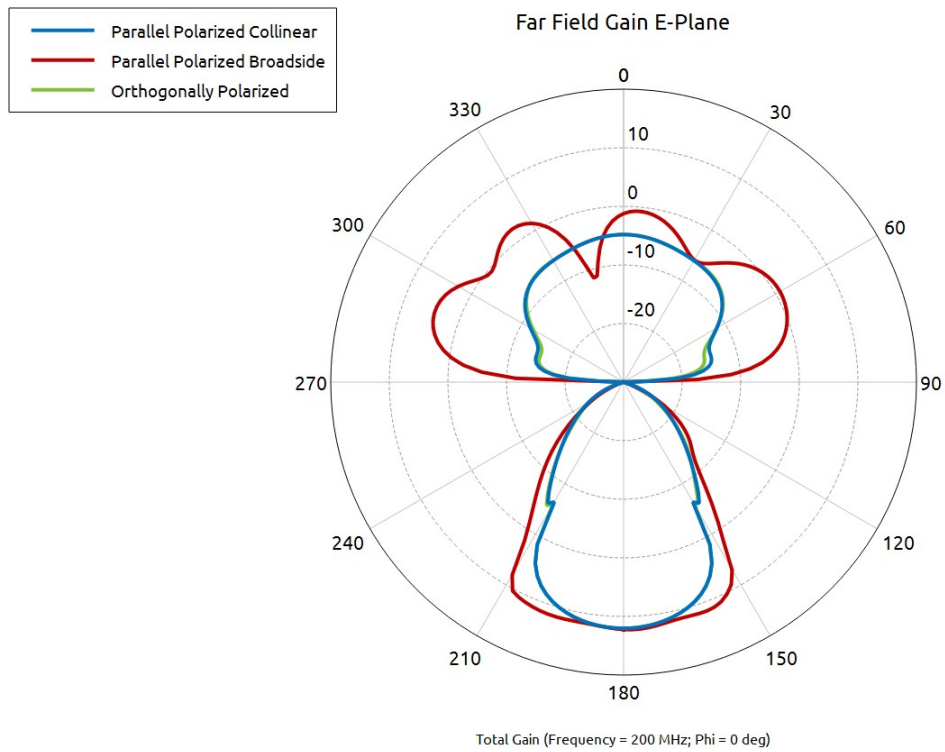


*Figure 48: Antenna pattern perturbation (E-Plane) from Tx/Rx coupling at 200 MHz*

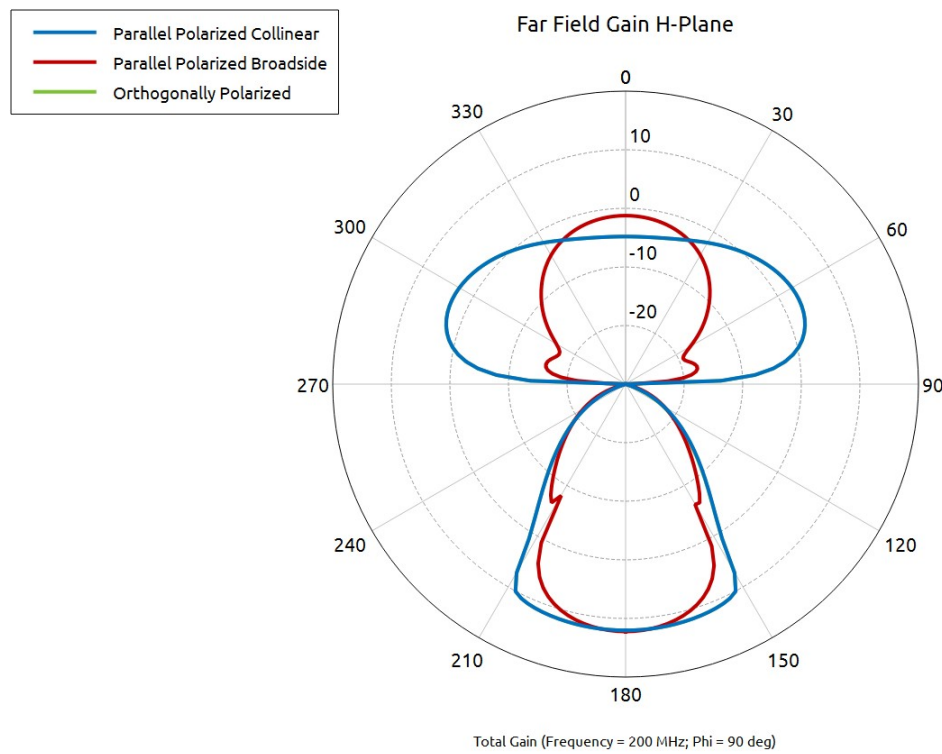


*Figure 49: Antenna pattern perturbation (H-Plane) from Tx/Rx coupling at 200 MHz*

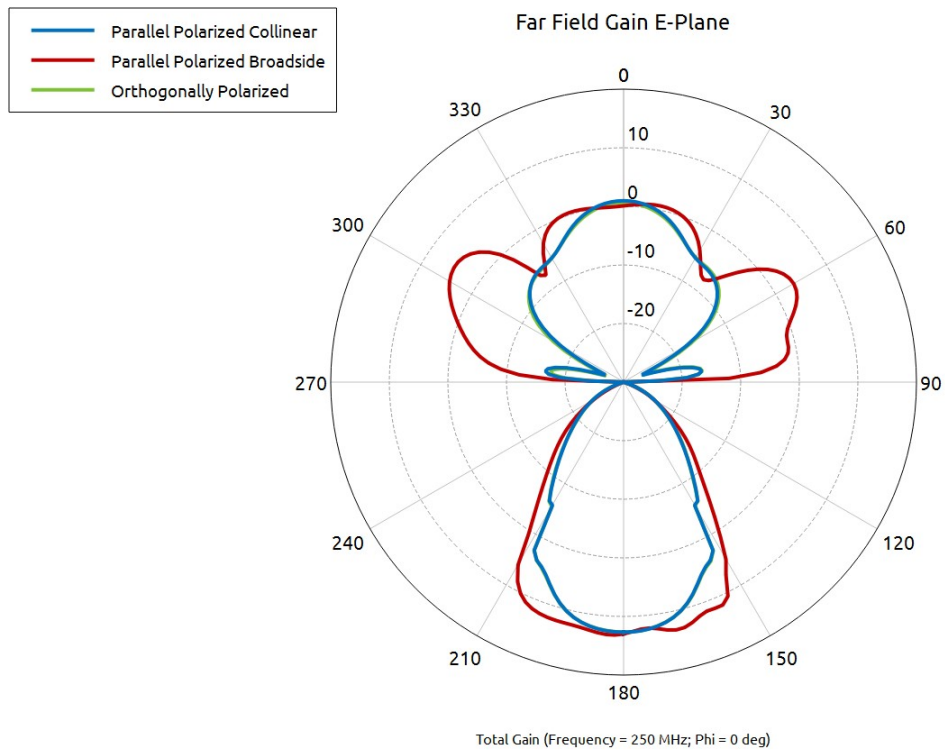


*Figure 50: Antenna pattern perturbation (E-Plane) from Tx/Rx coupling at 250 MHz*

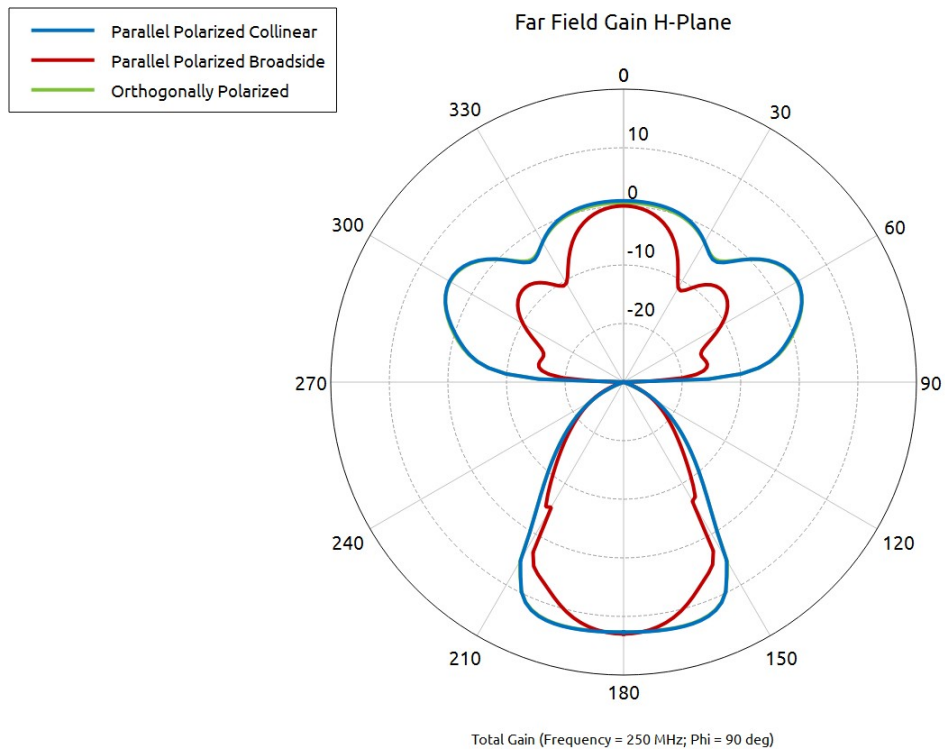


*Figure 51: Antenna pattern perturbation (H-Plane) from Tx/Rx coupling at 250 MHz*

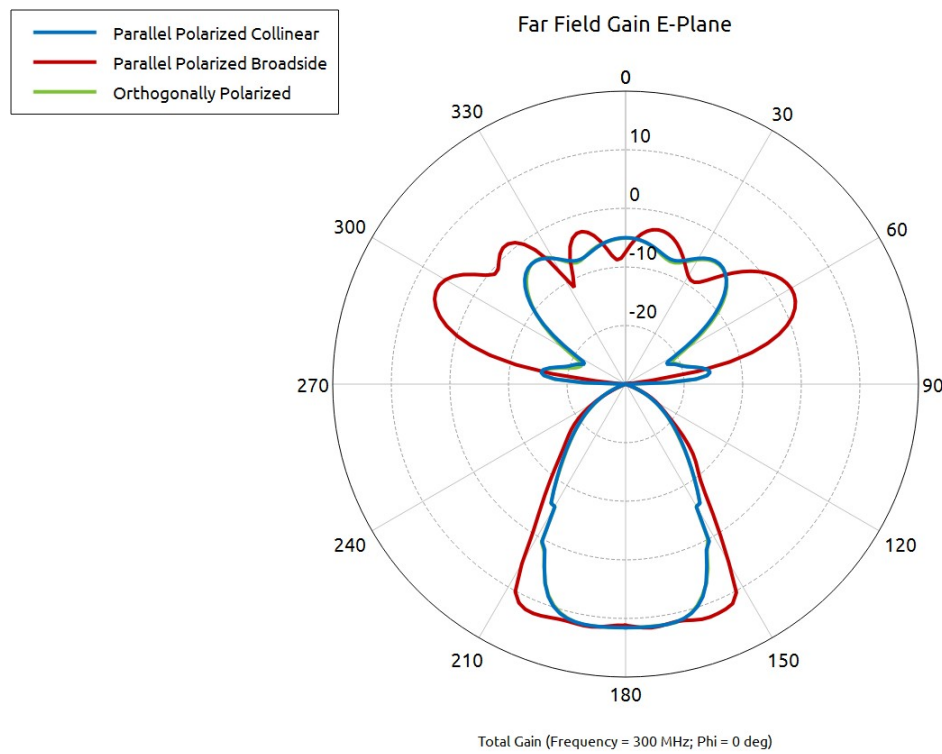


*Figure 52: Antenna pattern perturbation (E-Plane) from Tx/Rx coupling at 300 MHz*

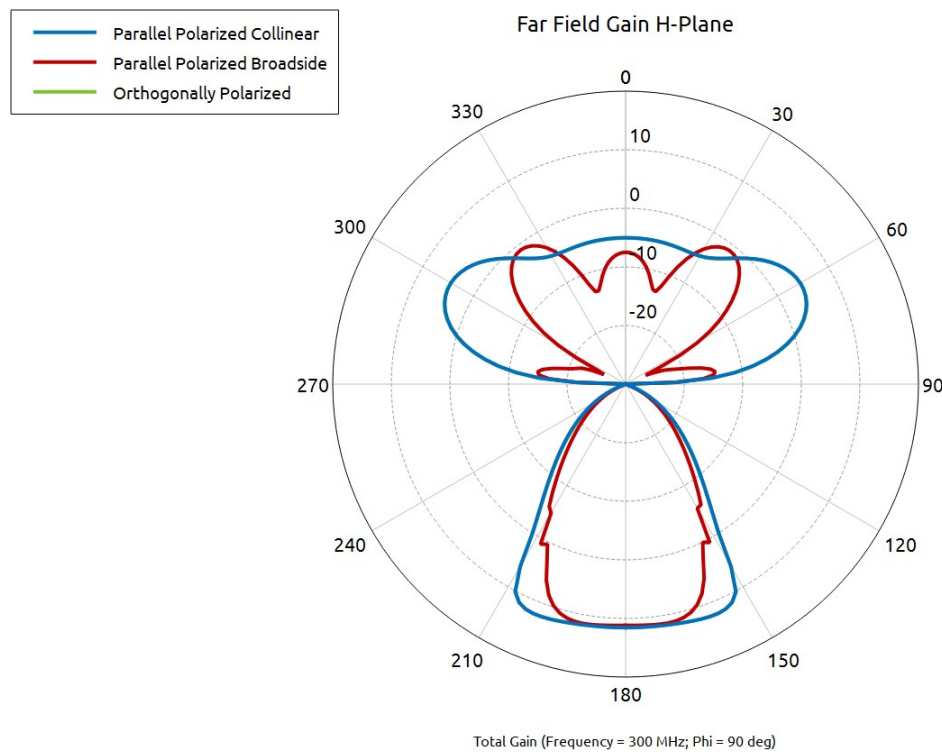


*Figure 53: Antenna pattern perturbation (H-Plane) from Tx/Rx coupling at 300 MHz*

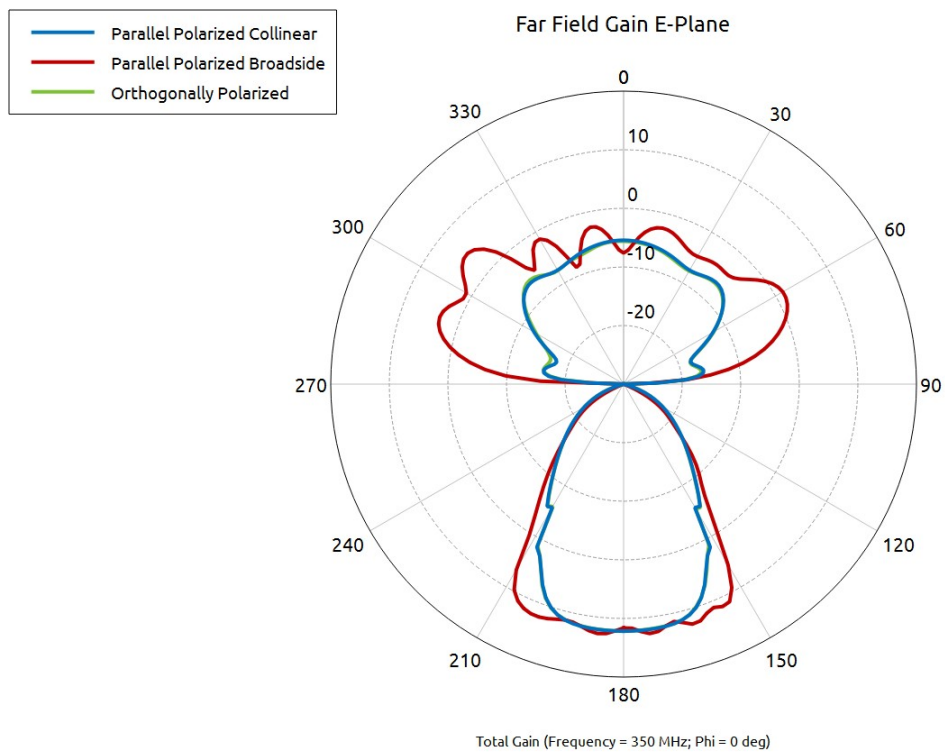


*Figure 54: Antenna pattern perturbation (E-Plane) from Tx/Rx coupling at 350 MHz*

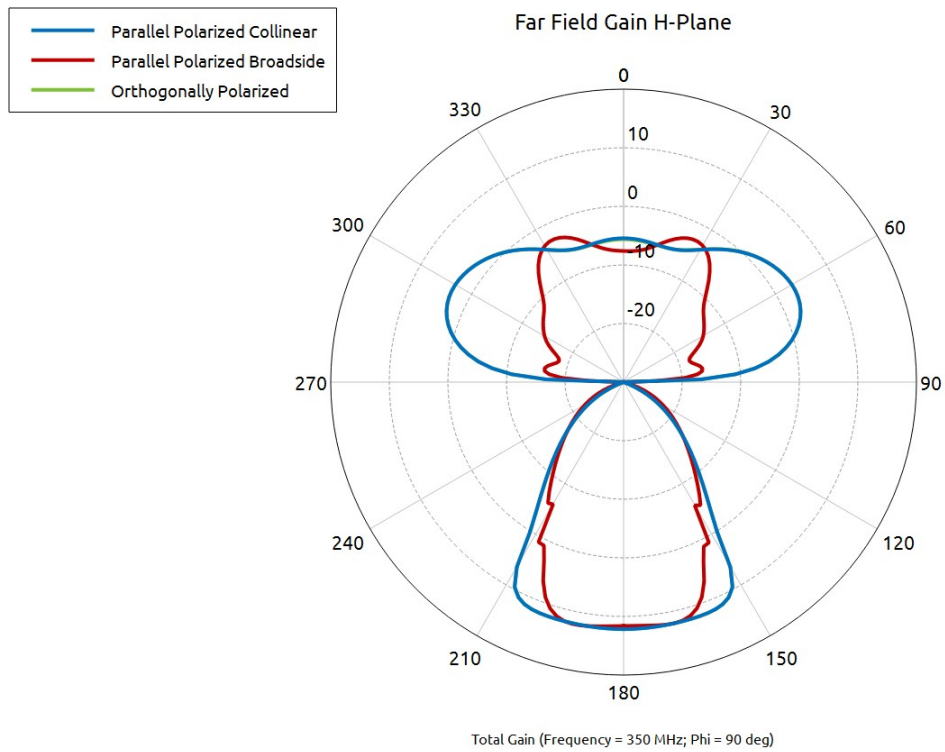


*Figure 55: Antenna pattern perturbation (H-Plane) from Tx/Rx coupling at 350 MHz*

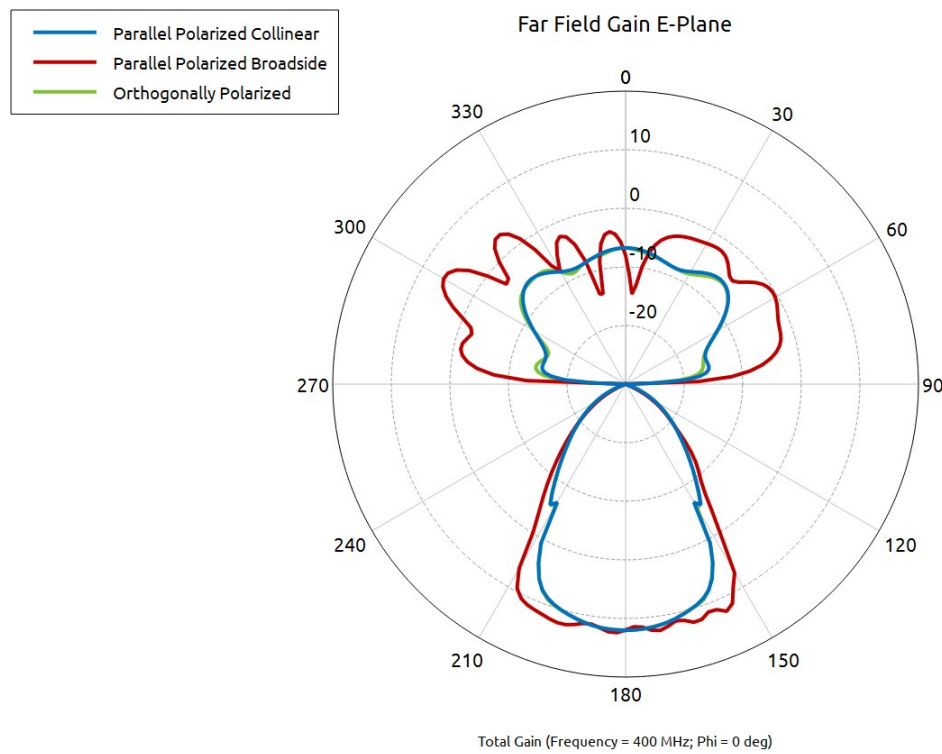


*Figure 56: Antenna pattern perturbation (E-Plane) from Tx/Rx coupling at 400 MHz*

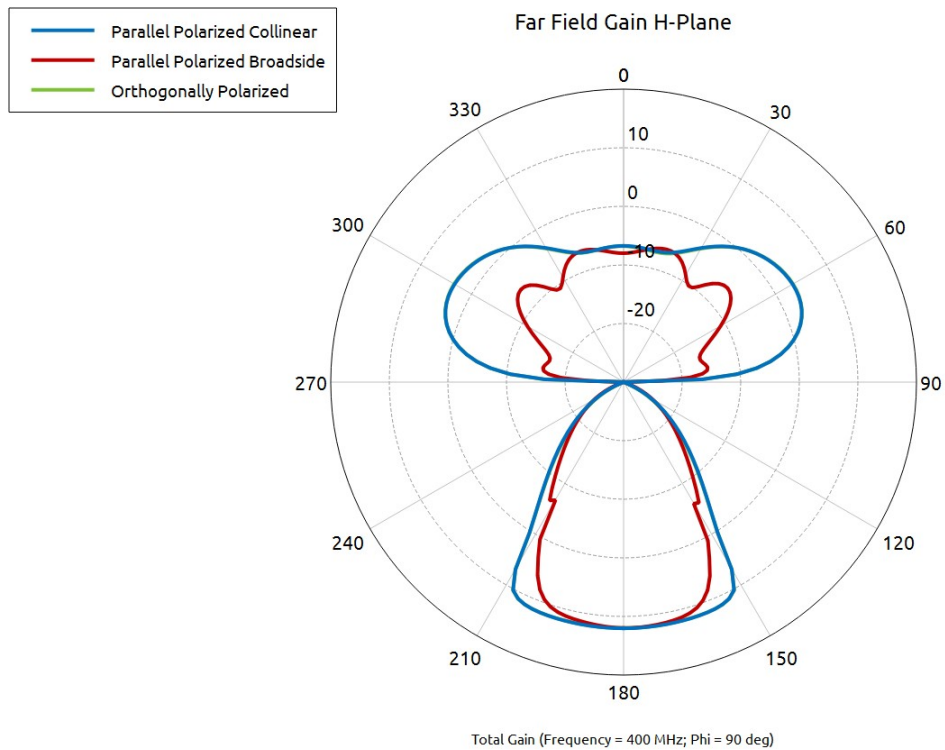


*Figure 57: Antenna pattern perturbation (H-Plane) from Tx/Rx coupling at 400 MHz*

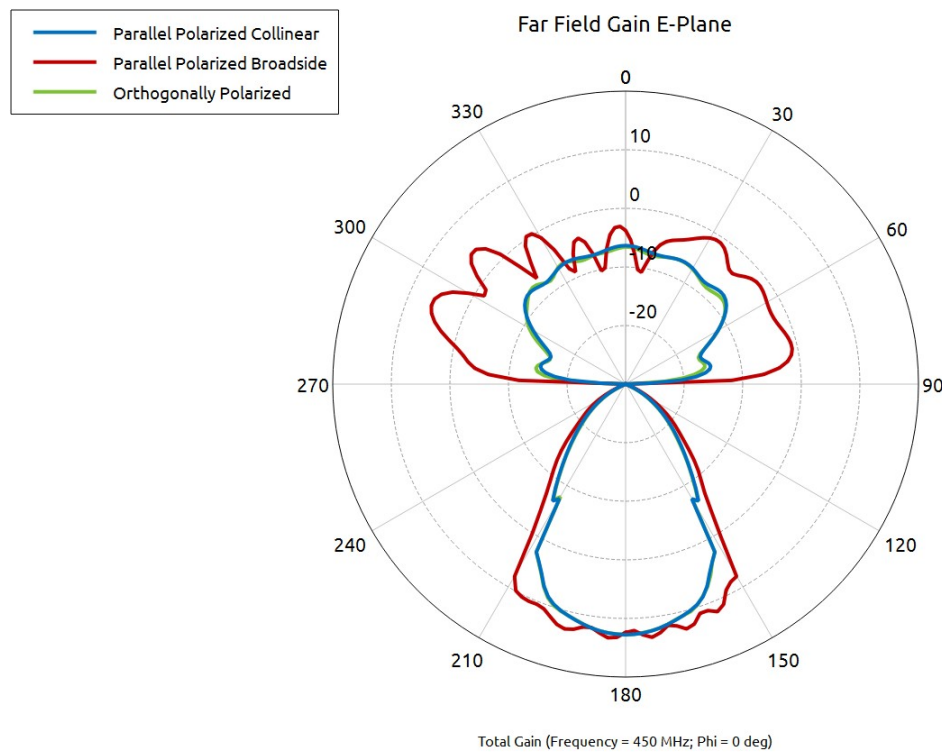


*Figure 58: Antenna pattern perturbation (E-Plane) from Tx/Rx coupling at 450 MHz*

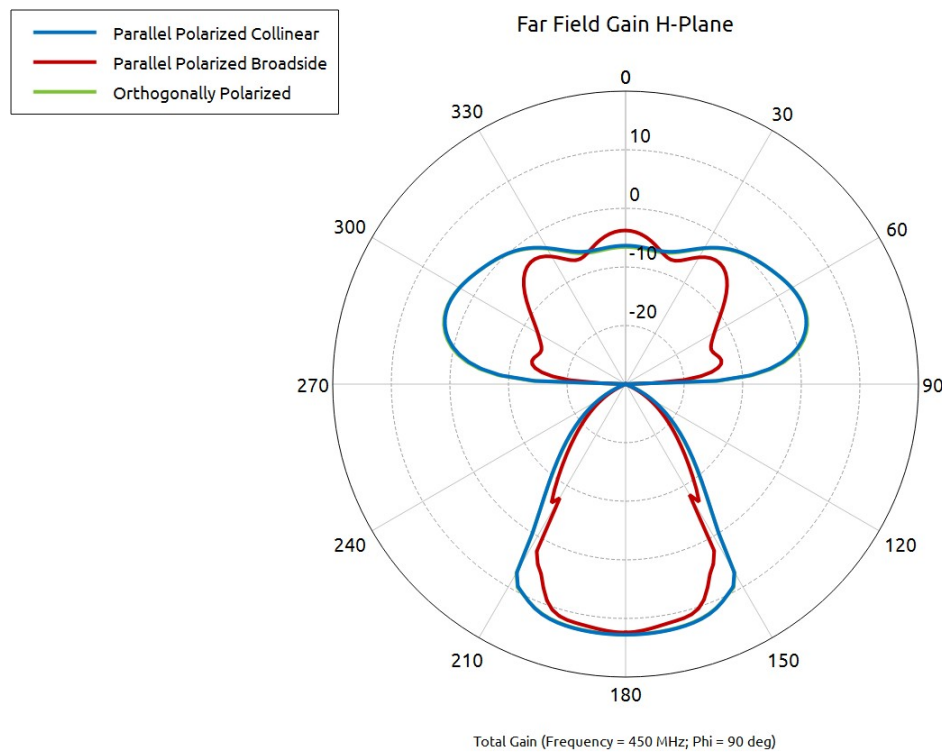


*Figure 59: Antenna pattern perturbation (H-Plane) from Tx/Rx coupling at 450 MHz*

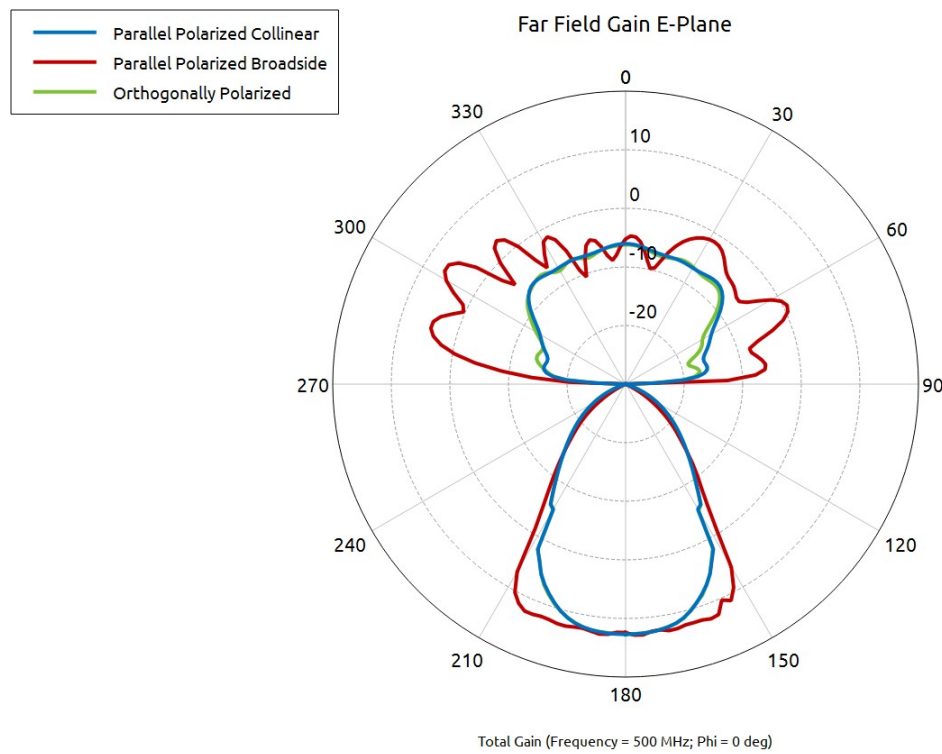


*Figure 60: Antenna pattern perturbation (E-Plane) from Tx/Rx coupling at 500 MHz*

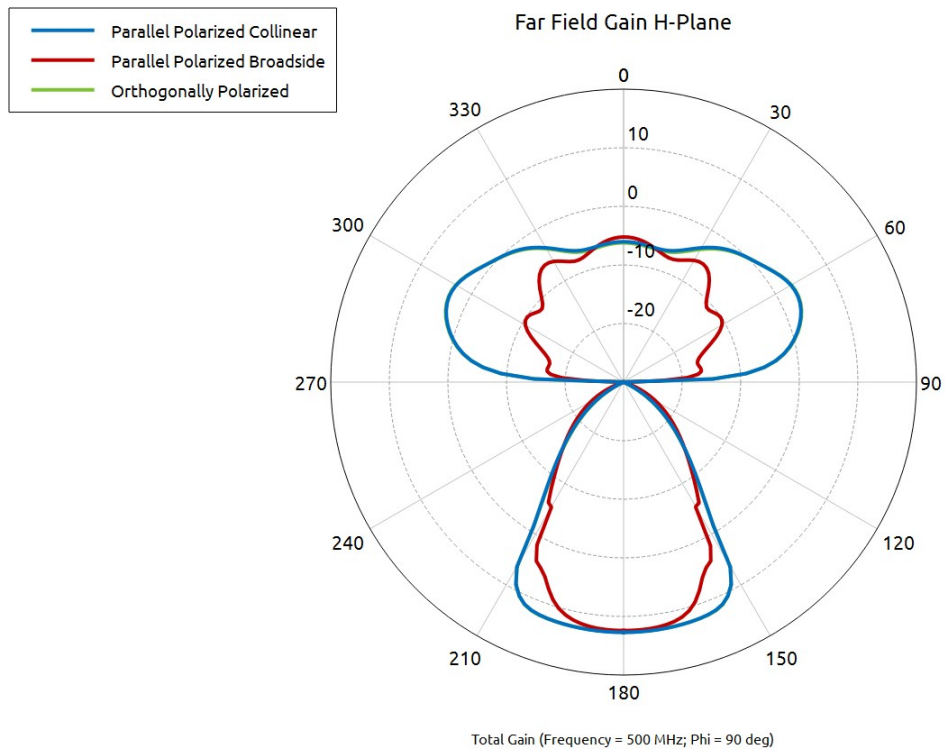


*Figure 61: Antenna pattern perturbation (H-Plane) from Tx/Rx coupling at 500 MHz*

## 4.5 Loading of Ice in the Near Field

The modeling of the antennas, both for the purposes of far-field radiation patterns and coupling between transmit and receive antennas, made use of approximations for upper layer snow, assumed to be 1 meter, and firn, assumed to be 10 meters, and the ice. The different dielectric modeling mechanisms discussed in Section 2.3.1: *Electric Permittivity* were all simulated using FEKO. The Cole–Cole approximations produced the fewest modeling errors and gave results virtually indistinguishable from other relaxation modeling mechanisms in the media. See Section 2.3: *Electromagnetic Properties of Ice and Snow* for more background on the modeling of snow as a loading dielectric.

The model of the antenna, assuming the configuration of the transmit and receive antennas are positioned such that their polarizations are parallel (sharing the E-Plane) and with the elements collinear, was configured to test sweep differing cases of the loading effect of the snow. The greatest changes were observed in the far-field gain when the conductivity of the lower firn and ice layers were changed. The snow and firn were modeled as a multi-layered dielectric substrate — using the Green's function for layered dielectric media — with the ice making up an infinitely-thick dielectric half-space below the firn. This infinite half-space approximation allows model simplification and results in no practical errors in far-field gain since any reasonable ice thickness is well beyond the far-field transition.

The model was run for various values of conductivity and permittivity. The conductivity effect dominates. Models with both high and low levels of conductivity and was run as a set of frequency plots, which are shown in the figures below, to show the variation of far-field pattern and gain across the antenna bandwidth. The high conductivity series was run with an ice conductivity of  $10^{-3}$  S/m and the low conductivity series was run with a conductivity of  $10^{-5}$  S/m. Relative permittivity was fixed at 4.0 to allow comparison strictly on the basis of the more dominant conductivity effects.

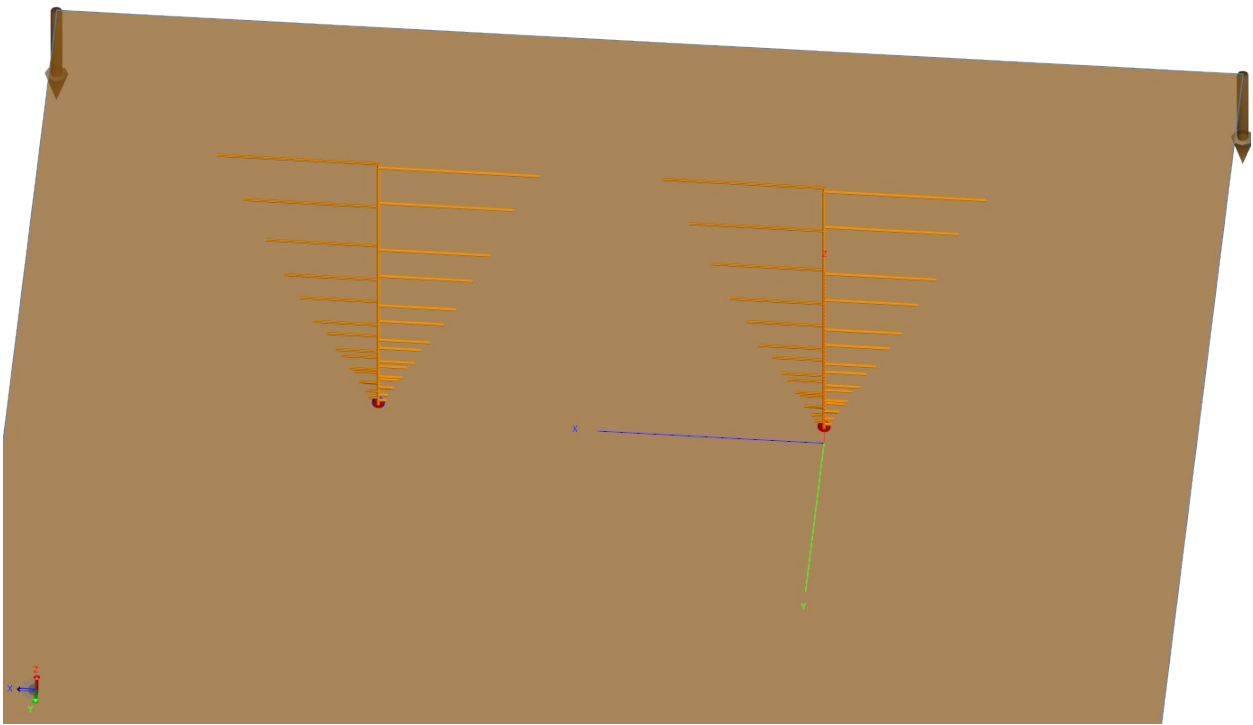


Figure 62: Antenna orientation for modeling of media effect frequency series

## 4.6 Antenna Phase Center

A requirement for accurate estimation of absolute ice thickness by means of the IFT of frequency data points is that the phases of the frequency samples all originate from the same reference point in space. In practice, this will not be the case. The phase center — the point that is the effective origin from which the antenna radiation emanates — is not constant with frequency in the log-periodic type antenna selected for this research. This is illustrated schematically in *Figure 63*. Further, the phase center moves with respect to near-field loading of the antenna by dielectric materials such as the snow and firn near the surface. The antenna must be modeled with the exact mounting arrangement and details of the height above snow to determine the exact phase center position with respect to frequency. The higher frequency responses tend to shift more when moved closer to the snow than the lower frequency responses.

A correction can be applied to the frequency-domain data phase values before the inverse transform is taken wherein an appropriate phase correction corresponding to the two-way change in returned phase is added to the received phase. The phase correction is equal to the change in phase center from the nominal phase center for that frequency. The nominal phase center is typically taken to be the forward-most point on the log-periodic boom or the RF feedpoint where the coaxial cable is attached.

Exact numerical models for the phase center position versus frequency were not computed as a part of this thesis. There is also no practical closed-form solution for finding the phase centers of a log-periodic antenna since the position is extremely sensitive to the geometry of construction. The typical simplifications that permit closed-form antenna analysis — infinitesimally thin wires, infinite conductivity, negligible coupling between boom halves — would render a phase center position calculation meaningless. Further, the phase center position has a slight dependency on the position of the antenna above snow.

Phase center can be modeled numerically using full-wave simulation given an electromagnetic model of sufficient fidelity. Alternatively, the antenna system can be field tested against a known standard broadband antenna with coincident phase center across the frequency band of interest or by using a series of narrowband dipoles with known phase center to determine the approximate phase center distribution versus frequency. Those measurement technique, are remarkably similar to the phase difference technique which is the topic of this thesis.

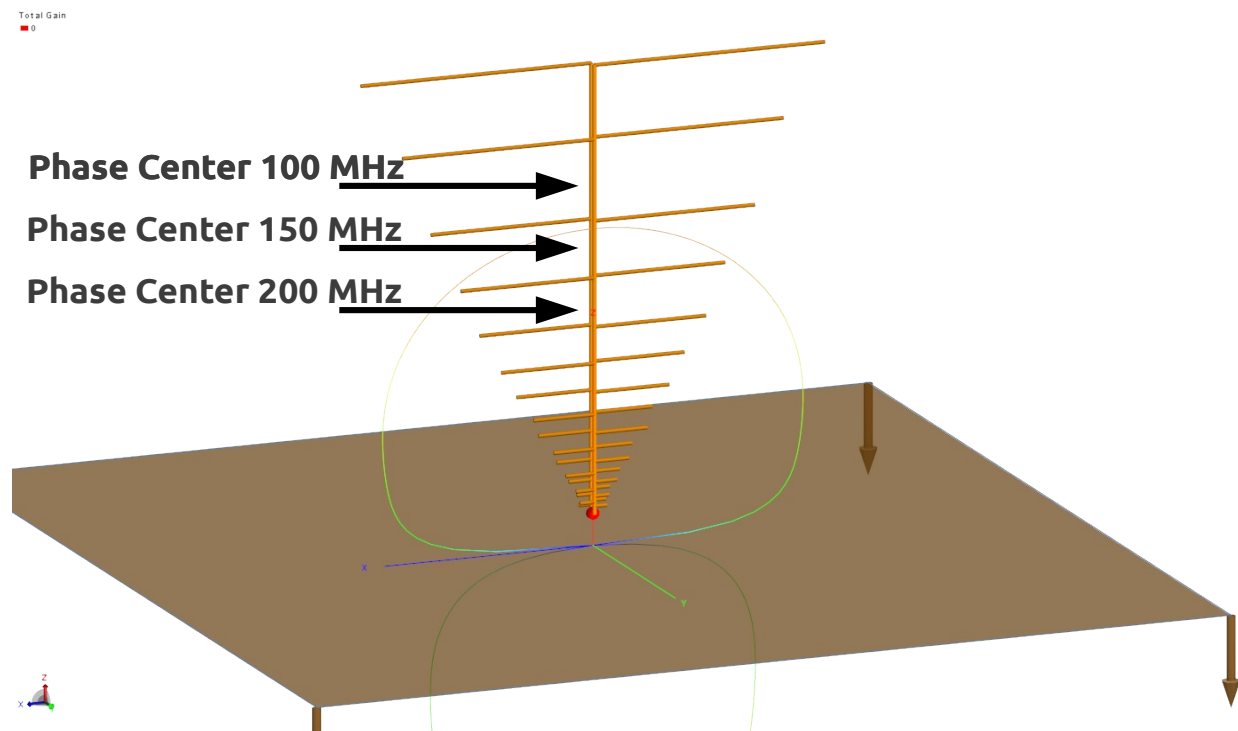


*Figure 63: Log-Periodic antenna phase center distribution*

As an example of this correction, assume that the end-fire direction of the antenna is located in the negative Z direction — nadir — and that the boom of the antenna is located along the Z axis with the principal polarization plane of the antenna normal to the Z axis. If the nominal phase center for the

antenna is at  $Z = Z_0$ , a position that can be chosen arbitrarily, the phase center for a frequency  $f$  is located at  $Z = Z_f$ , and the antenna is completely located in air. A correction should be applied and is given by

$$\varphi_{pc} = \frac{720 f (Z_0 - Z_f)}{C} \quad (4.19)$$

which is simply the fraction of a wavelength in air that the two-way phase correction requires. The phase correction angle formula is given in units of degrees.

## CHAPTER 5: VNA DESIGN IMPLEMENTATION

In this chapter, the design of the VNA is presented with motivations for circuit design and component selection. Simulation of circuit subsections has been completed. Bench testing of some subsystem components has been completed in a laboratory setting. The full VNA unit has not yet been fabricated for laboratory testing. Guidelines for future testing and design revision are presented. The first section of this document presents an overview of the system architecture and an evaluation of the published design in [Baier, 2007] and then in [Baier, 2009c] which inspired this work. Some of the work of Baier in [Baier, 2007] is based on original hobbyist VNA designs by P. Kiciak [Kiciak, 2003] and by the Tuscon Amateur Packet Radio (TAPR) group [TAPR, 2013].

### 5.1 VNA Architecture Overview

The background for the general architecture of a VNA is discussed in more detail in Section 3.3: *VNA System Block Diagram* of this thesis. The specific implementation proposed for the hobbyist VNA that inspired this work, published in [Baier, 2007] and [Baier, 2009c] is given in *Figure 64*. The block diagram for the work of this thesis is given in *Figure 65*.

#### 5.1.1 Published Low-Cost VNA Architectures

The work of this thesis is inspired by the design for a hobbyist VNA with limited technical performance but very low cost which was published in [Baier, 2007] and refined in subsequent publications. The original design is for a T/R VNA that uses a single local reference source to drive two DDS frequency synthesis chips that generate the RF stimulus signal and the LO for recovery of the reference, reflection, and transmission components, the latter from Port 2. The digitization, rather than being implemented with

discrete A/D devices, was completed with the use of a PC sound card. As the sound card has only two simultaneously sampling channels, the device must switch between transmission and reflection channels on one sound card channel and the reference signal on the other. All data processing is done in the PC.

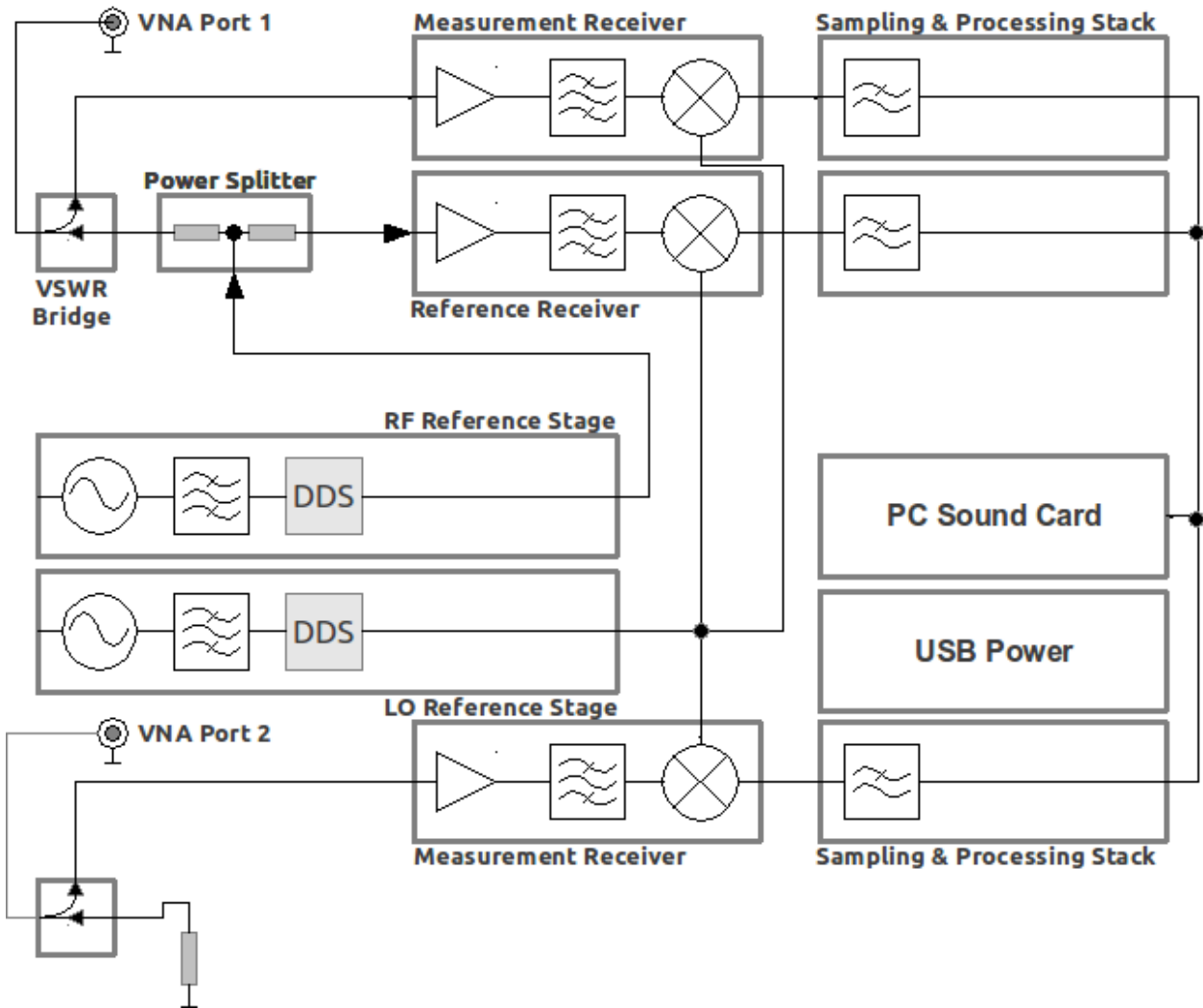
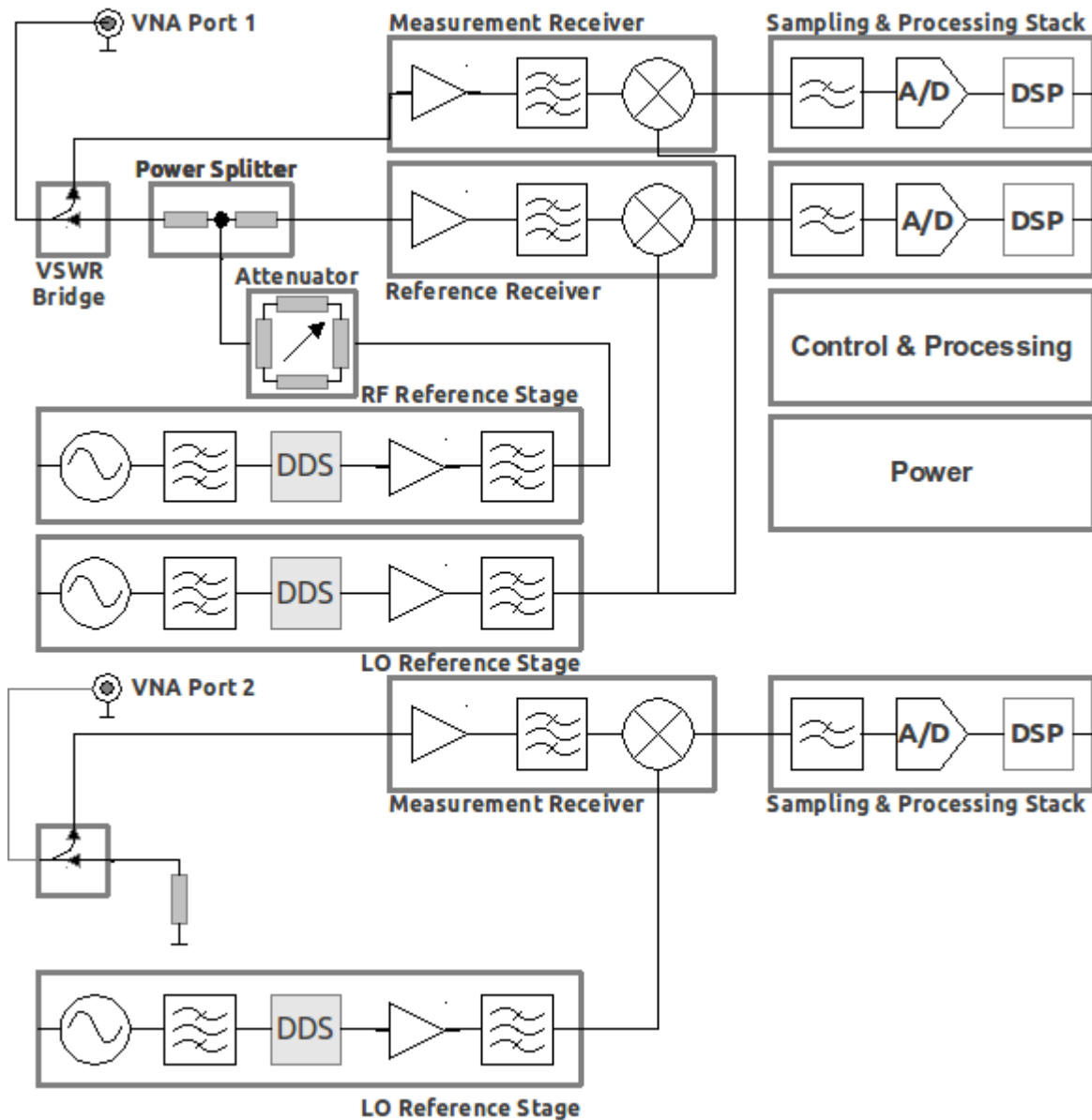


Figure 64: VNA block diagram proposed by Baier



*Figure 65: Block diagram for VNA design with independent A/D and local DSP*

Other published designs, which operate at lower frequencies, make use of an Analog Devices IC that features a fully integrated magnitude and phase comparator, which forms a “VNA On Chip” but suffers from very limited dynamic range — less than 60 dB — due to the limited response of the integrated log-

magnitude power detector and the less than 1 degree phase comparison accuracy even for phase differences near the zero-crossing. For a discussion of the importance of the phase reference plane, see Section 2.5.4: *Phase Measurement Reference Selection*.

The design of this thesis builds on the previously published work but optimizes performance in several key ways. The published hobbyist designs emphasize wide bandwidth, versatility, and the functionality of the data display. The work of this thesis does not require extremely wide bandwidths or extravagant software functionality but instead requires increased dynamic range and phase accuracy to accomplish the relative ice thickness measurements that are, in the end, the scientific goal of this research. By trading away the unnecessary functionality of the hobbyist designs for improved performance in other aspects, the low-cost architecture can be made suitable for this research. The following sections discuss the specific implementation of the VNA and how the design deviates from the published hobbyist VNA designs. The block diagram for the improved system is shown in *Figure 65*.

## 5.2 Base Reference Oscillator

The base reference oscillator used in the existing published work is a 10-to-12-MHz quartz crystal XO, depending on which publication one consults, operated in a Pierce configuration with the fundamental and first harmonics suppressed. The 3rd harmonic of the oscillator — 30–36 MHz — is used to drive the input to the DDS, which implements internal PLL multipliers to drive its system core clock frequency. The general layout of the clock generation signal chain is shown in *Figure 66* and more background information on the clock generation mechanisms is given in Section 3.7: *Core Reference Oscillator* and in *Figure 10*.

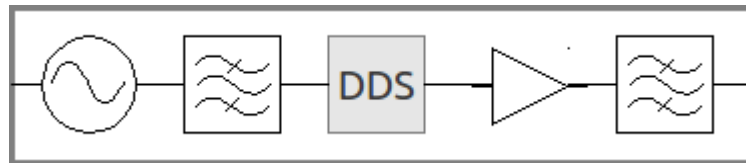


*Figure 66: Clock source signal chain*

The signal chain begins with the common base reference oscillator, which is then low-pass filtered, and drives the DDS IC, which implements the PLL multiplication and digital frequency tuning. The output is then buffered and filtered.

In work completed by [Tim, 2012] an analysis of the existing oscillator was completed and a replacement TCXO was selected. This work was reviewed for its accuracy as a part of this thesis. The accuracy of the oscillator and the implications on the resolution of the system were discussed extensively in Section 3.12: *Signal Chain Accuracy and Calibration*.

Specification	Value
Center Frequency	20 MHz
Temperature Stability	$\pm 0.5$ ppm
Aging Stability	$\pm 1$ ppm/year
Phase Noise	- 80 dBc/Hz @ 10 Hz Offset
Initial Accuracy	$\pm 1$ ppm

*Table 7: Connor-Winfield D53G reference oscillator technical data*

The oscillator chosen in [Tim, 2012] was the Connor-Winfield D53G 20 MHz oscillator 3.3V supply and clipped sine output and valid over temperature range of -30°C to 85°C. The oscillator will remain within the temperature stability specification in that temperature range. Key technical specifications for the oscillator are found in *Table 7*.

For the work of this thesis, further extensive review of available COTS oscillators was completed. For the purposes of oscillator selection, the key criteria to focus on was not initial frequency accuracy of the oscillator but rather the temperature stability and the aging stability. The focus is on eliminating the drift errors with time since the purpose of the radar is to make relative measurements of thickness. Absolute errors in oscillator performance can be tolerated, as can random jitter, which can be averaged out to a great degree with a sufficient number of measurements.

The work of this thesis has selected the AVX/Kyocera KT7050A20000KAW33TAD TCXO which has specifications summarized in *Table 8*. The AVX oscillator operates over a wider voltage range, 2.7 V to 5.5 V, and also produces a clipped sine output. The selected oscillator operates within specification from -40°C to 85°C, again, a wider range. Most importantly, the Kyocera part has significantly lower drift with aging than the oscillator selected in [Tim, 2012] as well as lower phase noise at all offsets, including the important 10-Hz metric. Technical data can be found in [Kyocera, 2013].

Specification	Value
Center Frequency	20 MHz
Temperature Stability	$\pm 0.28$ ppm
Aging Stability	$\pm 0.23$ ppm/year
Phase Noise	-90 dBc/Hz @ 10 Hz Offset
Initial Accuracy	$\pm 0.1$ ppm

Table 8: AVX/Kyocera KT7050A20000KAW33TAD oscillator technical data

### 5.3 Direct Digital Synthesis

In the background discussion of the VNA architecture, Section 3.8: *Frequency Sweep Generation* discussed the RF frequency and sweep generation in general terms. For the work of this thesis, the stimulus sweep and LO references are generated by means of a Direct Digital Synthesis (DDS) IC, which features an integrated PLL to multiply the VNA base reference oscillator to a high reference clock frequency and then digitally divide that reference down to the desired RF stimulus and LO frequencies. The DDS chosen for the published design discussed in this chapter remains the ideal COTS DDS IC to use for this type of design.

The chosen DDS is the Analog Devices AD9859 [ADI, 2009], which is specified to operate on core clock frequencies up to 400 MHz. The core clock frequency for the DDS is the base reference oscillator frequency multiplied by the overall PLL ratio in the digitally programmable PLL implemented inside the DDS. The DDS operates in the temperature ranges expected for this application and is within specifications provided by Analog Devices. The output frequency, however, operates only to 200 MHz using standard Nyquist rate D/A conversion and at frequencies much lower than that in practice. Careful placement of the mix products inside the DDS — the DAC images and spurs — allows use of DDS image and alias frequencies at higher frequency than the typical clock frequencies [Gentile, 2007]. Use of the DAC products requires a thoughtful frequency plan.

### 5.3.1 Spur and Harmonic Products

The DDS output does not produce pure sine products. The output of the DDS will be the desired output frequency set by the frequency tuning word programmed to the DDS,  $f_{tune}$ , and various harmonic, alias, and spur products produced by the DDS DAC. In general the frequencies of the spur products can be found by

$$f_{spurDAC} = m \cdot f_{tune} \pm n \cdot f_{ref} \quad |m \in \mathbb{N}, n \in \mathbb{N} \quad (5.1)$$

where  $f_{tune}$  is the desired output frequency,  $f_{ref}$  is the DDS core clock frequency, which is set by the combination of the base reference oscillator and the internal DDS PLL divide ratios. This means that the products will be present at all mix products  $f_{tune}$  and its harmonics and  $f_{ref}$  and its harmonics.

The spectral products of the DAC images are shown conceptually in *Figure 67*. Notice that the spectral images exhibit a frequency-dependent attenuation, which is mostly attributed to the sinc response, a consequence of the digital-to-analog conversion process of the DAC [Gentile, 2007]. In addition to sinc shaped attenuation distortion of the spectrum of the DDS output, images in the even Nyquist zones are inverted relative to the fundamental signal phase. The 180 degree phase shift spectral inversion has little impact on a purely sinusoidal DAC output waveform. However, the phase shift must be accounted for in the phase detection if even products are used for LO or RF generation. The use of the odd products eliminates this complication.

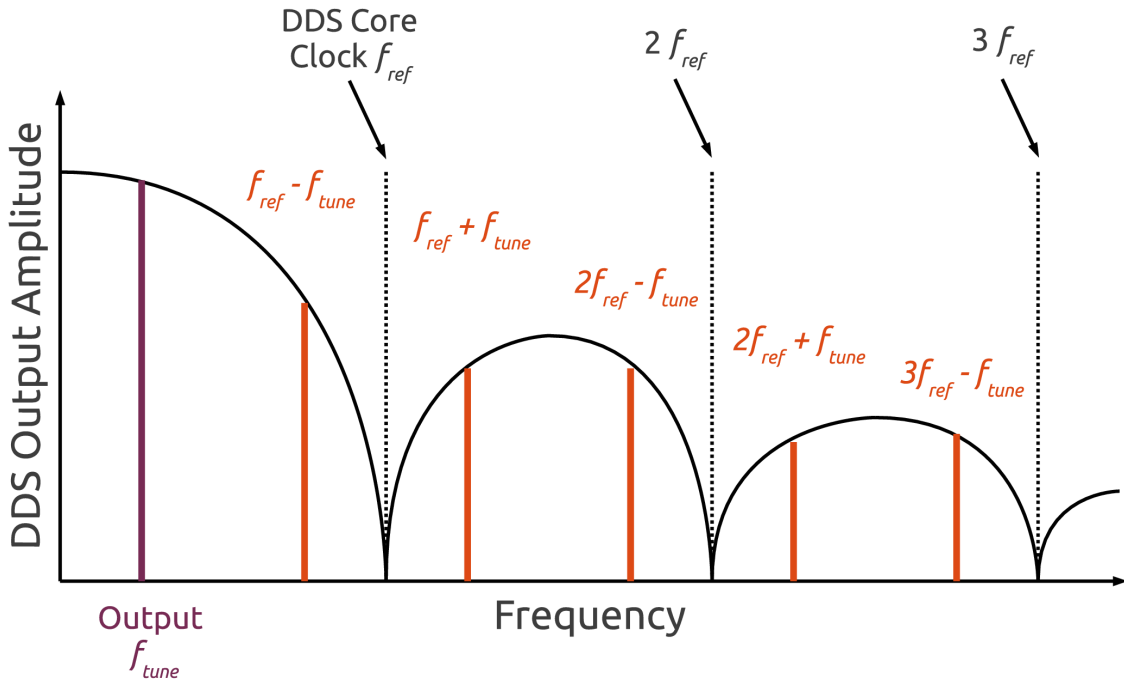


Figure 67: DDS alias, harmonic, and spur products and their output power

The sinc magnitude response of the DDS and the prospect of higher frequency operation using super-Nyquist operation also has implication of the receiver recovery if the RF and LO are operated at the same frequencies or even at the same DDS core clock frequencies. If both the RF stimulus DDS and the LO DDS are operated at the same programmable PLL divider ratio, their system core clocks will be identical and their images will overlap. This can be seen in *Figure 68*, in which the RF stimulus DDS signal is shown in black and the LO DDS spectrum is shown in green, using a lower PLL multiplier.

By effectively choosing the correct offsets between the RF DDS frequency and the LO frequency within the frequency plan, it is possible to place nulls in the LO performance at places where unwanted RF spurs occur or vice-versa. This provides a filter response characteristic to the receivers because the output of the mixer will have zero power at those frequencies. This is illustrated in *Figure 69*, in which the RF stimulus

DDS signal is shown in black and the LO DDS spectrum is shown in green, using a lower PLL multiplier chosen to place the null in the amplitude (power) response of the DDS on top of the highest power undesired RF product. Spur products of the RF DDS are shown in orange. Note that the LO will also produce a spur spectrum, which is not shown.

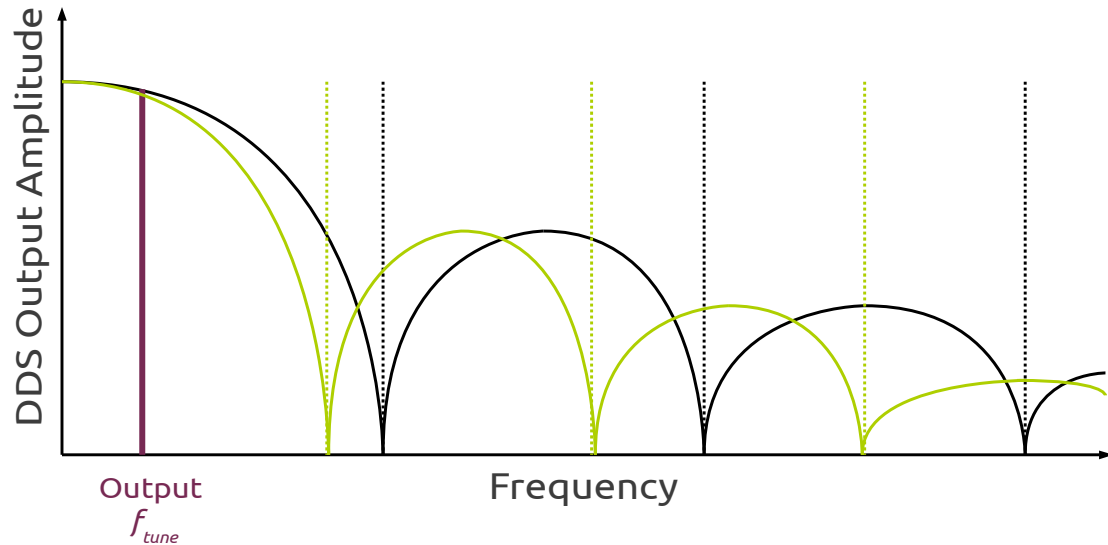


Figure 68: DDS LO and RF DAC image spacings

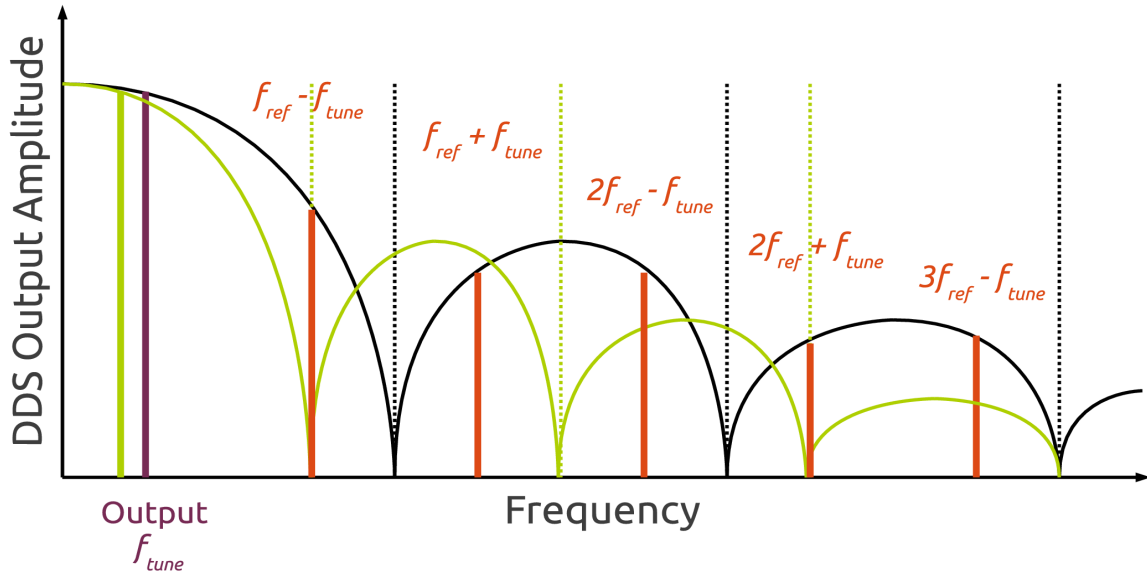


Figure 69: DDS RF and LO spectral product placement to attenuate mix products

### 5.3.2 DDS Phase-Coherence and Synchronization

Care must be taken in the revised design to ensure phase synchronization of the stimulus and local oscillator channels. The multiple DDS chips must be phase-synchronized from the base reference oscillator. This requirement has implications on the physical layout of the board, requiring equal trace length between reference and DDS chips. This can be verified by simulating group delay of the transmission line — microstrip — on the PCB and adjusting until equal phase delay between clock distribution paths is achieved.

Further, synchronization requires that all internal PLLs in the DDS chips, which are clocked to the oscillator but have differing divide ratios, achieve lock simultaneously since the lock detection signal typically resets the phase accumulator of the DDS. Because the DDS chips always operate with differing

divisors to reduce the spur effect, other techniques must be used to account for the variable PLL lock time. Eliminating this effect can be accomplished by asserting the reset line to the DDS after lock is achieved and then by programming the tuning word for all devices to zero [Brandon, 2002]. This sets the phase accumulator phase to zero and prevents the accumulator from incrementing while the PLL clocks. Since all the devices are clocked by a common clock and the PLLs are phase-locked to the base reference oscillator, all system clock signals will be phase coherent [Brandon, 2002].

## 5.4 VSWR Bridge

The VSWR bridge and power splitter design that is used in the VNWA design are shown in *Figure 70*. The design recommendation is that bridge be modified into a fully-balanced configuration with the transformer layout as shown to provide better DC bleed-off when connected to the antennas. The revised configuration is shown in *Figure 71*.

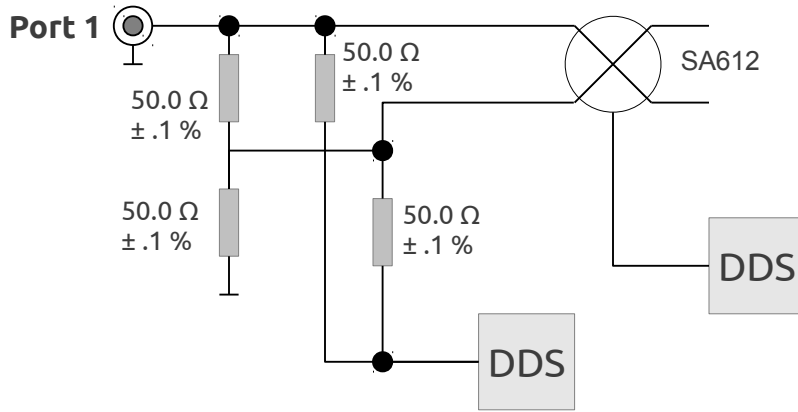


*Figure 70: Standard VSWR bridge with four differential input*

Further improvements can be realized in the VSWR bridge by matching the resistor values to the input impedance of the revised mixer, discussed in the next section, and by using broadband transformer

coupling to implement the balun as shown in *Figure 72*. Further optimization of the bridge values based on simulation of the input impedance of the new receiver mixers will be required.

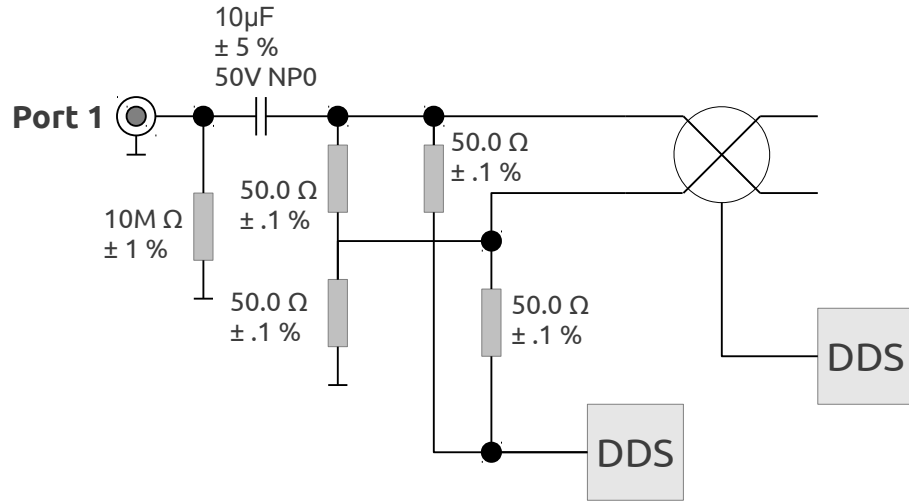


*Figure 71: Improved VSWR bridge with DC blocking and bleed resistor*

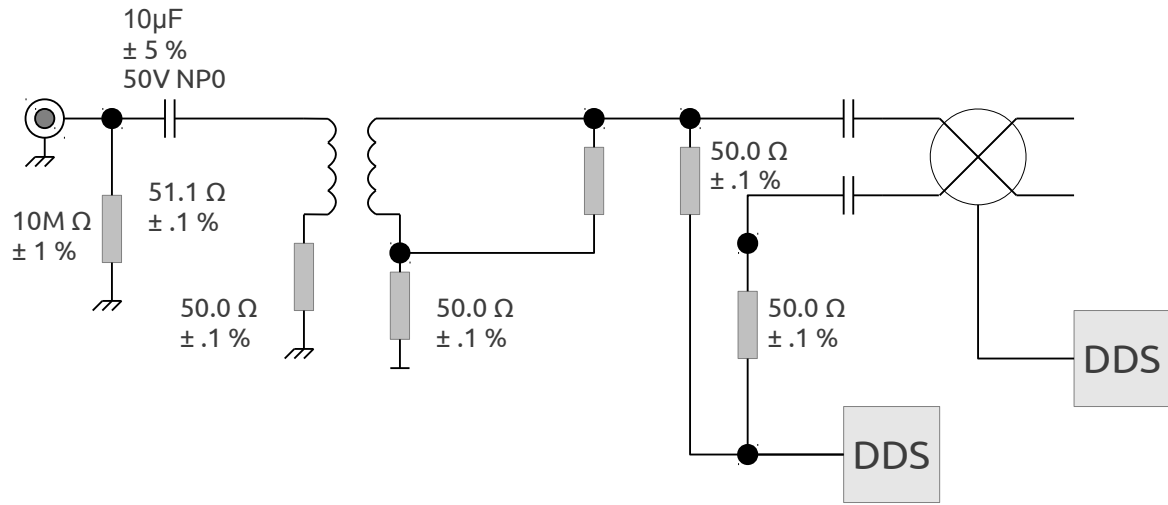


Figure 72: VSWR bridge with broadband transformer for ground isolation

## 5.5 Tuned Receiver

The receiver implementation on the hobbyist VNA that is the basis of this design is implemented using a Gilbert Cell mixer — a differential Cascode pair — part number SA612A. The SA612A is a low-power double-balanced Mixer by NXP (formerly Philips Semiconductor). This part has been obsoleted by the manufacturer and other parts with better performance are available.

The highly integrated configuration of the SA612A does offer some advantages that should be found in any replacement parts for the device in the design. The SA612A includes internal bias-tee circuitry so external bias chokes are not required. The fully-balanced operation permits the balanced output of the VSWR bridge to be taken differentially without the use of DC biasing when operating from sufficiently large voltage rails.

Undesirable features of the existing mixer are that the balanced output of the mixer does require downstream implementation of DC bias-tee for single supply operation of the output buffer amplifiers

that feed the audio CODEC. The SA612A has a very low P1dB (1 dB input power compression point) which would require a significant change to the power splitter implementation that provides the reference signal to maintain linearity if the output power of the RF generator is increased significantly upstream of the splitter.

Replacement mixer parts from Linear Technologies, Hittite Microwave, Minicircuits, Analog Devices, Texas Instruments, NXP, and On Semiconductor were evaluated. Very few suitable parts were found. Applications in this frequency range typically employ highly integrated receivers and so discrete high performance double-balanced mixers working in this lower frequency range are difficult to obtain. Most discrete mixers are used for higher frequency applications and this frequency range is typically covered by fully integrated transceivers.

One part evaluated that would be quite suitable is the On Semiconductor SMA5101. The SMA5101 is a fully-balanced mixer with differential inputs and good performance. The LO-to-IF isolation, while acceptable, is undesirably low.

Two parts evaluated from Analog Devices, the ADL5801 and the AD8343 also would be suitable for this application. The ADL5801 works to 10 MHz and up to 500 MHz and would be suitable for this task, however, the performance of the AD8343 is superior. Analog Devices AD8343 active differential mixer that also suppresses the LO and RF signals at the output to better than 50 dB of isolation despite the fact that AD does not market the device as a true double-balanced mixer. This part would be the optimal choice for the receivers. Data for the AD8343 is found in [ADI, 2013].

## **5.6 Digitization**

If the sound card implementation is changed in the new VNA as is recommended by this thesis, analog to digital conversion will need to be implemented by external A/D. Given the dynamic range that is the requirement of this thesis, a minimum of 16-bit resolution is required. A search of available, production, low-cost, high resolution A/D converters was completed. Several devices were evaluated.

The device selected after examination of the parametric search including multiple vendors was the AD7610, which features conversion rates of 250 kSPS, an effective SNR of better than 94 dB, SPI or parallel interfaces, and internal sample/hold buffers. The most negative attribute of this choice is cost. This would be the most costly component in the design BOM.

A further possibility for future work is the implementation of direct digital-downconversion using an FPGA implementation and sub-Nyquist bandpass sampling along with suitable analog filter. This method takes advantage of the fact that signals samples at less than twice the rate of their frequency will alias and be indistinguishable from integer multiples of that frequency. By using bandpass filtering to guarantee that signal falls within a particular integer multiple of the sampled band, the entire signal can be reconstructed.

## **5.7 Miscellaneous Component Selection**

This section provides miscellaneous notes on construction and design recommendations for the VNA implementation. Topics discussed include the selection of passive components that have very good stability over a temperature swing to facilitate overall frequency and phase stability of the VNA.

### **5.7.1 RF Signal Capacitors**

All filter capacitors in the VNA in the RF patch should be realized using surface mount Multilayer Ceramic Chip capacitors (MLCC). MLCCs, due to their box-end terminations, exhibit practically no parasitic lead inductance, which would introduce extra stray impedance at the higher end of frequencies seen in this particular radar design.

All MLCCs used in the VNA design in the signal path should be of the lowest possible temperature coefficient and use, at a minimum, Class 1B dielectrics such as the NP0 capacitors (EIA code C0G). NP0 MLCCs have a dielectric that exhibits practically zero drift with temperature, which will provide better temperature stability over the operating range of the VNA. The recommended part family used is AVX (Kyocera) 08055A or 06035A series, which both meet the full temperature range for this design.

Capacitors in the design within the power rails or used for power supply decoupling in the digital electronics domain can be of the lower quality X7R type dielectric, which is more cost effective and offers a higher bulk capacitance. X7R is the only Class 2B capacitor type that meets the full temperature range requirement for the system. The recommended part family for power and decoupling is AVX (Kyocera) 08055C or 12065A series, which both meet the full temperature range for this design. In no instance should Y5V type capacitors or any non-ceramic capacitors be used in this design.

### **5.7.2 Inductors**

The inductors in the signal path used to implement the filters and bias-tees should be of surface mount type, high-Q, and with high temperature stability. This implies that surface mount, wire-wound inductors with air or ceramic chip cores should be used. Ferrite core magnetic material changes drastically in permeability with temperature and this type should not be used. In past work, Coilcraft 1008HT and

0805CS series SMD inductors have been identified as ideally suited for high temperature stability. A further review of currently available products has confirmed that this series is still the ideal choice.

### **5.7.3 Resistor Selection**

All reference and ballasting resistors in the VNA should be of the high-stability, metal film type. Vishay metal film resistors used in previous work have been shown to have temperature coefficients of less than .05 ppm/°C. Metal film type resistors also offer the best aging tolerance properties of any resistor type [Pease, 1991].

Resistors found in the VSWR bridge should be 0.1% or 0.05% tolerance. For all other resistors in the power supply or digital domain components, 1% tolerance is sufficient.

### **5.7.4 PCB Substrates and Plating**

The frequencies involved in this radar design are low enough that PCBs may be fabricated using standard FR4/G10 construction. For a higher frequency system, high-frequency alumina or Teflon core substrates should be used. Terminations and plating for this environment should be ENIG and not HASL. Any surface contacts in the design should use hard gold plating. For controlled-impedance traces, a four-layer stackup should be used with trace widths calculated per [Gupta, 1996] using the manufacturer's published prepreg laminate thickness dimensions. Groundplanes should be separated and joined at a single point [Brokaw, 1989].

## **5.8 Digital Processing and Control**

The data processing and control of the radar in this thesis is responsible for the sweep frequency selection

and control of the VNA's DDS circuits to generate the RF and recovery LO signals. In the base design of the VNWA — and the sample version available at the university. The VNA uses a PC host for capture and processing of the data and for control of the VNA parameters.

While control of the DDS is implemented over USB through the microcontroller, the sampling digitization of the VNA is completed through the use of a COTS audio CODEC IC meant to implement external sound cards. The original VNWA design made direct use of a PC sound card to digitize the data.

The CODEC IC is a Texas Instrument PCM 2900 stereo interface USB HID class, which simply functions like a USB sound card that is moved directly into the VNWA case. In a new design, it is recommended that the a 16-bit or 18-bit A/D is used and sampled directly to the microcontroller to maintain better control over timing.

### **5.8.1 DSP Capable Microcontroller**

As part of the design of a revised VNA, the selection of a microcontroller for implementation of control and communication is required. The published VNWA design was controlled directly by a PC without microcontroller. Subsequent revisions have added local control of the system with a Atmel ATmega88-20 device. In order to facilitate packing of the VNA as a standalone device, processing will be moved to an on-board controller.

As part of this work, a broad survey of available microcontrollers was completed with the intent being to shift more processing and control capability to the on-board controller to allow a future implementation of a standalone system that could be installed permanently and does not require a PC for data collection. Processing recorded received data may still be completed offline using a PC and a scripting computational engine such as MATLAB or Octave. The primary families of parts evaluated for control

functions were the Microchip dsPIC DSP microcontrollers, the TI Stellaris processor family, the ST Micro STM32F4 ARM processors, and NXP LPC ARM processor family.

Evaluation of the microcontrollers was based on a number of factors including:

- IO Capabilities
- Internal Memory
- DMIPS Speed
- COREMARK Scores
- USB Interface Model
- HW Floating Point Model
- Power Consumption
- Programming Model
- Tool Support & Example Code
- Develop Tool Availability

The recommended choice based on this evaluation is the NXP dual-core LPC4357, which has an ARM CORTEX M4 DSP with hardware floating-point unit and an low-power ARM CORTEX M0+ core which can manage power and IO functions. For a future remote application, the power-hungry M4 DSP core can be put into sleep mode with interrupts and systems timers on the very low-power M0+ core used to wake the DSP core for occasional measurements and data processing.

A future VNA implementation using some FPGA processing is a possibility but would probably be

excessive since most of the processing is sequential. The speed of the frequency sweeps is determined by the settling time of the DDS and the response settling time of the DUT. Recall that the response settling time of the DUT is the maximum time expected for two-way propagation through an ice sheet of the minimum thickness. No appreciable improvement in sweep time would be gained in return for the complexity of FPGA usage. Even for the A/D conversion purposes, FPGA provides no compelling advantages since the IF that is being digitized is very slow for modern A/D technology.

### 5.8.2 Embedded Linux Platforms for Interfaces

As a viable alternative to bare metal microprocessor control with PC interface for data display, there are several very low cost embedded Linux platforms that are now easily obtainable. Choices for embedded Linux are wide ranging but popular devices include the Raspberry Pi Model B which is based on the Broadcom BCM2835 SOC, and the BeagleBone Black, which is based on the Texas Instruments Sitara AM3359AZCZ100 ARM A8 application processor.

The fundamental problem with the operating system implementation is the loss of real-time operating system control of the hardware. Timing tests can be done, as are done with the existing hobbyist VNAs, to determine the latency of the control loops for the DDS chips and for the interface to the audio CODEC. The use of the higher level operating system would simplify programming model complexity at the expense of the timing certainty that would come from a lower-level hardware implementation using a DSP microcontroller.

## 5.9 Power

This section describes the power supply for the radar and looks at the suitability of the power system to achieve the requirements presented in Section 2.7: *System Functional Requirements*. In particular, this

section provides an analysis of the power subsystem on the existing low-cost VNA and the recommended design changes for a new design that is based on it.

### **5.9.1 Power Requirements of VNA**

The initial requirement for the VNA power system was that it should be able to operate from the nominally 5-V power source supplied by a USB connection. Over USB, up to 500 mA is available from any one USB hub. Not all USB ports have 500mA available as the standard specifies that it is per host controller, not per physical port. If other devices are connected to the same host controller, the available current for the VNA would be reduced.

In the interest of planning for future revisions of the design which are able to supply more stimulus power and operate for longer periods of time, additional power features and supply architectures have been considered. In general, the requirement is that the power supply be able to provide very clean, very stable DC power to the oscillator, mixers, DDS, amplifiers and any control circuitry.

### **5.9.2 Power Supply Architecture**

The proposed and analyzed architecture is one that can operate either from the DC supply of a USB connection or from a DC power source jack, convert that voltage to a stable reference using a very high efficiency switching regulator, and then provide local point-of-load regulation at the devices using low power, clean linear Low Dropout (LDO) regulators.

### **5.9.3 Battery Pack for Long Term Monitoring**

One possible enhancement to the VNA design that would allow the flexibility of long term battery power

for a complete system would be to add a high capacity lithium-ion battery pack to power the entire system. A four-cell series string would provide nominally 10.4 V when discharged — assuming lithium iron phosphate chemistry — and 16.8 V at nominally 95% battery state-of-charge. The author has experience in the design of such packs and recommends GAIA/EAS HP601300 cells which provide 20 Ah between typical 90% to 20% SOC discharge limits.

To calculate the number of measurement cycles a large battery would support, first assume an absolute maximum future transmit power level of 1 watt and further assume the use of high-linearity Class A amplifier. Reasonable assumptions for ancillary circuit power consumption bring the total consumption to 4 watts in full transmit mode. Then assume a 10 minute cycle for warm-up, stabilization, and a series of tens to hundreds of averaged sweeps, computation, and storage. At this rate of discharge, in excess of four-hundred measurements could be made on charged set of batteries, well over a year of accumulated data. A small, low data rate satellite packet data transmitter could also be added to send measurement results directly to researchers.

If an advanced chemistry battery pack is included to power a standalone data logging system, a battery management subsystem should be included to provide safe operation. For a four-cell system, high-voltage management IC's such as the TI BQ76PL536 can be used.

#### **5.9.4 Switching Supply Pre-Regulator**

This design proposes the use of a switching pre-regulator which would allow the use of externally supplied DC power or an internal battery pack. A number of circuits were evaluated for the switching pre-regulator with the best performance compromise being the TI — formerly National Semiconductor — LM2676 switching regulator. It features up to 3-A load current at 96% efficiency. The regulator also features On/Off switching so that it can be completely powered down when a measurement cycle is not

taking place. The low power microcontroller core that wakes the remaining circuitry can be powered from a very low current LDO.

### **5.9.5 Point-of-Load Linear Regulators**

Small linear regulators, low dropout (LDO) type are placed at the point of load to ensure precise, clean voltage free of switching noise at the inputs to the DDS chips, the base reference oscillator, the amplifiers, and the A/D converters. Selected for this portion of the design are the Texas Instruments LMC7101 LDOs, which are available in a variety of fixed output voltages.

The A/D converter would use a special precision reference for its  $V_{ref}$  input and since the A/D is a digital device, selecting a precision reference with a voltage that is a multiple of a power of two, in mV, allows more precise fixed-point math on the result in the microcontroller. The precision reference selected is Maxim Integrated MAX6341CPA+.

### **5.9.6 Power Supply Layout Guidelines**

Layout consideration is particularly important for sensitive RF electronic devices. It is advised that there be a separation of the DC groundplane from the RF groundplane — with star grounding — thus isolating the RF return path from large common-mode voltage drops across the DC groundplane from any ohmic losses in the groundplane due to (relatively) high current supply to the reference stage [Brokaw, 1989].

Another layout consideration is that the guidance from National Semiconductor in the LM2676 datasheet regarding layout of the switching power supply inductor and flyback diode loop.

## 5.10 Mechanical and Environmental

This section of the thesis examines miscellaneous aspects of the mechanical and environmental requirements of the radar, how these aspect impact the design and performance of the radar, and how testing would be completed on the system. The requirements found in Section 2.7: *System Functional Requirements* will be verified using the criteria outlined below.

- Examination: Observation of the system to assure that the item is constructed as designed
- Demonstration: Showing that the component works as designed
- Test: Inspection of the item using instruments to verify design
- Analysis: Simulation and calculations will be preform as designed

### 5.10.1 Thermal Environment

The basic requirements for temperature survival were developed as a compromise between the published requirement for equivalent test systems — e.g., US DOD standards — and the experience of the research team from the University, which will eventually be testing this system. The published relevant data is taken from MIL-STD-810G Part 1 Annex C - *Climatic Categories* and gives temperature ranges for Greenland and coastal Antarctic climates. The maximum working temperature for the design is taken to be an Indoor temperature during testing and calibration of +85°C (+185°F) and a minimum operating design temperature for this region to be -46°C (-50°F). The specification states that low temperatures may exceed the low temperature extreme for up to 20% of operating time during the coldest month of the year. This thesis has taken -46°C as the design limit.

The non-operational storage survival temperatures are taken to be the temperatures at which the unit will

survive without damage but its operational ability or accuracy is severely degraded outside of its specified operating point. For the purposes of this radar design, the cold survival temperature minimum is equivalent to the operating temperature minimum of -46°C. The hot survival temperature maximum is taken to be 125°C per standard commercial practice for highly-reliable test equipment.

After much review of published standards and test procedures, it has been determined that the appropriate published test procedure for high temperature testing is outline in MIL-STD-810G Part Two Method 501.5b with limits and rates as given in MIL-STD-810G Part 1 Annex C for Extreme Cold and Extreme Cold Coastal regions. Additional information on design guidelines for evaluation by analysis of temperature performance is per MIL-STD-210B .

Following a similar review, the recommended low temperature testing is given in MIL-STD-810G Part Two Method 502.5 with limits and rates as given in MIL-STD-810G Part 1 Annex C for Extreme Cold and Extreme Cold Coastal regions. Additional information on design guidelines for evaluation by analysis of temperature performance is per MIL-STD-210B .

Optionally, thermal shock testing may also be advantageous. If the radar is moved from a, relatively speaking, warm staging area to the glacier, a steep thermal transition will occur, which may damage components or break solder joints. Thermal shock testing is outlined in MIL-STD-810G Part Two Method 503.5 with limits and rates as given in MIL-STD-810G Part 1 Annex C for Extreme Cold and Extreme Cold Coastal regions. Use of Exposure Condition 2.3.2-C is recommended.

Additional guidance on temperature conditions was obtained from MIL-HDBK-310 - *Global Climatic Data for Developing Military Products.*

## **5.10.2 Moisture, Humidity & Condensation**

The humidity conditions for coastal areas during the local summer can approach saturation of 100% relative humidity per MIL-STD-810G Part 1 Annex C *Climatic Categories*. The specification gives percentage relative humidity ranges between 0% in winter and saturation 100% in summer. Humidity survival should be tested according to MIL-STD-810G Part Two Method 507.5 using specifically Procedure I. Procedure II testing aggravated conditions is unnecessary for this application. Additional guidance on humidity and moisture conditions was obtained from MIL-HDBK-310 - *Global Climatic Data for Developing Military Products*.

## **5.10.3 Requirements and Testing for Corrosion Resistance**

It was assumed for the purposes of this analysis that the test sites are located sufficiently far from shore lines that salt spray and salt fog testing would not be required to ensure survivability of the radar. Should it be determined that this is not the case, testing per MIL-STD-810G Part Two Method 509.5 should be considered.

## **5.10.4 Requirements and Testing for Mechanical Shock and Vibration**

The requirements for mechanical shock, vibration, and acceleration are primarily for survival of transportation and drops during set up of the system. In formal operation, the system will be stationary and not experience any of these forces. Because the system is only expected to experience transit stresses, the appropriate test procedures have been selected as MIL-STD-810G Part Two Method 514.6 test method for vibration profile using 'Figure 514.6C-1 — Category 4 - Common carrier (US highway truck vibration exposure)', MIL-STD-810G Part Two Method 513.6 Acceleration related to survival of drops in

accordance with Procedure I and MIL-STD-810G Part Two Method 516.6 Shock Procedure IV and Procedure VI for transit drop and bench test drops.

## 5.11 Electronics Enclosures

A robust enclosure must be selected for the radar system presented in this thesis due to the harsh environmental conditions at the test site. Because the radar system, as configured currently, generates very little heat from internal power dissipation, a thermal analysis on case was not completed. It is assumed that the electronics can safely be housed in a fully-shielded enclosure that is cooled only by thermal radiation from its sidewalls. If a future implementation of the system with higher transmit powers is considered, a thermal analysis should be undertaken.

It is recommended that the control PCB within the VNA include board-level temperature sensors for calibration purposes. During thermal cycling, a non-release software load could specifically continuously monitor internal temperature to determine the internal operating temperature relative to outside conditions and the warm-up time required to meet steady state conditions. The production release software for field measurements could then use the sensor data to adjust calibration profiles *in situ* based on sensed temperature.

The enclosure should be moisture sealed to prevent corrosion of the electronics or RF shield-can on the PCBs. While no specific IP rating is proposed, the environmental requirements for temperature, moisture and humidity presented in Section 5.10.2: *Moisture, Humidity & Condensation* and Section 5.10.3: *Requirements and Testing for Corrosion Resistance* should be observed.

The enclosure should be metal to provide RF shielding for the circuitry within. Opening and ports within the enclosures should be gasketed with conductive moisture-resistant crush-gaskets to prevent RF leakage into the enclosure.

Since it is assumed that the VNA will be absolutely stationary during measurement activities, no shock-mounting is required for the circuit PCBs inside the VNA. Should the design be used for a mobile platform where vibration would occur during the measurement, the PCBs should be shock-mounted within the enclosure with appropriate vibration-dampening isolation designed for the vibration profile as any mechanical vibration incurred by the reference oscillator — a piezoelectric device — will introduce extra phase-noise/jitter beyond the error terms already calculated in this thesis.

## 5.12 Mounting and Mechanical Structures

While the specific mounting of the antennas for the measurement is left to the researchers implementing the system, recommendations for critical points of importance are presented herein. The specific item to be addressed with regard to mounting the radar system is more specifically the antenna mounts since the mounting will couple into the antenna and affect its impedance match and radiation pattern. Mounting of other system components like the VNA itself, processing or data collection PC, and restraints of RF cables is not critical so long as they remain stable.

As discussed in Section 4.4: *Idealized Analysis of Transmit/Receive Coupling*, the antennas should be mounted with the horizontal elements planar to place the transmitting and receiving antennas in one another's polarization nulls.

The mounting arrangement for the antenna should be rigid such that the antennas cannot move with respect to one another during successive setups during a measurement campaign as described in the system CONOPS. It is critical that the antennas remain in a constant position with respect to one another. This implies that the antenna should be mounted to a single, rigid structure rather than independent masts or tripods that could easily move with respect to one another during successive setups by much more than the target measurement resolution of the radar.

Mounting of the antennas should be done on non-conductive vertical masts. While the plane of principal polarization is horizontal in this application, the boom of the log-periodic type antenna would couple significantly into a closely-spaced vertical mast that served as the mount of the boom. The recommended mounting is on a FRP epoxy-glass pultrusion type square tube extrusion. These extrusions are low loss, low effective dielectric constant, non-conductive, and temperature stable. Cross-members should be added between the vertical masts to maintain relative position and angular alignment of the antennas. The fastening method recommended for multiple setup/tear-down sequences is close-fit mounting holes within the antenna and Screw-Thread-Insert (Helicoil) reinforced holes in the pultrusion.

## 5.13 RF Interconnects

In the design of the radar system, care must be taken in choosing appropriate RF connectors and cables, particularly given the harsh environment in which the system will operate. The requirements that most impacts the connector and cable selection are environmental considerations for temperature, moisture, and humidity.

Some types of RF cable are very poorly suited for low temperate due to embrittlement of the dielectric with temperature or moisture absorption in the outdoor environment. Cable jacketing material with good UV resistance must be chosen since the system will be deployed — initially — in the arctic summer with no shading. While it is important that the cable be low loss and have good phase stability across frequency, most practical amounts of cable attenuation that will be observed at the frequencies of this radar can easily be calibrated out without significant impact on system performance. Expressions for the insertion loss and reflection coefficients of the connectors placed in-line are given below. They can be used in the calibration and correction terms within the processing algorithms.

For the choice of connector, the preference is the standard SMA connectors provided on the existing VNA

system. All SMA type connectors are rated to 18 GHz. The connectors are suitable for up to 500 mating cycles per IEC 60169-15, 1979, and will not suffer degradation as a result of mating cycles during set up and tear down of the radar system during the measurement campaigns that are the CONOPS for this system.

While the IEC standard for the SMA connector does not define maximum VSWR and insertion loss for this connector, the Amphenol base specification for SMA connectors is taken to be the governing one in industry. That standard gives typical values for the maximum refection coefficient generated at a mated connector interface, in VSWR units, is Equation (5.2). The insertion loss per connector, when properly torqued, in is given in Equation (3.80). The quantities given for VSWR are dimensionless and the units of insertion loss,  $IL_{connector}$ , are dB when  $f$  is the frequency point in GHz.

Due to the moisture environment and the repeated cycling of an extended measurement campaign with frequent set up and tear-down cycles, it is recommended stainless steel solid body SMA connectors be used and that the connectors are torqued carefully to the specified 7.5 in-lb with a 5/16 open-end torque wrench. Use of non-torque-limited tools for mating of stainless steel RF connectors in harsh environments is discouraged.

While not waterproof, this type of SMA connector does provide moisture resistance per MIL-STD-202 method 106. Connector parts that meet all the performance specifications and standards for the SMA are available from Amphenol with precision silicone gaskets that further prevent moisture problems in the harsh environment. The silicone gaskets must be replaced regularly on a schedule based on manufacturer's recommendation to maintain performance.

$$VSWR_{Connector} = 1.05 + .005 \cdot f_{GHz} \quad (5.2)$$

$$IL_{\text{connector}} = .03 \cdot \sqrt(f_{\text{GHz}}) \quad (5.3)$$

There are many choices of RF cable that would be perfectly suitable for this application. The recommended cable is a standard RG316 type, which provides a suitable balance of attenuation performance, durability, and flexibility even at the extremely low temperatures likely to be seen in this environment. The insertion loss of the coaxial cables in the system is

$$IL_{\text{RG316}} = L_m [0.45 + 0.0015 (f_{\text{MHz}} - 200)] \quad (5.4)$$

in dB, when  $L_m$  is the length of the cable in meters and  $f_{\text{MHz}}$  is the frequency point, in MHz. This is valid to 1 GHz. The cable attenuation experiences a slight temperature dependence but its effect is an order of magnitude less significant than the frequency dependence for frequencies of interest in this system and it has been omitted from this formula for simplicity. The insertion loss can be calculated for each frequency point in the sweep and applied as a calibration lookup table in measurements. More information about selection of performance coaxial cable for this type of environment, see MIL-STD-188-202.

The CREATIVE antennas that are currently available for use for this project feature an N-Type terminated pigtail of lossy cable. It is highly recommended that this pigtail be removed and quality stainless steel SMA connector be placed onto the antenna directly at the antenna feedpoint where the pigtail is currently mated.

## 5.14 Data Interconnects

Currently, the data connection is provided by a standard USB interface with the VNA having USB Type B female connector. For the immediately envisioned CONOPS in which there are measurement campaigns with repeated set up and an tear down, this connector is sufficient. It is rated to 1500 mating cycles so

degradation of the connector will not be a problem during repeated procedures.

The USB connector, however, is not water resistant and will fail if moisture becomes a problem in the field. Waterproof versions of the USB connector are available from ASSMANN WSW Components, which use standard USB connectors — presumably to maintain spec compliance only in name — which are shrouded in a circular plastic connector with a seal. This type of connector is recommended for extended use to prevent moisture and debris-related shorts at the data connection.

Assuming that the VNA is redesigned per the recommendations of this thesis, the connections to the VNA could be made through USB alone — by the waterproof connectors above — or by more robust connectors suited for the harsh environment. Connections for video or serial interfaces as well as any additional data ports should employ waterproof connectors rated for the temperature range specified. At a minimum, connectors such as the TE Connectivity CPC type multi-pin terminals with seals should be used. Standard sealed Amphenol Mil-Spec connectors would be a very reliable choice for these connections, however, the costs of these connectors would be very high for the low-cost system envisioned. Another preferred, lower cost choice would be the use of Deutsch-IPD DTM series PCB headers and mating sealed connectors. These connectors are very inexpensive, fully-sealed, and provide excellent reliability.

## **CHAPTER 6: CONCLUSIONS**

The fundamental purpose of the research in this thesis was to determine if a very low cost instrument with a VNA architecture is indeed capable of making very high-accuracy measurements of the change in glacial ice sheet thickness between successive measurements using a suitable VNA. It is.

The more specific question that this work attempted to answer was to determine if an existing low-cost hobbyist VNA based on the published design of [Baier, 2007] was able to make these measurement accurately as a pre-assembled item available from any number of hobbyist suppliers item or with only basic modifications to improve the stability of the frequency reference. The conclusion reached in this research is that for very cold ice, and for very shallow depths, the existing hobbyist design will work adequately. All that would remain to be completed is to develop a suitable data processing algorithm that performs the IFFT and a compares raw phase data returns.

For thicker and warmer ice sheets, however, the attenuation of the ice and snow is too great to overcome meager -17 dBm maximum transmit power of the existng design given the dynamic range of the unit is no greater than 90 dB. Returns from a 1-km-thick sheet would require a dynamic range of 120 dB or better. For ice sheets of reasonable thickness or for warm, highly-attenuating surface conditions, the entirety of the returned signal will be well below the noise floor regardless of how much averaging of the returns is completed.

Within this thesis, recommended design changes were presented to the original design published in [Baier, 2007] that would improve the performance (e.g., higher dynamic range A/D, improved double-balanced mixers, amplifiers in the reference oscillator path, etc.) of the design. Analysis strongly suggests that these improvements would allow a redesigned, yet still very low-cost, custom VNA to complete these

measurements.

An additional conclusion of this work is that the short-term frequency stability of the base system reference oscillator is less consequential than the long-term aging stability or the temperature coefficient of the oscillator. Short term oscillator instability, or phase-noise is a Gaussian process. Averaging of multiple samples will reduce the effect of that phase noise to the point where the long-term drift of oscillator due to aging and temperate dominate the effect of the short-term instability.

While the initial design goal was the creation of a VNA for this radar that would be operated interactively by a user in a measurement campaign, the development of the work has lead those involved to conclude that the next logical step — modifying the design to allow remote data collection without user intervention — is incredibly desirable from a programmatic and budget perspective. Because of this, work completed during the latter stages of research has shown that it is entirely feasible to pair the VNA's RF architecture with suitable on-board DSP processing and control system that does not require a power-hungry PC or laptop to collect the data. When the controller and the RF system are paired with power system to allow unmanned, remote collection of thickness data over long period of time, the system developed in this thesis will allow low-cost, long term, high accuracy ice thickness change data collection.

## REFERENCES

- Analog Devices, "Analog Devices Reliability Handbook," Norwood, MA, 2000.
- Analog Devices, "AD9859: 400 MSPS, 10-Bit, 1.8 V CMOS Direct Digital Synthesizer," Norwood, MA, no. AD9859, 2009.
- Analog Devices, (2006). *DC-2.5 GHz High IP3 Active Mixer* [Online]. Available: [http://www.analog.com/static/imported-files/data\\_sheets/AD8343.pdf](http://www.analog.com/static/imported-files/data_sheets/AD8343.pdf)
- Agilent Technologies, "Applying Error Correction to Network Analyzer Measurements," Santa Clara, CA, no. 1287-3, 2002.
- T. C. Baier, "A Low Budget Vector Network Analyzer for AF to UHF," *ARRL QEX*, No. 2, 2007.
- T. C. Baier, "Error Correction in Vector Network Analyzers," Unpublished
- T. C. Baier, "A Small, Simple, USB-Powered Vector Network Analyzer Covering 1 kHz to 1.3 GHz," *ARRL QEX*, no. 1, pp. 32-36, January, 2009.
- C. A. Balanis, "Antenna Theory," 3rd Edition. Hoboken, NJ: John Wiley & Sons, 2005.
- M. Barnes, M. Poirier, and L. Peteres Jr., "Novel GPR Antennas," *Journal of Applied Geophysics*, 1994
- C. R. Bentley, R.H. Thomas, and I. Velicogna, "Global Outlook for Ice and Snow," no. 6A, pp. 100-113, 2007.
- M. Beres and F. P. Haeni, "Application of Ground-Penetrating-Radar Methods in Hydrologic Studies," *Ground Water*, vol. 29, no. 3, pp.375-386, May-June, 1991.
- D. Brandon, "Synchronizing Multiple AD9850/AD9851 DDS-Based Synthesizers," Analog Devices, Norwood, MA, no. AN-587, 2002.
- P. Brokaw, J. Barrow, "Reccomended Grounding for High Frequency Circuits," Analog Devices, Norwood, MA, no. AN-345, 1989.
- G. H. Bryant, "Principles of Microwave Measurements," Revised Edition. London, UK: Institution of Electrical Engineers, 1993.
- K. S. Cole, R. H. Cole, "Dispersion and Absorption in Dielectrics - I - Alternating Current

Characteristics," *Journal of Chemical Physics*, vol. 9, no. 1, pp. 341-352, 1941.

H. F. J. Corr, A. Jenkins, and K. W. Nicholis, "Precise Measurement of Changes in Ice-shelf Thickness by Phase-sensitive Radar to Determine Basal Melt Rates," *Geophysical Research Letters*, vol. 29, no. 8, pp. 73-1–74-4, April, 2002.

D. J. Daniels, "Ground Penetrating Radar," 2nd Edition. IEE Press, 2004.

T. Diep, C. Durvury, "TI Application ESD Guide," Dallas, TX , SSYA010, 2001.

D. J. Drewry, "Comparison of Electromagnetic and Seismic-Gravity Ice Thickness Measurements in East Antarctica," *Journal of Glaciology*, vol. 15, no. 73, pp. 137-150, , 1975.

S. Evans and B. M. E. Smith, "A Radio Echo Equipment for Depth Sounding in Polar Ice Sheets," *Journal of Physics*, vol. 2, no. 2, 1969.

K. Gentile, "Super-Nyquist Operation of the AD9912 Yields a High RF Output Signal," Analog Devices, Norwood, MA , no. AN-939, 2007.

S. P. Gogineni, J. Legarsky, and R. Thomas, "Coherent Radar Depth Sounder Measurements over the Greenland Ice Sheet," *Geoscience and Remote Sensing Symposium Proceedings*, vol. 4, pp. 2258-2260, July 1998.

P. Gudmandsen, "Glacier Sounding in the Polar Regions: A Symposium - Part II Airborne Radio Echo Sounding of the Greenland Ice Sheet," *Geographical Journal*, vol. 135, no. 4, pp. 548-55, 1969.

K. C. Gupta, R. Garg, I. Bahl, P. Bhartia, "Microstrip Lines & Slotline," Secnd Edition. Norwood, MA: Artech House, 1996.

S. Havriliak and S. Negami, "A Complex Plane Representation of Dielectric and Mechanical Relaxation Processes in Some Polymers," *Polymers*, vol. 8, pp. 161-210, 1967.

, "Understanding the Fundamental Principles of Vector Network Analysis," Hewlett Packard, Englewood, CO , no. 1287-1, 1997.

S. Hyvonen, S. Joshi, E. Rosenbaum, "Comprehensive ESD Protection for RF Inputs," *Microelectronics Reliability Journal*, vol. 45, no. 2, pp. 245-254, February, 2005.

International Panel on Climate Change, "Climate Change 2007: Summary for Policymakers," IPCC, February, 2007.

R. W. Jacobal and S. M. Hodge, "RADAR Internal Layers from the Greenland Summit," *Geophysical Research Letters*, vol. 22, no. 5, pp 587-590, 1995.

JEDEC, "Human Body Discharge Model for Electrostatic Discharge Sensitivity Testing," , Arlington, VA, no. JS001-2011, 2011.

A. Jenkins, H. Corr, K. Nicholis, C. Doake, and C. Stewart, "Measuring of the Basal Melt Rate of the Antarctic Ice Shelves using GPS and Phase-Sensitive Radar Observations," *FRISP Report*, no. 14, 2003.

P. Kiciak, (2003, ). *N2PK VNA* [Online]. Available: <http://n2pk.com/VNA/VNAarch.html>

R. W. P. King, G. S. Smith, "Antennas in Matter," 1981.

V. N. Kuleshov, "Oscillators: Stability, Tuning, Noise," *ISSCS 2005 International Symposium on Signals, Circuits and Systems*, vol. 2, pp. 397-402, 2005.

A. Kuchikulla, S. P. Gogineni, P. Kanagaratnam, T. L. Akins, "A Wideband Radar Depth Sounder for Measuring the Thickness of Glacial Ice," *Proceedings of Geoscience and Remote Sensing Symposium, 2004. IGARSS '04*, pp. 105-108, 2004.

Kyocera Group. *KT7050 Series Oscillator Technical Datasheet* [Online]. Available:

J. Legarsky, T. Chuah, and S. P. Gogineni, "Next-Generation Coherent Radar Depth Sounder for Measurement of the Greenland Ice Sheet Thickness," *Geoscience and Remote Sensing, 1997. IGARSS '97. Remote Sensing - A Scientific Vision for Sustainable Development*, pp. 996-998, 1997.

A. Mazzanti, F. Svelto, P. Andreani, "On the Amplitude and Phase Errors of QuadratureLC-Tank CMOS Oscillators," *IEEE Journal of Solid State Circuits*, vol. 41, no. 6, pp. 1305-1313, June, 2006.

J. Mendoza, "Development of an Ice-Penetrating Software-Defined Radar," Thesis, Dept. of Electrical Engineering, Pennsylvania State University, 2012.

J. C. Moore, "Dielectric Variability of Antarctic Ice Core: Implications for RADAR Sounding," *Annals of Glaciology*, vol. 11, pp. 95-103, 1988.

Olhoeft, 1984: G. L. Olhoeft, Applications and Limitations of Ground Penetrating Radar, 1984

G. R. Olhoeft, "Electrical, Magnetic, and Geometric Properties that Determine Ground Penetrating Radar Performance," *Proceedings of the 7th International Conference on Ground Penetrating Radar*, no. 7, pp.477-482, 1998.

B. Panzer, C. Leuschen, A. Patel, T. Markus, s. Goglineni, "Ultra-Wideband Radar Measurements of Snow Thickness Over Ice.," *IGARSS 2010*, pp. 3130-3133, 2010.

R. A. Pease, "Troubleshooting Analog Circuits," Newnes, 1991.

Peters, 1994: L. Peters, J. J. Daniels and J. D. Young, Ground Penetrating Radar as a Subsurface Environmental Sensing Tool, 1994

G. W. Pierce, "Piezoelectric crystal resonators and crystal oscillators applied to the precision calibration of wavemeters," *Proceedings of the American Academy of Arts and Sciences*, vol. 59, no. 4, pp. 81-106, October, 1923.

D. M. Pozar, "Microwave Engineering," 3rd Edition. Hoboken, NJ: John Wiley & Sons, 2005.

V. Ramasami, S. Gogineni, B. Holt, P. Kanagaratnam, K. Gurumoorthy, S. K. Namburi, J. Henslee, D. Braaten, A. Mahoney, and V. Lytle, "A Low Frequency Wideband Depth Sounder For Sea Ice," *IGARSS*, vol. 4, pp. 2811-2813, July, 2003.

D. Rytting, "Network Analyzer Error Models and Calibration Methods," Santa Clara, CA, 2009.

P. Salzenstein, A. Kuna, L. Sojdr and J. Chauvi, "Significant Step in Ultra-High Stability Quartz Crystal Oscillators," *Electronic Letters*, pp. 1433-1434, October, 2010.

A. Shepherd, D Wingham, and E. Rignot, "Warm Ocean Eroding West Antarctic Ice Sheet," *Geophysical Research Letters*, vol. 31, no. 23, 2004.

TAPR. *Tuscon Amateur Packet Radio* [Online]. Available: <https://www.tapr.org>

E. J. Tim, "Network Analyzer with Stable Oscillator for Ice Penetrating Radar," Thesis, Dept. of Electrical Engineering, Pennsylvania State University, University Park, PA, 2012.

G. Turner, A. F. Siggins, "Constant Q Attenuation of Subsurface Radar Pulses," *Journal of Geophysics*, vol. 59, no. 8, pp. 1192-1200, 1994.

The US Geological Survey, (2012). *USGS Listing of Glacier and Glaciology Terminology* [Online]. Available: [http://vulcan.wr.usgs.gov/Glossary/Glaciers/glacier\\_terminology.html](http://vulcan.wr.usgs.gov/Glossary/Glaciers/glacier_terminology.html)

F. Vernotte, G. Zalamansky, "A Bayesian Method for Oscillator Stability Analysis," *IEEE Transactions on Ultrasonics, Ferroelectrics, and Frequency Control*, vol. 46, no. 6, pp. 1545-1550, 1999

J. R. Vig, "Quartz Crystal Resonators and Oscillators for Frequency Control and Timing Applications,"

*IEEE 2004 International Frequency Control Symposium*, January, 2004.

A. H. Waite and S. J. Schmidt, "Gross Errors in Height Indication from Pulsed Radar Altimeters Operating Over Thick Ice or Snow," *Proceedings of the IRE*, vol. 50, no. 6, pp.1515-1520, June, 1962.

J. R. Weber and P. Andreux, "Radar Sounding in the Penny Ice Cap on Baffin Island," *Journal of Glaciology*, vol. 9, no. 55, pp. 49-54, 1970.

W. Wenpeng, Z. Bo, L. Xiaojun, Y. Jian, F. Guangyou, "High-Resolution Penetrating Radar for Ice Thickness Measurement," *Proceedings of the 14th International Conference on Ground Penetrating Radar (GPR)*, pp. 115-118, 2012.

E. J. Wilkinson, "An N-Way Power Divider," *IRE Trans. on Microwave Theory and Techniques*, vol. 8, pp. 116-118, January, 1960.

## **APPENDIX: DEVELOPMENT SOFTWARE INFORMATION**

This appendix presents information about the software and simulation tools used in the process of this design so that those seeking to verify or replicate the work may do so while working with the same set of tools and software builds.

### **Schematic Capture and PCB Layout**

Schematic capture and PCB layout for all components of this design was completed using KiCAD Build 2011.05.25 for 32 bit Debian-based systems on a 64 bit distribution of Ubuntu Linux 12.04 LTS. KiCAD is a completely open source schematic capture and PCB layout suite. While the author had access to other toolchains which offered slightly superior features, a conscious decision was made to use open source toolchains whenever available to allow this research to be duplicated at no cost by other students and researchers. KiCAD is available from <http://www.kicad-pcb.org>.

### **Linear Circuit Analysis**

Linear circuit analysis for this work was completed using a combination of proprietary tools and free tools. As schematic files are available, simulations can be reconstructed in any open tool. Linear simulation was completed primarily using GENESYS 2012 with harmonic balance simulations completed in Agilent ADS 2009. Nonlinear simulations and power simulations were completed using LTspice, available freely from <http://www.linear.com>.

### **Antenna Modeling and Propagation**

All propagation, antenna modeling, and electromagnetic simulation was completed using the FEKO 6 modeling suite. FEKO is a proprietary tool with feature-limited free version available to academia.

### **Microcontroller Programming**

Initial microcontroller work was completed using the open unlimited LPCexpresso tools from CodeRed

technologies and NXP. The toolchain is based on the ECLIPSE IDE and the GNU toolchain.